Order Number 9218247

Design and implementation of instrumentation for the observation of infrared (vibrational) circular dichroism from aqueous solutions

Lee, Ou, Ph.D.

City University of New York, 1992

U·M·I

300 N. Zeeb Rd.
Ann Arbor, MI 48106

DESIGN AND IMPLEMENTATION OF INSTRUMENTATION FOR THE OBSERVATION OF INFRARED (VIBRATIONAL) CIRCULAR DICHROISM FROM AQUEOUS SOLUTIONS

by

OU LEE

A dissertation submitted to the Graduate Faculty in Chemistry in partial fulfillment of the requirement for the degree of Doctor of Philosophy, The City University of New York.

1992

This manuscript has been read and accepted for the Graduate Faculty in Chemistry in satisfaction of the dissertation requirement for the degree of Doctor of Philosophy.

Jan 15 1992
Date

Chair of Examining Committee

1/15/92
Date

Executive Officer

Supervisory Committee

The City University of New York

Abstract

DESIGN AND IMPLEMENTATION
OF INSTRUMENTATION FOR THE OBSERVATION OF
INFRARED (VIBRATIONAL) CIRCULAR DICHROISM
FROM AQUEOUS SOLUTIONS
by
OU LEE

Adviser: Professor Max Diem

This dissertation reports the design and construction of two state-of-the-art dispersive instruments for the observation of Infrared (Vibrational) Circular Dichroism, their optimization, as well as their superior performance. A discussion and comparison of result between the dispersive unit and Fourier transform infrared VCD describe the advantages and disadvantages of the respective technical approaches. The studies of alanyl peptides in aqueous solution demonstrate application aspects of VCD in attacking the difficult yet important problems of

molecular conformation in aqueous solution, particularly for biological molecules. Furthermore, the exhibited structural sensitivity of VCD toward molecular chirality can find wide utilization in chiral analysis and determination, in such field as chiral synthesis and separation.

To Nancy (Siu Gun)
Her encouragement and patience made the
completion of this work possible

And To My Mother and Brothers
for their encouraging words and well wishes

And To My late Father
His dream has been fulfilled

Acknowledgements

I wish to express my sincerest gratitude to Dr. Max Diem, my mentor, for his guidance throughout the progress of this study, for his invaluable time, and for his patience in the preparation of this manuscript. He has opened my eyes to the fascinating world of molecular optical activity and vibrational spectroscopy. Under his leadership, I have grown not only as a scientist but also as a human being. His professional conduct, liberal within reason and discipline, will definitely be remembered.

I would like thank Dr. William Grossman for his skillful teaching in instrumentation, analytical spectroscopy, and numerous enlightening conversations to train me become a thoughtful Analytical Chemist. The individual attention he has given me and his devotion to his students will always be appreciated.

I also wish to thank my former and present colleagues: Dr. Uma Gunnia, Dr. Gull-maj Roberts, Dr. Indira Persaud, Arthur Barlow, Miriam Gulotta, and Dr. Sheryl Birke for their friendship. I can never

forget the many friendly, yet some times intense, scientific discussions. The results of those discussions are reflected in this dissertation. Moreover, the memorable atmosphere of cultural exchange I have experienced will certainly be missed.

I am also in debt to my many relatives, especially my grandmother, aunts and uncles. Without their generous financial support, my "American Dream" would still be only a dream. Particularly, my heartfelt appreciation goes to Aunt Chan Lee Hsieh and Uncle John C. Hsieh, who were instrumental for bringing me here, and have been supportive both in my personal life and in my professional career ever since I landed in this country in Summer, 1983.

Finally, I am very grateful for the financial support given me by Hunter College, Chemistry Department in form of Teaching Assistantships, and by the National Institute of Health in form of Research Assistantship.

Preface

The fascinating phenomenon of optical activity has interested many scientists ever since its discovery. Around 1810, French physicist Jean Baptiste Biot discovered that when polarized light passes through certain substances the polarization direction of the light is rotated about its propagation direction[i]. The observed effect is called optical rotation, and the substances which exhibit it are called optically active. Optical rotation is one measure of optical activity. Biot's study also showed that optical activity is due to some molecular characteristic of the substance, known later as the chirality of the molecule.

Circular dichroism (CD), which measures the absorption difference between left and right circularly polarized light, was discovered in 1895 by yet another French physicist, Aime Cotton. Circular dichroism was soon understood to come about from the same mechanism as optical rotation.

Although optical rotation and circular dichroism provide similar information about the molecule, CD relates the information closely to the molecular structure of some particular light-absorbing groups. Thus, its results are much easier interpreted. However, CD was not widely used because of the extreme instrumental difficulties. Only since the first commercial CD instrument in the ultraviolet-visible region was available in 1960, CD has become a popular tool in research and analysis.

The extension of the measurements of circular dichroism into the infrared region has been a long-sought goal for many scientists. It would utilize the combination of the sensitivity of CD and the specificity of infrared spectroscopy to solve a variety of problems in molecular stereochemistry. Yet, technical obstacles made the goal impractical until the early Nineteen Seventies[ii]. The infrared circular dichrograph became reality, thanks to technical advances on several fronts, such as highly sensitive IR detectors, personal computers, and, especially, the photoelastic modulators in the IR region.

Because of the chiral nature of circularly polarized light, CD is sensitive to the following:

a. structural difference between the molecules

containing chiral center(s), *i.e.*, L- and D- (or S- and R-) enantiomers;

b. conformational difference, *e.g.*, secondary structures of polypeptides, *i.e.*, α-helix or β-sheet, and that of DNA, *i.e.*, right- or left-handed double stranded helix.

In the latter cases, the molecule may or may not contain a chiral center, however, the overall conformation must exhibit a pattern of asymmetry (symmetry point group, C_1) or dissymmetry (C_n).

The field of studying optical activity has been getting some new attention in light of recently emphasized efforts on chiral molecules in areas such as Organic Chemistry (chiral synthesis), Analytical Chemistry (chiral separation and detection), and biochemistry (effect of molecular conformation on biological reaction), and, particularly, in pharmaceutical industry (new drug design and pharmacology of enantiomers)[iii,iv].

The aim of the research project in this dissertation has evolved, under the general objectives of the laboratory research group, from the design and instrumentation of VCD instruments to study stereochemical systems, specifically, conformation of biologically significant molecules. The detection and

analysis in biomolecular spectroscopy has been challenging due to some inherent difficulties, such as small quantity (thus, low concentration) available.

The major task of the research project includes two assignments: first, design and building of two state-of-the-art VCD instruments; second, employing the instruments to study a specific system and to demon-strate the usefulness of the technique. This project also lays the ground work for others to carry out conformation studies via VCD on peptides and nucleic acids in aqueous solution.

The scope of this thesis incorporates five chapters. Chapter One briefly reviews theoretical foundations of circular dichroism, including polarized light, circularly polarized light, the measurement of CD. Also contained in the chapter are Lambert-Beer's law for absorption spectroscopy and a short description of a theoretical model, the Coupled Oscillator, for the interpretation of VCD data. In Chapter Two, the focus is on the different methods to observe VCD and their respective advantages and disadvantages. The three known designs are dispersive IR with a photo-elastic modulator (PEM), regular FT-IR with a PEM, and a modified FT-IR (using a polarizing Michelson interferometer). Chapter Three deals

exclusively with the designs of the two dispersive VCD units, optimized for separate regions, at Hunter College. The extensive discussion covers optical design, electronic layout as well as their optimization. Presented in Chapter Four are VCD data to show the instrumental performance of VCD-I and VCD-II. A comparison with FT-IR-VCD is also made, based on spectra of the same sample. Chapter Five emphasizes the application aspect of VCD via thorough studies of alanyl dipeptide and alanyl tripeptide. The VCD data exhibit an exceptional sensitivity of the technique toward stereochemistry, both in terms of structure and conformation.

References

[i] Applequest, J., *American Scientist*, **1987**, 75, 58.

[ii] Stinson, S.C., *Chemical & Engineering News*, **Nov. 11, 1985**, 21.

[iii] *Chemical & Engineering News*, **March 19, 1990**, 40.

[iv] Brittain, H.G., *Spectroscopy*, **1991**, 6(3),, 10; and 6(6), 13.

Table of Contents

Abbreviations

AC - alternating current.

ADC - analog-to-digital converter.

CD - (electronic) circular dichroism (in ultraviolet-visible region).

COM - coupled oscillator model.

CPL - circularly polarized light.

DC - direct current.

D-D - D-alanyl-D-alanine.

D-D-D - D-alanyl-D-alanyl-D-alanine.

D-L - D-alanyl-L-alanine.

FT - Fourier transform.

FT-IR - Fourier transform infrared spectroscopy (or spectrophotometer).

FT-VCD-PEM - a VCD instrument built on a FT-IR with a PEM.

FT-VCD-PMI - a VCD instrument built on a FT-IR with a PMI.

IR - infrared spectroscopy.

LD - linear dichroism.

L-D - L-alanyl-D-alanine.

L-L - L-alanyl-L-alanine.

L-L-L - L-alanyl-L-alanyl-L-alanine.

MCT - mercury cadmium telluride, HgCdTe

PC - personal computer.

PEM - photoelastic modulator.

PMI - polarizing Michelson interferometer.

VCD - vibrational (infrared) circular dichroism (or dichrograph).

VCD-I - The first dispersive VCD built at Hunter College.

VCD-II - The second dispersive VCD built at Hunter College.

ZPD - zero path difference (between the fixed mirror and the movable mirror in the Michelson interferometer).

Symbols

$A(t,\bar{R})$ - vector potential of light.

$A(\bar{\nu})$ - sample absorbance.

$A_+(\bar{\nu})$ - sample absorbance due to right CPL.

$A_-(\bar{\nu})$ - sample absorbance due to left CPL.

C - concentration, in mole/L.

D - dipole strength or dipole moment.

$\bar{E}$ - electric vector potential of light.

e_j - electric charge on particle j.

G_f - band shape function of the fth band.

g - anisotropy, or dissymmetric factor.

H - magnetic vector potential of light.

$I(\bar{\nu})$ - light intensity.

$J_n(x)$ - n th order Bessel function.

$\bar{K}$ - light wave vector, $\bar{K} = (2\pi\nu/c)\bar{r}_K$.

l - sample cell pathlength.

$\bar{m}$ - magnetic dipole operator.

m_j - mass of particle j.

$N(\bar{\nu})$ - complex refractive index.

p_j - momentum of particle j.

Q - nuclear coordinates.

q - electron coordinates.

R - rotational strength.

r_j - position of particle j.

$V(\bar{\nu})$ - detector signal output.

$V_{DC}(\bar{\nu})$ - transmission signal not modulated by PEM.

$V_{AC}(\bar{\nu})$ - signal modulated by PEM.

$\epsilon(\bar{\nu})$ - molar extinction coefficient, $L \cdot mole^{-1} \cdot cm^{-1}$.

$\bar{r}_U$ - unit vector in direction U.

λ - light wavelength.

ν - light frequency, c/λ in Hz.

$\bar{\nu}$ - light frequency, $1/\lambda$ in cm^{-1}.

ω - angular frequency of light.

$\bar{\mu}$ - electric dipole operator.

θ - initial phase of light.

Ψ - molecular wavefunction.

Constants and Units

c - speed of light in vacuum, 2.998×10^{10} cm/second.

cm^{-1} - wavenumber.

esu - electric static unit, 1.602×10^{-19} coulomb.

$\hbar$ - Planck constant over 2π.

L - liter.

N - Avogadro's constant, 6.0225×10^{23} mol^{-1}.

List of Tables

List of Figures

Chapter One

Theoretical Background of Circular Dichroism

This chapter consists of brief discussions on the following topics: i) linearly polarized light, circularly polarized light, and Lambert-Beer's Law; ii) a short formalism of circular dichroism (CD) and its measurements, dipole strength and rotational strength; and iii) vibrational circular dichroism (VCD) and the coupled oscillator model.

1.1 Light

The complex phenomena presented in this dissertation all begin with light interacting with molecules of matter. It is appropriate first to express light in a basic mathematical fashion[1,2], so all the later discussions will be built on a solid foundation.

1.1.1 Linearly Polarized Light

In a right-handed coordinate system the electric potential ($E(t,Z)$), a vector, of a linearly polarized electromagnetic wave propagating in Z direction (*cf.* Figure 1) in vacuum, is given by

$$\begin{aligned} \bar{E}(t,Z) &= \bar{E}_o \sin [2\pi(\nu t - Z/\lambda) + \theta] \\ &= \bar{E}_o \sin [\delta + \theta] \qquad (1.1) \\ \delta &= 2\pi(\nu t - Z/\lambda) \qquad (1.2) \end{aligned}$$

Here, $\bar{E}_o$ is the maximum amplitude, a constant vector in the XY plane, perpendicular to the Z axis (the spatial coordinate); the direction of $\bar{E}_o$ will be referred to as the polarization direction; ν is the frequency of the light wave (in Hz); t is the time the light has traveled; λ is the wavelength ($\lambda = c/\nu$), c is the speed of light in vacuum; and θ is the initial phase.

The light can be characterized by a wave vector $\bar{K} = (2\pi/\lambda)\bar{\epsilon}_z$, where $\bar{\epsilon}_z$ is a unit vector in propagation direction, Z. Notice that $\nu = c\bar{\nu} = c/\lambda = c|\bar{K}|/2\pi = \varpi/2\pi$. Here, ϖ is the angular frequency, $2\pi\nu$, and $\bar{\nu}$ is $1/\lambda$, in unit of wavenumber (cm^{-1}).

In addition to the electric component, light also has a magnetic component

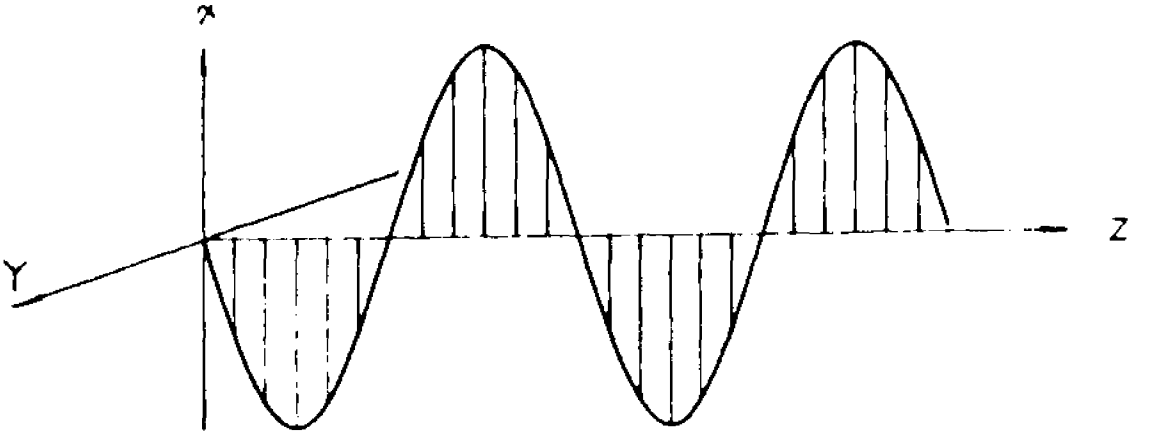

Figure 1. Linearly Polarized Light ($\vec{E}_x$).

$$\bar{H}(t,Z) = \bar{H}_o \sin [\ \delta + 0\ ] \qquad (1.3)$$

Here $\bar{H}_o$ is the maximum amplitude, a constant vector, also in the XY plane but perpendicular to $\bar{E}_o$.

For a point in space $\bar{R} = (X,Y,Z)$ and time t, both $\bar{E}(t,\bar{R})$ and $\bar{H}(t,\bar{R})$ can be derived from a single quantity called vector potential $\bar{A}(t,\bar{R})$.

$$\bar{E}(t,\bar{R}) = -\frac{1}{c}\frac{\delta \bar{A}(\bar{t},\bar{R})}{\delta t} \qquad (1.4)$$

$$\bar{H}(t,\bar{R}) = \bar{\nabla} \times \bar{A}(t,\bar{R}) \qquad (1.5)$$

For light with wave vector $\bar{K}$ along the Z axis and linearly polarized alone $\bar{U}$, a chosen spatial direction, one gets

$$\begin{aligned} A(\bar{t},\bar{R}) &= \bar{\epsilon}_u A_o \cos(2\pi\nu t - \bar{K}\cdot\bar{R}) \\ &= \bar{\epsilon}_u A_o \cos\delta \end{aligned} \qquad (1.6)$$

The amplitude $\bar{A}_o$ is proportional to both $\bar{E}_o$ and $\bar{H}_o$. (They are equal in Gaussian units.) The direction of $\bar{U}$ can be any direction perpendicular to $\bar{K}$ and, thus, the Z axis. For instance, if $\bar{U}$ = X and substituting $\bar{\epsilon}_u = \bar{\epsilon}_x$ into Equation (1.6), one obtains,

$$\bar{A}(t,\bar{R}) = \bar{\epsilon}_x A_o \cos\delta \qquad (1.7)$$

This is a light wave linearly polarized in the XZ plane. If $\bar{U} = Y$, one would obtain a light wave polarized in the YZ plane. The third example is $\bar{U} = (X+Y)/\sqrt{2}$, in which case, $\bar{\epsilon}_u = (\bar{\epsilon}_x+\bar{\epsilon}_y)/\sqrt{2}$. Substituting into Equation (1.6), one obtains

$$\bar{A}(t,\bar{R}) = \frac{1}{\sqrt{2}} (\bar{\epsilon}_x+\bar{\epsilon}_y)A_o\cos\delta \qquad (1.8)$$

This is a linearly polarized light whose projection on the XY plane is 45° with respect to the X axis. It is also interesting to note that this particular linearly polarized light can be rewritten as

$$\begin{aligned}\bar{A}(t,\bar{R}) &= \frac{1}{\sqrt{2}} (\bar{\epsilon}_x\bar{A}_o\cos\delta + \bar{\epsilon}_y\bar{A}_o\cos\delta) \\ &= \bar{A}_x + \bar{A}_y \qquad (1.9)\end{aligned}$$

Equation (1.9) implies that this particular linearly polarized light can be decomposed into two linearly polarized waves perpendicular to each other in the XZ and the YZ planes, respectively. These two waves are in phase and have identical amplitudes, $\sqrt{2}$ times smaller than the original one. (*cf.* Figure 2)

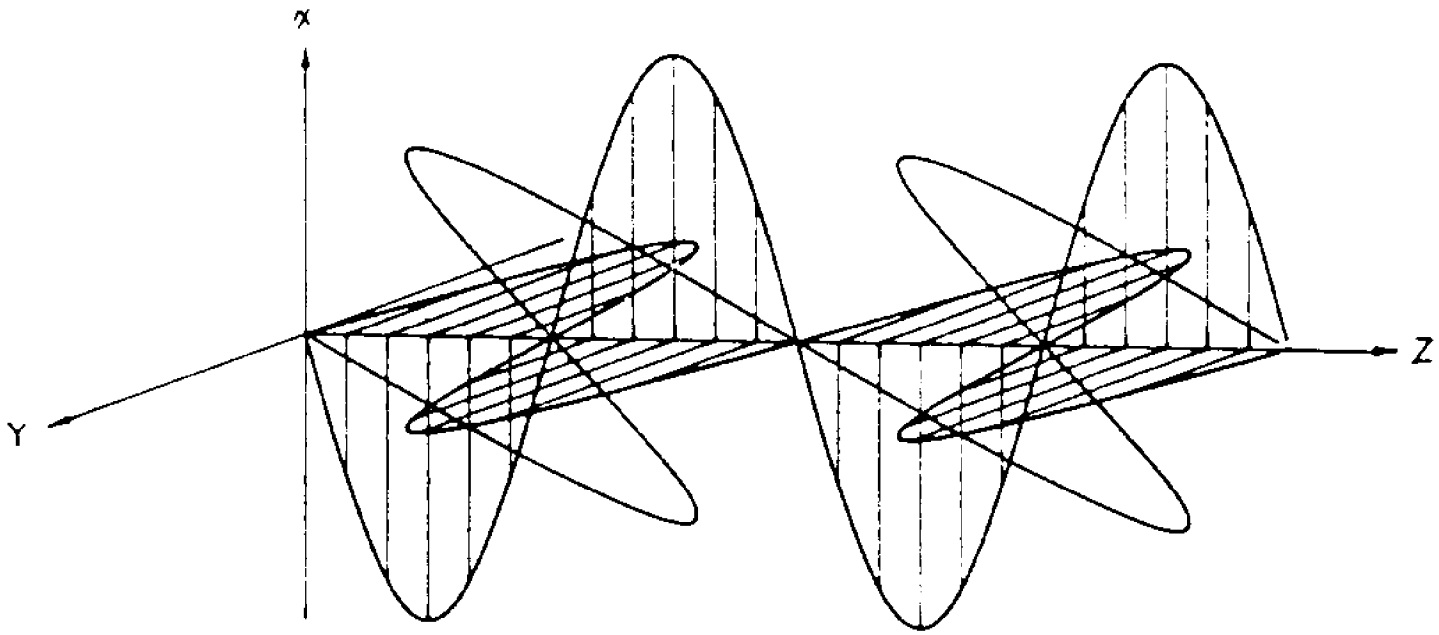

Figure 2. Decomposition of a Linearly Polarized Wave ($\bar{E}$) into Two Linearly Polarized Waves (E_x and E_y)

1.1.2 Circularly Polarized Light (CPL)

As described above, a linearly polarized wave can be considered as the superposition of two linearly polarized waves which are in phase. To simplify the problem, the discussion hereafter concentrates just on the electric component of a light wave, $\bar{E}$. If there is a phase difference induced between the $\bar{E}_x$ and $\bar{E}_y$ components of the aforementioned linearly polarized light (Equation (1.9)), the resulting superposition will depend on the induced phase difference. Unless the phase difference is 0 or $\pi/2$, the superposition will no longer be a linearly polarized wave.

If the waves $\bar{E}_x$ and $\bar{E}_y$ in Equation (1.8) have a phase difference of $\pi/2$ ($i.e.\ \theta_y-\theta_x = \pi/2$), the superposition of those two linearly polarized waves will lead to a circularly polarized wave.

$$\begin{aligned}\bar{E}(t,z) &= \bar{E}_{ox}\cos(\delta) + \bar{E}_{oy}\cos(\delta+\pi/2) \\ &= \bar{E}_{ox}\cos(\delta) - \bar{E}_{oy}\sin(\delta) \end{aligned} \qquad (1.10)$$

The circularly polarized wave has a constant amplitude, $|\bar{E}| = |\bar{E}_{ox}| = |\bar{E}_{oy}|$. However, the direction of its electric potential (polarization direction) keeps changing, rotating around the light propagation

direction (Z axis) at a pace of one rotation per wavelength the light travels (*cf.* Figure 3b). The induced phase shift (called retardation), $\Delta\theta = \theta_y - \theta_x$ must be equal to $+\pi/2$ (or $2n\pi + \pi/2$, n = 0,1,2,...) for left CPL; $-\pi/2$ (or $2n\pi - \pi/2$, n = 0,1,2,...) for right CPL.

The constant amplitude and ever changing direction of polarization are the characteristic of circularly polarized light. A graphic illustration (*cf.* Figure 3) will clarify the definition of circularly polarized light. The light propagates towards the viewer as the vector of its electric potential rotates in a circle with a constant amplitude. The CPL whose electric vector rotates clockwise is called right circularly polarized light and the one whose electric vector rotates counterclockwise is called left circularly polarized light.

CPL can be characterized by the unit vector $\bar{\epsilon}_u$, which is a complex number. Thus, $\bar{\epsilon}_x$ and $\bar{\epsilon}_y$ are the unit polarization vector of light propagating along the Z axis and linearly polarized along X and Y, respectively. Then, $\bar{\epsilon}_u = (\bar{\epsilon}_x + i\bar{\epsilon}_y)/\sqrt{2} = \bar{\epsilon}_+ = \bar{\epsilon}_R$ will stand for the polarization vector of right CPL, and $\bar{\epsilon}_u = (\bar{\epsilon}_x - i\bar{\epsilon}_y)/\sqrt{2} = \bar{\epsilon}_- = \bar{\epsilon}_L$ will stand for the polarization vector of left CPL propagating in positive Z direction. Here and elsewhere, i is the imaginary unit

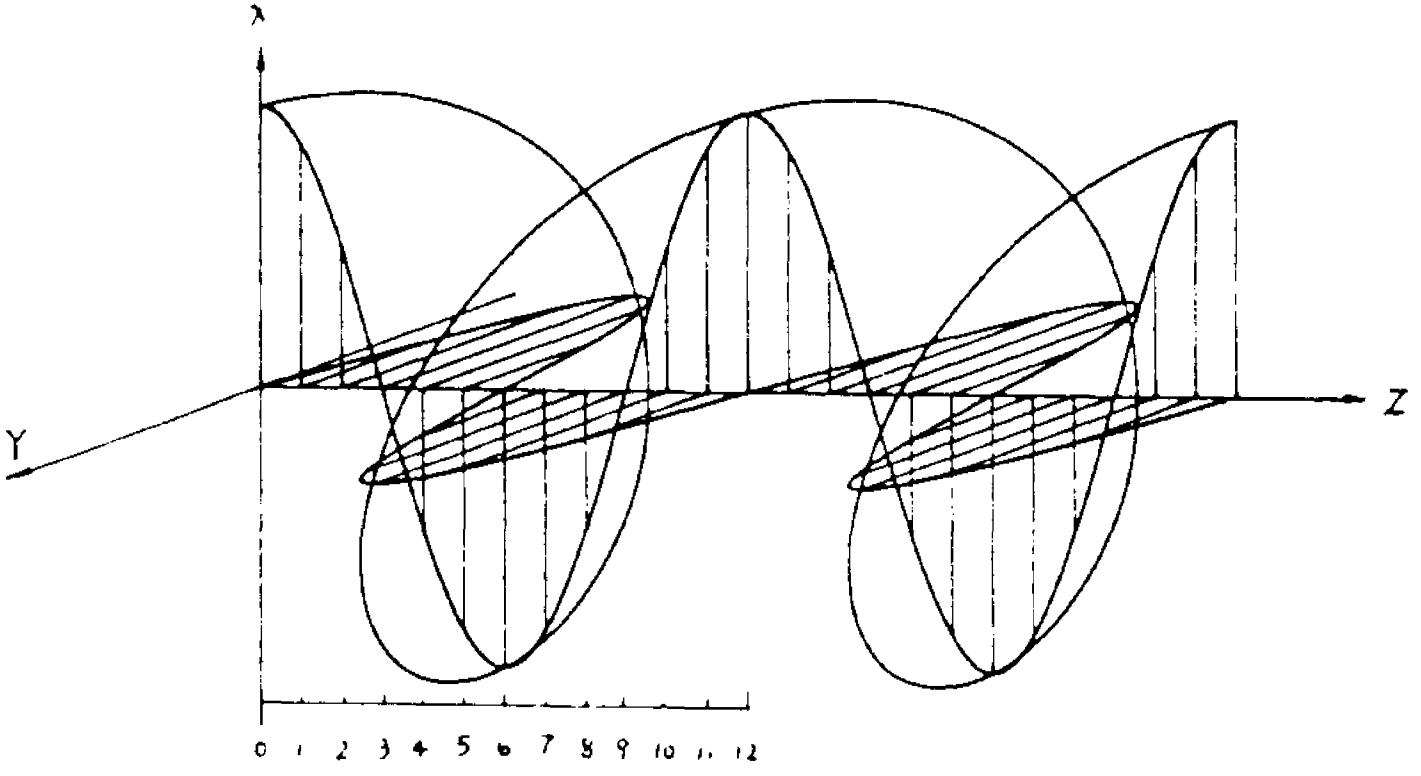

Figure 3. Right Circularly Polarized Light: a) side view;

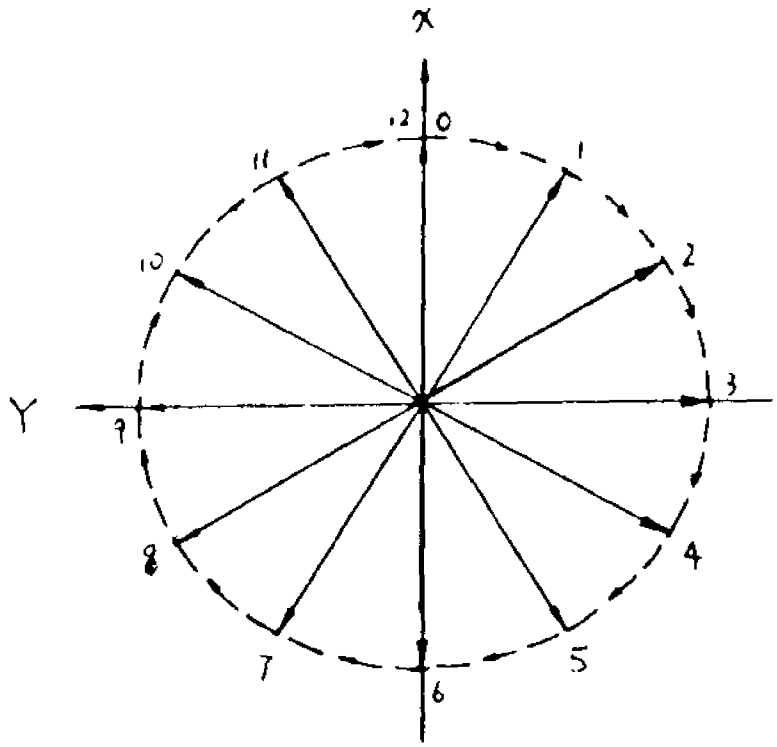

b) viewing against light propagation

($i=\sqrt{-1}$).

When the retardation is $2n\pi$, n = 0,1,2,..., the superposition is the same as the original linearly polarized light. When $\Delta\theta$ is $(2n+1)\pi$, n=0,1,2,..., the superposition is still linearly polarized light but with opposite polarization direction. All other superpositions of the two waves, $\bar{E}_x$ and $\bar{E}_y$, between linearly polarized light and circularly polarized light are called elliptically polarized light.

It is also worth noting that linearly polarized light can be decomposed into two circularly polarized light waves, one left CPL and one right CPL. They are in phase and have equal amplitudes, half of the amplitude of the original linearly polarized light. For example,

$$\begin{aligned} \bar{E}_x &= 0.5\,[(\,\bar{E}_x\,) + (\,\bar{E}_x\,)] \\ &= 0.5\,[(\,\bar{E}_x - i\bar{E}_y\,) + (\,\bar{E}_x + i\bar{E}_y\,)\,] \\ &= 0.5\,(\,\bar{E}_R + \bar{E}_L\,) \end{aligned} \qquad (1.11)$$

1.1.3 Lambert-Beer's Law

When a collimated monochromatic light beam with intensity I_o and wavenumber $\bar{\nu}$ passes through a

homogeneous, isotropic absorbing sample, it is attenuated. If the sample concentration is C [mole/L], and the cell pathlength is l cm, the transmitted light intensity is given by the Lambert-Beer's law:

$$I(\bar{\nu}) = I_0(\bar{\nu})10^{-\epsilon(\bar{\nu})Cl} = I_0(\bar{\nu})e^{-\alpha(\bar{\nu})l} \qquad (1.12)$$

where $\epsilon(\bar{\nu})$ is the molar extinction coefficient or absorptivity in $Lmol^{-1}cm^{-1}$, $\alpha(\bar{\nu})$ is absorption coefficient, in cm^{-1}, and $\alpha(\bar{\nu}) = 2.303\ \epsilon(\bar{\nu})C$.

In the field of molecular optical activity, the complex refractive index, $N(\bar{\nu})$ is used.

$$N(\bar{\nu}) = n(\bar{\nu}) - (i/4\pi\bar{\nu})\kappa(\bar{\nu}) \qquad (1.13)$$

In an oriented sample, $N(\bar{\nu})$ depends on the directions of propagation and polarization of the light. Even in an isotropic sample, $N(\bar{\nu})$ is still a function of the light polarization if the sample is optically active.

If $N_x(\bar{\nu})$ and $N_y(\bar{\nu})$ denote the complex refractive indices for light polarized linearly along X or Y direction, respectively, and $N_L(\bar{\nu})$ and $N_R(\bar{\nu})$ the refractive indices for left CPL or right CPL, respectively, then the difference $N_x(\bar{\nu}) - N_y(\bar{\nu})$ is a meas-

ure of linear birefringence (the real part) and linear dichroism (the imaginary part); the difference $N_L(\bar{\nu})$ - $N_R(\bar{\nu})$ is a measure of circular birefringence (the real part) and circular dichroism (the imaginary part).

Lambert-Beer's law holds for circularly polarized light as well, though is does not hold in general for samples in which $N(\bar{\nu})$ depends on the polarization state of light. Therefore, the following equation stands

$$I(\bar{\nu}) = I_o(\bar{\nu})e^{N(\bar{\nu})l} \qquad (1.14)$$

1.2 Circular Dichroism (CD)

Passing through a chiral medium, right and left circularly polarized light beam experience different electric and magnetic environments. The interactions between light and molecules are different for these two forms of CPL. As a result, the net absorption effect by the chiral medium on the right CPL should be different from that of the left CPL. Therefore, the measurement of the difference between

those two absorptions reveals some insight into the molecular chirality. Another way to understand why circular dichroism is so sensitive towards the molecular chirality is that the circularly polarized light itself is chiral. The tip of the electric vector travels in space in a helical route, which has a handness.

Conventional CD measures the electronic transitions of molecules in the ultra-violet and visible (UV-Vis) region of electromagnetic radiation in the wavelength 180 - 700 nm range. Typical chromophores are $\pi^* \leftarrow n$ or $\pi^* \leftarrow \pi$ transitions of organic or biological molecules. For example, a carbonyl group, C=O, absorbs at 295 nm due to a $\pi^* \leftarrow n$ transition; an unconjugated C=C functional group absorbs at 180 nm in the ultraviolet due to a $\pi^* \leftarrow \pi$ transition, while the absorption peak of conjugated C=C shifts towards visible as the chain grows longer[3]. Some transitions which also fall into this region are the *d* to *d* electronic transitions of the transition metals as well as the charge transfer between a metal center ion and ligands in a system where different ligands form a chiral environment surround the center metal ion.

1.2.1 Dipole Strength and Rotational Strength

Two important quantities in the CD measurement are the dipole strength and the rotational strength of a transition.

From quantum chemistry, one can derive the following relationships:

$$\text{Dipole Strength } (D) = |\langle\Psi_o| \bar{\mu} |\Psi_1\rangle|^2 \qquad (1.15a)$$

$$= \frac{2.303 \times 3 hc}{8\pi^3 N} \int_{\text{band}} \frac{\epsilon(\bar{\nu})}{\bar{\nu}} d\bar{\nu} \qquad (1.15b)$$

where $\bar{\mu}$ is the electric dipole operator; Ψ_o is an electronic ground state; and Ψ_1 is the first excited state. $\epsilon(\bar{\nu})$ is the molar absorptivity.

The first part of the equation, (1.15a), can be derived from quantum chemistry, the second part, (1.15b), from statistical thermodynamics. The integration represents the area under an absorption peak corresponding to one electronic transition. That is, of course, an experimental measurement. The terms in front of the integral is a constant, 9.188 X 10^{-39} esu cm erg in SI units.

The rotational strength, R, is a unique quantity CD measures, that accounts for the interaction between the electronic transition and the magnetic

transition.

$$R = \mathrm{Im}[\langle\Psi_o|\ \vec{\mu}\ |\Psi_1\rangle\cdot\langle\Psi_1|\ \vec{m}\ |\Psi_o\rangle] \qquad (1.16a)$$

$$= \frac{2.303 \times 3\ hc}{32\pi^3 N} \int_{band} \frac{\epsilon_L(\bar{\nu}) - \epsilon_R(\bar{\nu})}{\bar{\nu}}\, d\bar{\nu}$$

$$= 2.297 \times 10^{-39} \int_{band} \frac{\epsilon_L(\bar{\nu}) - \epsilon_R(\bar{\nu})}{\bar{\nu}}\, d\bar{\nu} \qquad (1.16b)$$

Its unit is also in esu cm erg in SI unit. Here: $\vec{m}$ is the magnetic dipole operator; $\epsilon_L(\bar{\nu})$ is the molar absorptivity due to the left CPL, and $\epsilon_R(\bar{\nu})$ is the molar absorptivity due to the right CPL.

Circular Dichroism measures the absorption difference between left CPL and right CPL. A unique characteristic of an individual band for CD measurement is a dissymmetric factor, or anisotropy (g), defined by[4]:

$$g = \frac{\Delta\epsilon(\bar{\nu})}{\epsilon(\bar{\nu})} = \frac{\epsilon_L(\bar{\nu}) - \epsilon_R(\bar{\nu})}{0.5[\epsilon_L(\bar{\nu}) + \epsilon_R(\bar{\nu})]} = \frac{4\ R}{D} \qquad (1.17)$$

Practically, $\Delta\epsilon(\bar{\nu})$ is computed from the maximum of a CD peak, and $\epsilon_R(\bar{\nu})$ is computed from the maximum of

the corresponding absorption peak. To be more accurate, $\Delta\varepsilon(\tilde{\nu})$ and $\varepsilon(\tilde{\nu})$ should be the areas under the respective bands. The latter part of the equation is easily obtained, from Equations (1.14b) and (1.15b). The anisotropy, g, is a characteristic constant which is used to identify a compound and its optical purity.

1.2.2 Quantum Chemical Description

In their book "Spectroscopy with Polarized Light", Michl and Thulstrup[1] discuss thoroughly the formulation of circular dichroism. Therefore, I shall present only a summary of this description.

In quantum chemistry, any measurable property of a molecule can be expressed as

$$B_{o\rightarrow f} = |\langle\Psi_o(q,Q)|\ \mathbf{H}\ |\Psi_f(q,Q)\rangle|^2 \qquad (1.18)$$

Here, $\Psi_o(q,Q)$ is the wavefunction of the initial state of a transition (for example, ground state); q is the electron coordinate; Q is the nuclei coordinate; $\Psi_f(q,Q)$ is the wavefunction of the final state of the transition; and H is the operator of the desired property.

For the total absorption,

$$A_{o->f} = \frac{1}{2\pi\hbar^2\nu^2} |\langle\Psi_f(q,Q)| \sum_j \frac{e_j}{m_j} e^{i\bar{K}\cdot\bar{r}_j} \bar{r}_U\cdot\bar{p}_j|\Psi_o(q,Q)\rangle|^2 \quad (1.19)$$

where e_j is the electric charge on the jth particle; m_j is the mass of the particle; $\bar{r}_j$ is its position; $\bar{K}$ is the light wave vector, $\bar{K}=(2\pi\nu/c)\bar{r}_K$; $\bar{r}_K$ is the unit vector in the propagation direction of light; $\bar{r}_U$ is the unit vector in the polarization direction of light, and $\bar{p}_j$ is the linear momentum of the jth particle.

The operator $e^{i\bar{K}\cdot\bar{r}_j}$ can be expanded into a converging Taylor series since $\bar{K}\cdot\bar{r}_j$ is << 1.

$$e^{i\bar{K}\cdot\bar{r}_j} = 1 + i\bar{K}\cdot\bar{r}_j - 0.5\ (\bar{K}\cdot\bar{r}_j)^2 + \ldots \quad (1.20)$$

Keeping only the first term will change the integral in Equation (1.19) to the familiar electric transition dipole moment, M.

$$M(of) = \langle \Psi_f |\ \bar{\mu}\ |\ \Psi_o \rangle \quad (1.21)$$

$$\bar{\mu} = \sum_j e_j\bar{r}_j \quad (1.22)$$

The second term in the expansion is purely imaginary.

It leads to the following integral:

$$\langle \Psi_f(q,Q) | \sum_j \frac{e_j}{m_j} (e^{i\vec{K}\cdot\vec{r}_j})(\vec{\epsilon}_U \cdot \vec{p}_j) | \Psi_o(q,Q) \rangle \qquad (1.23)$$

Recalling that $\vec{K} = (2\pi\nu/c)\vec{\epsilon}_K$, the integral becomes

$$2\pi i\nu \langle \Psi_f(q,Q) | \sum_j \frac{e_j}{m_j} (\vec{r}_j)_K (\vec{p}_j)_U^* | \Psi_o(q,Q) \rangle \qquad (1.24)$$

Its integration will lead to the magnetic dipole transition moment, $\boldsymbol{M}$, and the electric quadrupole transition moment, Q.

$$\boldsymbol{M}(of) = \langle \Psi_f | \mathfrak{m} | \Psi_o \rangle \qquad (1.25)$$

$$\mathfrak{m} = 0.5 \sum_j (\vec{r}_j \times \vec{p}_j)_{K \times U}^* \qquad (1.26)$$

$$Q(of) = \langle \Psi_f | \mathfrak{q} | \Psi_o \rangle \qquad (1.27)$$

$$\mathfrak{q} = 0.5 \sum_j [(\vec{r}_j \vec{p}_j)_{KU}^* + (\vec{r}_j \vec{p}_j)_U^* {}_K] \qquad (1.28)$$

Ignoring the terms of higher order in the expansions in Equation (1.20), the total absorp-

tion, Equation (1.19), can now be rewritten as the sum of those three transition moments.

$$A_{o->f} = \frac{4\pi^2\bar{\nu}}{hc} n \sum_f G_f(\bar{\nu}) \left| \vec{\epsilon}_U^* \cdot M(of) + (\vec{r}_K \times \vec{\epsilon}_U^*) \cdot \boldsymbol{M}(of) + i\pi\bar{\nu}\vec{r}_K Q(of)\vec{\epsilon}_U^* \right|^2 \qquad (1.29)$$

Here, $G_f(\bar{\nu})$ is a band shape function; n is the number of molecules per cm^3, n = CN/1000; N is Avogadro's number.

In case of an unpolarized light passing through isotropic solutions, the total absorption will contain only the first term, the electric dipole transition moment. That is the already-familiar dipole strength, Equation (1.15a).

$$D = |M(of)|^2$$
$$= \mathrm{Re} < \Psi_o | \bar{\mu} | \Psi_f > \cdot < \Psi_f | \bar{\mu} | \Psi_o > \qquad (1.30)$$

In case of circularly polarized light, all three terms in the sum contain real and imaginary parts. When the square is evaluated (dot product of two integrals), there will be some cross terms between M(of) and $\boldsymbol{M}$(of). It is these cross terms that give rise to the molecular optical activity.

1.3 Vibrational Circular Dichroism (VCD)

1.3.1 Formalism

VCD is the extension of the CD technique into the infrared region. The theoretical formalism of VCD is the same as the electronic CD only this time both nuclear and electronic contributions need to be evaluated[5,6,7]. Again, the measurements are the dipole strength and the rotational strength. In VCD, like in other vibrational spectroscopies, there are 3N-6 molecular vibrational transitions (N is the number of atoms in the molecule under investigation). Each transition has a dipole strength (D_i) and a rotational strength (R_i). One should notice that under normal condition both excited and ground vibrational states are in the same electronic state (usually the ground state). Therefore, in the formalism Equations (1.15) and (1.16), one only needs to substitute the vibrational wavefunctions for the electronic wavefunctions, and applies them to all the vibrational transitions.

$$D_i = |\langle \Psi_o | \vec{\mu}_i | \Psi_1 \rangle|^2 \qquad (1.31a)$$

$$= 9.188 \times 10^{-39} \int_{\text{band}} \frac{\epsilon_1(\bar{\nu})}{\bar{\nu}} d\bar{\nu} \qquad (1.31b)$$

$$R_i = \mathrm{Im}\left[\langle\Psi_o|\ \bar{\mu}_i\ |\Psi_1\rangle\cdot\langle\Psi_1|\ \bar{m}_i\ |\Psi_o\rangle\right] \qquad (1.32a)$$

$$= 2.297 \times 10^{-39} \int_{\text{band}} \frac{\epsilon_{iL}(\bar{\nu}) - \epsilon_{iR}(\bar{\nu})}{\bar{\nu}}\, d\bar{\nu} \qquad (1.32b)$$

$$g_i = \frac{\Delta\epsilon_i(\bar{\nu})}{\epsilon_i(\bar{\nu})} = \frac{\epsilon_{iL}(\bar{\nu}) - \epsilon_{iR}(\bar{\nu})}{0.5[\epsilon_{iL}(\bar{\nu}) + \epsilon_{iR}(\bar{\nu})]} = \frac{4R}{D} \qquad (1.33)$$

$$i = 1,2,\ldots 3N-6,$$

One unique advantage VCD offers over CD is the specificity since the absorption peaks in the infrared region are often correlated with certain molecular vibrations of some known individual functional groups. The assignments of many infrared peaks are unambiguous, and can be easily found in the literature. In addition, via normal coordinate analysis, the infrared frequencies and peak intensities provide information regarding the spatial orientation of the functional groups, and thus, the molecular conformation. VCD will further explore that information in the realm of chirality.

The first experimental infrared CD was observed in 1973 by Holtzwarth's group[8]. They were the only

group capable of performing this experiment at that time. The extreme technical difficulty involved in building a VCD instrument was the foremost obstacle for other researchers interested in entering the field. The rapid advancement in VCD instrumentation in the late 70s and early 80s[9,10,11,12] has been attributed to the commercial availability of some key IR optical components with highly desired property, such as a high sensitivity HgCdTe detectors in the mid-IR region. Also, the commercial availability of high quality photoelastic modulators (PEM), the heart of a VCD instrument, ended an era of home-made PEMs. Another special factor contributed to the acceleration in VCD instrumentation was the dramatic decrease in the price of the powerful personal computer in the early 80s. The later versions of VCD instruments rely on PCs for instrument control, data processing and on-screen spectral display. The use of PCs not only sped up VCD experiments because of the rapid data processing, but also improved reproducibility by a complete digital control of the instruments.

Along with the progress on the experimental front, theoretical work has also flourished[5-7]. There are many theoretical models established to attempt to calculate the frequency and intensity of

VCD peaks[13-20]. However, the lack of knowledge of the exact molecular wavefunctions has been the stumbling block in the searching for a universal theoretical model. Work in this area has met limited success. It is worth noting that any calculation of a VCD spectrum automatically would also predict the corresponding infrared spectrum, both intensity and frequency, in the region of interest.

On the other hand, theoretical models that apply only to a few specific situations have been much more successful. One of those models is the coupled oscillator model (COM)[19]. Diem's group has been using this model exclusively and very successfully in interpreting data on some small peptide samples in the amide I region as well as on some DNA model molecules in the C=O stretching vibration region[21-25]. For this reason, we will only discuss the coupled oscillator theory, as an example, to interpret VCD data and to demonstrate the usefulness of vibrational circular dichroism in the study of molecular conformation.

1.3.2 Coupled Oscillator Model (COM)

The formalism of the coupled oscillator model was published in detail in references 19, 23 and 26. Therefore, I only wish to concentrate on its results and applications, instead of repeating the deviation of the equations.

The coupled oscillator model considers the interaction between two identical or near identical dipoles. When under the radiation of an appropriate wavelength, instead of each dipole vibrating independently, the two dipoles oscillate in a coordinated manner, as if they "saw" each other. The interaction produces a distinct couplet in the VCD spectrum (positive-negative or negative-positive). The magnitudes and wavenumbers of the couplet depend on the geometry of the dipoles. The coupling is not, however, limited to two dipoles, and can be extended to any number of dipoles (called n-mer) until infinity (polymer). The geometry dependence of VCD is used, in turn, to study molecule conformation.

For simplicity, consider a hypothetical, optically active dimer composed of two diatomic, polar molecules, 1 and 2 (that is, two dipoles). The distance vector, $\overline{T}_{12}$, links the centers of mass of the dipoles.(*cf.* Figure 4)

For each molecule, the ground state and excited

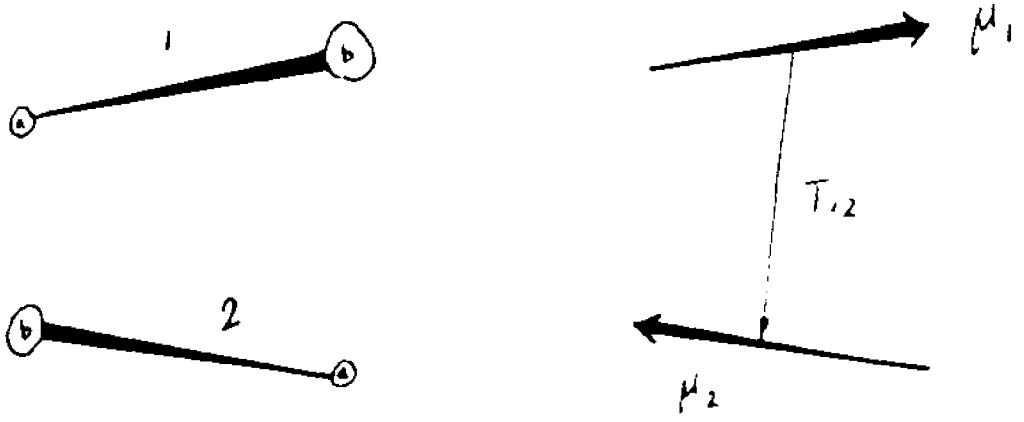

Figure 4. Coupled Oscillator Model (cf. text); μ_1=μ_2: dipole moments; T_{12}: distance vector linking centers of mass.

state are:

$$\Psi^1_o(q_1,Q_1) \text{ and } \Psi^1_f(q_1,Q_1) \text{ for } 1$$
$$\Psi^2_o(q_2,Q_2) \text{ and } \Psi^2_f(q_2,Q_2) \text{ for } 2$$

where q and Q are electronic and nuclear coordinates, respectively. The total wavefunction for the ground state of the dimer is, then:

$$\Omega_o(q_1,Q_1,q_2,Q_2) = \Psi^1_o(q_1,Q_1)\ \Psi^2_o(q_2,Q_2) \qquad (1.34)$$

Because the two molecules are identical, the first excited states, $\Psi^1_o\Psi^2_f$ and $\Psi^1_f\Psi^2_o$, would be degenerate. Therefore, the actual excited state, Ω, of the dimer will be the symmetrical (+) and antisymmetrical (-) linear combinations of these two degenerate states.

$$\Omega_+ = (\Psi^1_o \Psi^2_f \pm \Psi^1_f \Psi^2_o) / \sqrt{2} \qquad (1.35)$$

Next, one needs to evaluate μ_+ and m_+ for transition Ω_o -> Ω_+ and μ_- and m_- for transition Ω_o -> Ω_-, and derive the corresponding dipole strength, D_i, and rotational strength, R_i, respectively.

The result of the derivation yields the following equations (for more details, see references 10,

23 and 26). For the dimer, or two coupling dipoles,

$$D_{1,2} \; (= D_{\pm}) = \mu^2 \pm \bar{\mu}_1 \cdot \bar{\mu}_2 \qquad (1.36)$$

$$R_{1,2} \; (= R_{\pm}) = \mp \, (\pi \bar{\nu}_o / 2c) \; (\bar{T}_{1,2} \cdot \bar{\mu}_1 \times \bar{\mu}_2) \qquad (1.37)$$

$$\bar{\nu}_{1,2} \; (= \bar{\nu}_{\pm}) = \bar{\nu}_o \pm V_{12} \qquad (1.38)$$

$$V_{12} = \frac{\bar{\mu}_1 \cdot \bar{\mu}_2}{|\bar{T}_{12}|^3} - \frac{3 (\bar{\mu}_1 \cdot \bar{T}_{12}) (\bar{\mu}_2 \cdot \bar{T}_{12})}{|\bar{T}_{12}|^5} \qquad (1.39)$$

Here $D = \mu^2$ is the dipole strength of the diatomic monomer, and $\bar{\nu}_o$ is the monomer absorption frequency in cm^{-1} and c the velocity. They both can be obtained from a monomer absorption spectrum, or from the literature. D_1 and D_2 are the respective dipole strengths of the two absorption bands in the coupled system. R_1 and R_2 are the rotational strengths of the corresponding CD bands. They have equal absolute values but opposite signs. $\bar{\nu}_1$ and $\bar{\nu}_2$ are the energies (frequencies) of the two transitions, respectively. V_{12} is one half of the frequency splitting between those two transitions. Notice that

$$D_+ + D_- = 2D = 2\mu^2 \qquad (1.40)$$

$$R_+ + R_- = 0 \qquad (1.41)$$

$$\bar{\nu}_+ + \bar{\nu}_- = 2\bar{\nu}_o \qquad (1.42)$$

For a system of n coupled dipoles, the kth resultant exciton transition is given by:

$$R_k = -(\pi\nu_o/c) \sum_{i=1}^{n} \sum_{j>i}^{n} C_{ik}C_{jk}(\bar{T}_{ij}\cdot\bar{\mu}_i x\bar{\mu}_j) \qquad (1.43)$$

$$D_k = \sum_{i=1}^{n} C_{ik}^2\mu_i^2 + 2\sum_{i=1}^{n} \sum_{j>i}^{n} C_{ik}C_{jk}(\bar{\mu}_i\cdot\bar{\mu}_j) \qquad (1.44)$$

$$\bar{\nu}_k = \bar{\nu}_o + e_k \qquad (1.45)$$

Here $\bar{\mu}_i$ is the ith (monomer) dipole moment; $\bar{T}_{ij}$ is the distance vector between the centers of mass of dipoles i and j; C_{ij} are eigenvectors of perturbation matrix V_{ij}; and e_k are eigenvalues of V_{ij}:

$$V_{ij} = \frac{\bar{\mu}_i\cdot\bar{\mu}_j}{|\bar{T}_{ij}|^3} - \frac{3(\bar{\mu}_i\cdot\bar{T}_{ij})(\bar{\mu}_j\cdot\bar{T}_{ij})}{|\bar{T}_{ij}|^5} \qquad (1.46)$$

To calculate the VCD intensity and frequency on a molecule with two or more interacting dipoles, one

must provide the coordinates of the interacting groups. The dihedral angles between the groups, however, will depend on the molecule conformation, which is actually the goal of the investigation. Usually, a trial conformation is used, for example, an open-chain configuration, or better still, the conformation from a solid state structure. The monomer dipole strength (D) and absorption frequency ($\tilde{\nu}_o$) are needed as well.

To predict the conformation of a molecule in solution, one needs to compare the experimentally observed IR and VCD spectra to the calculated ones, and to find a reasonable fit with the observed one. There will be an infrared and a VCD spectrum corresponding to each assumed conformation, which is formed by rotating certain bonds (*i.e.*, changing torsion angles) in small steps, one at a time, from the initial conformation. The torsion angles from the best-fit calculation would be used to construct the corresponding molecular conformation. This trial-and-error method can be easily done on a personal computer in real time.

The Coupled Oscillator Model demonstrates clearly that the VCD signal will contain information about the spatial arrangement of the polar groups in

a molecule. This, of course, makes VCD a very attractive tool for the study of molecular conformation in solution. Typical examples include peptides, whose conformation is determined by the conformational angles, ϕ and ψ, along the peptide backbone. The amide I vibration around 1680 cm^{-1} is mostly due to the stretching motion of the carbonyl (C=O) group, located in the peptide linkage plane. In VCD calculation, sets of IR and VCD spectra, i.e., D, R and $\bar{\nu}$, can be calculated by varying the angles (from 180° to -180 degree)[21,27].

Since the coupled oscillator model is a relatively simple approach to a very complex problem, it has some weaknesses. The calculation is carried out for an idealized system, in which only the interaction between identical monomers exists. No solvent effects are considered, and only one vibrational mode is considered. Therefore, the model does not apply to the whole spectrum. Finally, it needs the information on absorption (dipole strength) and frequency of the monomer transition.

In spite of these limitations, the model has been very useful in numerous situations[19,21,28,29], and has also been extended to some cases involving near-identical oscillators[22,25]. Furthermore, it has been applied to molecules containing more than

two oscillators[22,23,26,30]. The simplicity of the model has made the applications on macromolecules system possible, and the results have been very promising.

Chapter Two

Methods to Observe Vibrational Circular Dichroism

In this chapter, the three different approaches presently used to measure VCD will be investigated. The three essential optical designs are: a dispersive infrared spectrophotometer with a photoelastic modulator (PEM), a Fourier transform infrared (FT-IR) with a PEM, and a modified FT-IR with a polarizing Michelson interferometer (PMI).

2.1 Dispersive Vibrational Circular Dichrograph

2.1.1 General Remarks

The dispersive design was the choice of the very first infrared circular dichroism instrument built by Holtzwarth *et al.*[8,9,31]. It was also chosen by several other researchers in the field when they built their respective first VCD instruments[10, 11,12,32]. This design is appealing since it follows the design of the commercial (electronic) circular di-

chroism (CD) instruments and the resulting equipment is reliable, flexible and easy to operate.

Optically, a dispersive VCD is obtained by adding two extra components, a polarizer and a photoelastic modulator (PEM), to the sample compartment of a conventional dispersive infrared spectrophotometer (*cf.* Figure 5a). VCD is observed via a high frequency polarization modulation. Radiation emerging from the exit slit of the monochromator is linearly polarized after passing a polarizer, and then converted to circular polarization by a PEM. Grosjean and Legrand originally proposed this method[33,34].

For differential measurement of two large quantities, it is well known that it is more accurate to measure the very small difference (10^{-3} - 10^{-6} of the average of the two originals) by a high frequency alternate-current (AC) modulation method, rather than a direct subtraction method. It is called the "AC advantage", resulting in a sensitivity increase by two to three orders of magnitude[34,35]. The subtraction method is to directly measure the two large quantities and subsequently subtract them. The AC method consists of measuring a quantity (*e.g.*, absorption) in two different but closed related modes (*e.g.*, polarizations of light) by alternating between

these two modes at a high frequency. Later, a lock-in amplifier tuned to the high frequency is used to extract the difference.

For a VCD instrument, the key component is the Photoelastic Modulator (PEM), which produces left circularly polarized light (CPL) and right CPL. The working principle of a PEM can be found elsewhere[36, 37,38] and will only be described briefly here. When periodically compressed and expanded by one or two piezoelectric transducers, some isotropic crystals (in the infrared, for example, ZnSe or CaF_2) display an optical characteristic called birefringence. The phenomenon of birefringence is that the crystals exhibit sightly different refractive indices towards light waves of different polarizations. The waves are otherwise identical in frequency, amplitude and phase. To graphically describe birefringence, let us put a polarized light wave in a right-handed coordinate system within one of the crystal mentioned above. The polarized light wave penetrates the crystal along the Z direction, perpendicular to the direction of compressing and expanding (X axis). The direction of Y axis is perpendicular to both Z and X axes, thus, is also determined. The birefringence occurs when the crystal is compressed (or expanded). Penetrating that crystal, a light wave polarized in

XZ plane experiences a refractive index that is sightly different from the one experienced by a another light wave polarized in YZ plane. Once again, the two waves are otherwise identical in frequency, amplitude and phase. To achieve circular polarization, the PEM introduces a phase shift of $\pm\pi/2$ (a quarter of the wavelength, $\lambda/4$) between these two linearly polarized components. Thus, as the two waves exit the crystal, the superposition of these two waves is no longer a linearly polarized light, but circularly polarized light.

The technique of vibrational circular dichroism commonly applies a double modulation method. The light beam is modulated by a chopper, as in a conventional infrared spectrophotometer, and by a PEM. Since a dispersive VCD is normally intended to only cover a specific frequency region, the design can be optimized for that region by carefully selecting optical components from the IR source to the grating in the monochromator to the detector. An example of such selection is found in Chapter Three where detailed descriptions of the two VCD instruments built at Hunter College are presented.

2.1.2 Theory of Operation - Optics

In order to understand the working principle of a dispersive VCD instrument, it is beneficial to first look at the evolution of light along the optical path, from the source to the detector (*cf.* Figure 5a) in mathematical terms[39].

Figure 5b indicates the axes of the polarizer (X′) and the photoelastic modulator (X is the compressing and expanding axis), such that the spatial relationship of the axes is clear. $\hat{\imath}$, $\hat{\jmath}$, $\hat{\imath}'$ and $\hat{\jmath}'$ are the unit vectors of the axes X, Y, X′ and Y′, respectively.

In the following, the electric potential of the light ($\bar{E}(t,Z)$), abbreviated **E** hereafter, will be derived at certain key components. After passing the monochromator, the light has a wavelength of λ (and a frequency of ν).

i. After passing the polarizer:

$$\begin{aligned} \mathbf{E} &= \sqrt{2}\,\hat{\imath}'\ E_o\cos(2\pi\nu t - Z/\lambda) \\ &= \sqrt{2}\,\hat{\imath}'\ E_o\cos\delta \end{aligned} \qquad (2.1)$$

where E_o is the maximum amplitude, a constant; t is the time; Z is the distance the light has traveled (*cf.* Equation 1.1); and $\delta = (2\pi\nu t - Z/\lambda)$. The square root

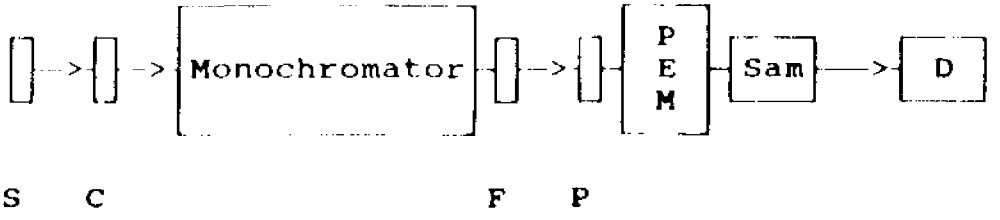

S: infrared source
C: optical chopper
F: filter
P: polarizer
PEM: photoelastic modulator
Sam: sample
D: infrared detector

Figure 5a. Optical Scheme of a Dispersive VCD

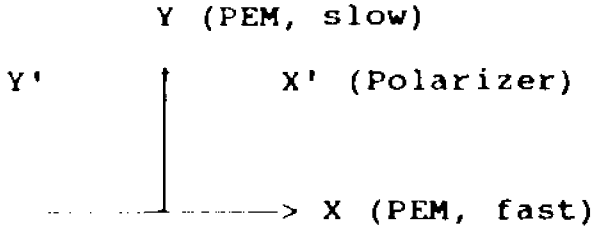

Figure 5b. Optical Axes of Components

of two normalizes the intensity to unity.

ii. At the PEM:

The polarizer axis is set at 45° with respect to the optical axis of the PEM (X axis). As the light reaches the PEM, it is considered a superposition of two linearly polarized waves. One is parallel and the other is perpendicular to the PEM axis(*cf.* Chapter One). The Electric vector of the light can be rewritten as

$$\mathbf{E} = \hat{\imath}\, E_o \cos\delta + \hat{\jmath}\, E_o \cos\delta \qquad (2.2)$$

Passing the PEM, one of the two components, for example, the Y component, is retarded by an angle of α (called a phase shift).

$$\mathbf{E} = \hat{\imath}\, E_o \cos\delta + \hat{\jmath}\, E_o \cos(\delta + \alpha) \qquad (2.3)$$

Here, we have chosen the X axis (unit vector $\hat{\imath}$) as the fast axis, and the Y axis (unit vector $\hat{\jmath}$) as the slow axis.

Actually, both waves are slowed down while penetrating the PEM crystal, but by different amounts due to the birefringence of the crystal. The two waves experience different refractive indices as they

traverse the crystal; and α is their phase difference as they exit the crystal.

Equation (2.3) can be rewritten as

$$\begin{aligned}
\mathbf{E} &= \mathbf{1}\, E_o\cos(\delta+0.5\alpha-0.5\alpha) + \mathbf{j}\, E_o\cos(\delta+0.5\alpha+0.5\alpha) \\
&= \mathbf{1}E_o[\cos(\delta+0.5\alpha)\cos(0.5\alpha) + \sin(\delta+0.5\alpha)\sin(0.5\alpha)] \\
&\quad + \mathbf{j}E_o[\cos(\delta+0.5\alpha)\cos(0.5\alpha) - \sin(\delta+0.5\alpha)\sin(0.5\alpha)] \\
&= E_o\cos(\delta+0.5\alpha)\cos(0.5\alpha)(\mathbf{1}+\mathbf{j}) \\
&\quad + E_o\sin(\delta+0.5\alpha)\sin(0.5\alpha)(\mathbf{1}-\mathbf{j}) \\
&= 1.414\mathbf{1}'E_o\cos(0.5\alpha)\cos(\delta+0.5\alpha) \\
&\quad - 1.414\mathbf{j}'E_o\sin(0.5\alpha)\sin(\delta+0.5\alpha)
\end{aligned} \tag{2.4}$$

Since $\mathbf{1} + \mathbf{j} = \sqrt{2}\,\mathbf{1}'$, and $\mathbf{1} - \mathbf{j} = -\sqrt{2}\,\mathbf{j}'$. (*cf.* Figure 5b).

Equation (2.4) is viewed as two linearly polarized waves, perpendicular to each other. They are $\pi/2$ out of phase, comparing $\cos(\delta+0.5\alpha)$ and $\sin(\delta+0.5\alpha)$, and with different amplitudes. Later, in the discussion of the VCD calibration, this information will be utilized. Deriving Equation (2.4) further:

$$\begin{aligned}
\mathbf{E} = 0.707E_o[&\mathbf{1}'\cos(0.5\alpha)\cos(\delta+0.5\alpha)+\mathbf{1}'\sin(0.5\alpha)\cos(\delta+0.5\alpha) \\
&- \mathbf{j}'\cos(0.5\alpha)\cos(\delta+0.5\alpha) - \mathbf{j}'\sin(0.5\alpha)\sin(\delta+0.5\alpha) \\
&+ \mathbf{1}'\cos(0.5\alpha)\cos(\delta+0.5\alpha) - \mathbf{1}'\sin(0.5\alpha)\cos(\delta+0.5\alpha)
\end{aligned}$$

$$+ \vec{j}'\cos(0.5\alpha)\sin(\delta+0.5\alpha) - \vec{j}'\sin(0.5\alpha)\sin(\delta+0.5\alpha) \ ]$$

$$= 0.707\ E_o\ x$$

$$[\cos(0.5\alpha)+\sin(0.5\alpha)][\vec{i}'\cos(\delta+0.5\alpha)-\vec{j}'\sin(\delta+0.5\alpha)]$$

$$+ 0.707E_o\ x$$

$$[\cos(0.5\alpha)-\sin(0.5\alpha)][\vec{i}'\cos(\delta+0.5\alpha)+\vec{j}'\sin(\delta+0.5\alpha)]$$

(2.5)

Equation (2.5) is the sum of a right circularly polarized light (CPL) wave and a left CPL wave. They are in phase but have different amplitudes, which depend on α. As α varies periodically, right CPL or left CPL alternatively dominates the intensity of light produced, and we infer that the PEM produces alternating right and left circularly polarized light waves.

iii. At the sample:

After passing an absorbing chiral sample, the light electric potential becomes (applying the Lambert-Beer's Law)

$$\mathbf{E} = 0.707E_o\ x\ \{\ [\cos(0.5\alpha)+\sin(0.5\alpha)]\ x$$

$$[\vec{i}'\cos(\delta+0.5\alpha)-\vec{j}'\sin(\delta+0.5\alpha)]10^{-0.5A_+(\nu)}$$

$$+ [\cos(0.5\alpha)-\sin(0.5\alpha)]\ x$$

$$[\hat{1}'\cos(\delta+0.5\alpha)+\hat{j}'\sin(\delta+0.5\alpha)]10^{-0.5A_-(\bar{\nu})}\} \quad (2.6)$$

Here $A_+(\bar{\nu})$ is the absorbance of the sample due to right circularly polarized light, and $A_-(\bar{\nu})$ is the absorbance due to left CPL. Because the absorption is a measure based on the intensity of light, and the intensity is directly proportional to the square of the electric potential ($\mathbf{E}$) of the light, the factor 0.5 in front of $A_-(\bar{\nu})$ and $A_+(\bar{\nu})$ thus accounts for the square.

$$\begin{aligned}\mathbf{E}^2 = {} & 0.5E_o^2 \times \\ & \{[\cos(0.5\alpha)+\sin(0.5\alpha)]^2[\hat{1}\cos(\delta+0.5\alpha)-\hat{j}\sin(\delta+0.5\alpha)]^2 10^{-A_+(\bar{\nu})} \\ & +[\cos(0.5\alpha)-\sin(0.5\alpha)]^2[\hat{1}\cos(\delta+0.5\alpha)+\hat{j}\sin(\delta+0.5\alpha)]^2 10^{-A_-(\bar{\nu})} \\ & + 2[\cos^2(0.5\alpha)-\sin^2(0.5\alpha)][\hat{1}\cdot\hat{1}\cos^2(\delta+0.5\alpha)-\hat{j}\cdot\hat{j}\sin^2(\delta+0.5\alpha) \\ & + (\hat{1}\cdot\hat{j}-\hat{1}\cdot\hat{j})\cos(\delta+0.5\alpha)\sin(\delta+0.5\alpha)]10^{-[A_+(\bar{\nu})+A_-(\bar{\nu})]}\}\end{aligned} \quad (2.7)$$

Applying the following vector and trigonometry identities:

$$\hat{1}\cdot\hat{j} = \delta_{ij} \begin{cases} = 1, & \text{if } i = j \\ = 0, & \text{if } i \neq j \end{cases} \quad (2.8)$$

$$\sin^2 x + \cos^2 x = 1, \quad (2.9)$$

and $$\sin(2x) = 2\sin(x)\cos(x) \qquad (2.10)$$

Equation (2.7) becomes

$$E^2 = 0.5E_o^2\{[1+\sin\alpha]10^{-A_+(\bar{\nu})} + [1-\sin\alpha]10^{-A_-(\bar{\nu})} + 2[\cos^2(0.5\alpha)-\sin^2(0.5\alpha)]\ x\ [\cos^2(\delta+0.5\alpha)-\sin^2(\delta+0.5\alpha)]10^{-[A_+(\bar{\nu})+A_-(\bar{\nu})]}\} \qquad (2.11)$$

iv. At the detector:

The electronic output of the detector, a voltage, is proportional to the time-averaged intensity. Thus, an integration over a whole period of the time variable, t, is necessary. The third term of Equation (2.11) goes to zero, because,

$$\int_0^{2\pi} [\cos^2(\delta+0.5\alpha)-\sin^2(\delta+0.5\alpha)]\ dt = 0 \qquad (2.12)$$

So,

$$I = 0.5E_o^2\{[1+\sin\alpha]10^{-A_+(\bar{\nu})} + [1-\sin\alpha]10^{-A_-(\bar{\nu})}\} \qquad (2.13)$$

Hereafter, the signal is converted to voltage, $V(\bar{\nu})$.

$$V(\bar{\nu}) = 0.5E_o^2\{[1 + \sin\alpha]10^{-A_+(\bar{\nu})} + [1 - \sin\alpha]10^{-A_-(\bar{\nu})}\}$$
$$= 0.5E_o^2\{[10^{-A_+(\bar{\nu})}+10^{-A_-(\bar{\nu})}]+\sin\alpha[10^{-A_+(\bar{\nu})}-10^{-A_-(\bar{\nu})}]\}$$
$$= V_{DC}(\bar{\nu}) + V_{AC}(\bar{\nu}) \qquad (2.14)$$

where,

$$V_{DC}(\bar{\nu}) = 0.5E_o^2[10^{-A_+(\bar{\nu})} + 10^{-A_-(\bar{\nu})}] \qquad (2.15)$$

is the retardation independent part of the $V(\bar{\nu})$, while

$$V_{AC}(\bar{\nu}) = 0.5E_o^2 \sin\alpha[10^{-A_+(\bar{\nu})} - 10^{-A_-(\bar{\nu})}] \qquad (2.16)$$

is the retardation dependent part.

Only the ratio of $V_{AC}(\bar{\nu})$ and $V_{DC}(\bar{\nu})$ is of importance to a dichroism measurement for the reasons that will be obvious later. Also, by taking the ratio, all the proportional coefficients involved in the conversions from the light electric potential to the light intensity and from the intensity to the output voltage of the detector signal will be canceled.

$$\frac{V_{AC}(\bar{\nu})}{V_{DC}(\bar{\nu})} = \sin\alpha \; \frac{10^{-A_+(\bar{\nu})} - 10^{-A_-(\bar{\nu})}}{10^{-A_+(\bar{\nu})} + 10^{-A_-(\bar{\nu})}} \qquad (2.17)$$

$$= \sin\alpha \; \frac{10^{-A_+(\bar{\nu})} - 10^{-A_-(\bar{\nu})}}{10^{-A_+(\bar{\nu})} + 10^{-A_-(\bar{\nu})}} \times \frac{10^{[0.5A_+(\bar{\nu})+0.5A_-(\bar{\nu})]}}{10^{[0.5A_+(\bar{\nu})+0.5A_-(\bar{\nu})]}}$$

$$= \sin\alpha \; \frac{10^{0.5[A_-(\bar{\nu})-A_+(\bar{\nu})]} - 10^{-0.5[A_-(\bar{\nu})-A_+(\bar{\nu})]}}{10^{0.5[A_-(\bar{\nu})-A_+(\bar{\nu})]} + 10^{-0.5[A_-(\bar{\nu})-A_+(\bar{\nu})]}}$$

Substituting $\Delta A(\bar{\nu})=A_{-}(\bar{\nu})-A_{+}(\bar{\nu})$, and using $10^{x}=e^{2.303x}$,

$$\frac{V_{AC}(\bar{\nu})}{V_{DC}(\bar{\nu})} = \sin\alpha \; \frac{e^{0.5[2.303\Delta A(\bar{\nu})]} - e^{-0.5[2.303\Delta A(\bar{\nu})]}}{e^{0.5[2.303\Delta A(\bar{\nu})]} + e^{-0.5[2.303\Delta A(\bar{\nu})]}} \qquad (2.18)$$

Substituting

$$\tanh(x) = \frac{e^{x} - e^{-x}}{e^{x} + e^{-x}} \qquad (2.19)$$

Equation (2.20) is obtained

$$\frac{V_{AC}(\bar{\nu})}{V_{DC}(\bar{\nu})} = \sin\alpha \; \tanh[1.152 \; \Delta A(\bar{\nu})] \qquad (2.20)$$

Since $\Delta A(\bar{\nu})$ is very small (less than 10^{-4}), the hyperbolic tangent function can be replaced by its argument.

$$\frac{V_{AC}(\bar{\nu})}{V_{DC}(\bar{\nu})} = \sin\alpha \; [1.152 \; \Delta A(\bar{\nu})] \qquad (2.21)$$

It is, therefore, clear that once $V_{DC}(\bar{\nu})$ and the corresponding $V_{AC}(\bar{\nu})$ are measured, the VCD signal ($\Delta A(\bar{\nu})$) can be easily calculated. However, it must also be noted that only if $\Delta A(\bar{\nu})$ is very small

(smaller than 0.01), will the simple proportional relation of Equation (2.21) stand. This should apply for samples in most liquid solutions, in which small VCD signals are observed due to relatively low concentrations and random orientation of the molecules. For a large $\Delta A(\bar{\nu})$, as in some solid samples, Equation (2.20) must be used.

2.1.3 Theory of Operation - Electronics

The electronics of the VCD instrument is designed to extract the $V_{DC}(\bar{\nu})$ and the $V_{AC}(\bar{\nu})$ from the $V(\bar{\nu})$, the total detector signal. As a result, the signal processing scheme is different from that of a conventional infrared spectrophotometer. Figure 6 is the electronic layout of a dispersive VCD. The detector signal is separated into two paths. One processes the transmission signal, $V_{DC}(\bar{\nu})$, which is the same as in a normal IR instrument. The other one processes the differential signal, $V_{AC}(\bar{\nu})$. Since $\Delta A(\bar{\nu})$ is proportional to the ratio of $V_{AC}(\bar{\nu})$ over $V_{DC}(\bar{\nu})$, the set-up described can directly measure $\Delta A(\bar{\nu})$ instead of having to measure an $A_{-}(\bar{\nu})$ and the corresponding $A_{+}(\bar{\nu})$ and then subtracting one from the other. Once again, a direct absorption subtraction method would

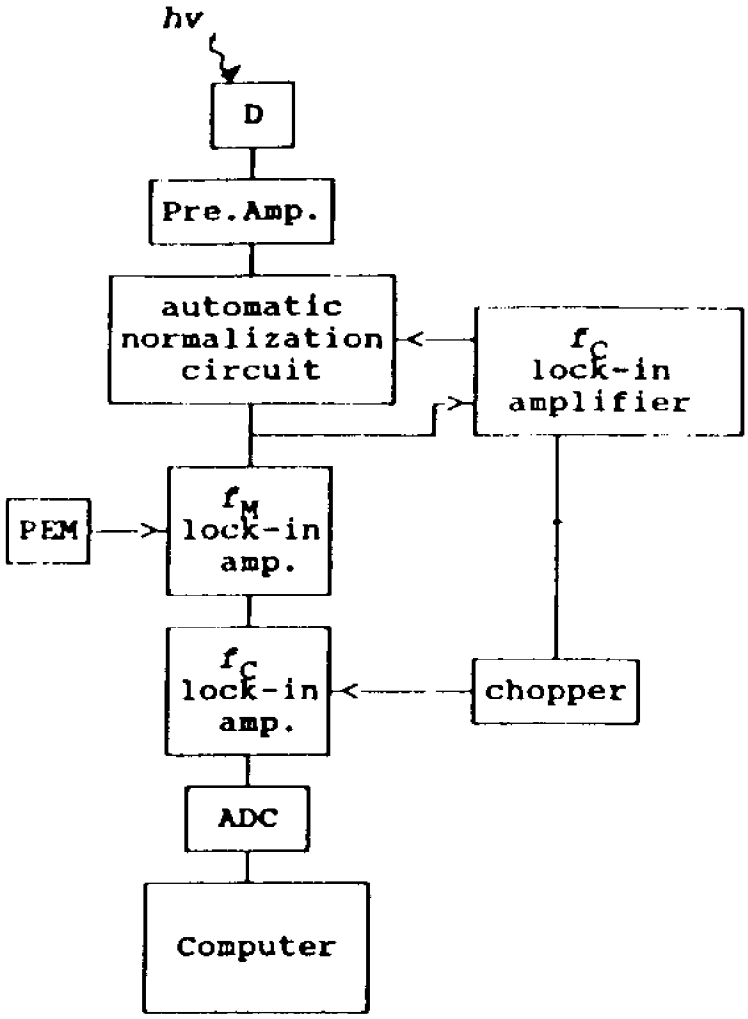

Figure 6. Electronic Block Diagram of a Early Version of Dispersive VCD (*cf.* text)

have demanded a large (greater than 10^6) linear dynamic range as well as extremely low noise (S/N > 10^5) from the detector, the amplifiers and the other electronics.

The $V_{DC}(\bar{\nu})$ signal is obtained by passing the detector output through a low-pass filter to get rid of the $V_{AC}(\bar{\nu})$ signal. Subsequently, it is demodulated at the chopper frequency, f_C, using a phase-sensitive detector (lock-in amplifier). The $V_{AC}(\bar{\nu})$ signal is doubly demodulated in series, first at the PEM frequency, f_M, then at the chopper frequency, f_C.

For the double demodulation to work well, the two modulation frequencies should be as far apart as possible (at least two orders of magnitude). Usually, f_M is in the neighborhood 50 kHz, while f_C is less than 100 Hz. Because of the high frequency modulation, one must be careful to select a detector and preamplifiers whose response time is shorter than $1/f_M$. Thus, the IR detector should have a response time on the order of microsecond (10^{-6} second), or faster, to follow adequately the high frequency intensity modulation.

Up to now we have not discussed the $\sin\alpha$ term in Equation (2.21). To solve the equation, this term must be solved first. α is the retardation generated by the photoelastic modulator to produce right and

left circularly polarized light waves. (One would assume that α should be close to $\pm\pi/2$.) In fact, α is not a constant; instead, it tracks the PEM modulation, and varies sinusoidally from $+\pi/2$ to $-\pi/2$ and back, at frequency f_M.

$$\alpha = \alpha_o \sin(2\pi f_M t) \qquad (2.22)$$

Here, α_o is the maximum retardation, a constant to be determined. Thus,

$$\sin\alpha = \sin[\alpha_o \sin(2\pi f_M t)] \qquad (2.23)$$

The sine function of an embedded sine function can be evaluated using Bessel functions. Reference 40 has a detailed discussion of Bessel functions. For our application, the useful results are the following:

$$\cos[X \sin(\theta)] = J_o(X) + 2 \sum_{n=o}^{+\infty} J_{2n}(X) \cos(2n\,\theta) \qquad (2.24)$$

$$\sin[X \sin(\theta)] = 2 \sum_{n=1}^{+\infty} J_{2n-1}(X) \sin[(2n-1)\theta] \qquad (2.25)$$

$$J_n(X) = \sum_{k=0}^{\infty} \frac{(-1)^k (0.5X)^{n+k}}{k!\,\Gamma(n+k+1)} \qquad (2.26)$$

For integer n and k, $\Gamma(n+k+1) = (n+k)!$

Figure 7 is a diagram of $J_0(X)$, $J_1(X)$ and $J_2(X)$. Notice that $J_1(X)$ has a maximum of 0.5819 at X = 1.84, whereas sinX peaks at $0.5\pi = 1.57$. The value of $J_0(1.84)$ is 0.4.

In the dichroism experiments, $J_0(X)$, $J_1(X)$ and $J_2(X)$ are of significance. $J_0(X)$ is wanted in both the circular dichroism (CD) and the linear dichroism (LD). CD sometimes needs $J_0(\alpha_0)$ for magnitude calibration. $J_1(X)$ accounts for signal in the circular dichroism measurement because the sine function of Equation (2.23) in CD can be solved by Equation (2.25), not (2.24). As a result, only the odd term Bessel functions survive. $J_2(X)$ is essential in the linear dichroism (LD) measurement because a derivation of this measurement would lead to a $\cos\alpha$ term, which could be solved by Equation (2.24) with only the even term Bessel functions survive. The higher order terms in Equations (2.24) or (2.25) will be filtered out electronically by a lock-in amplifier tuned to the first order frequency (0) in CD measurement, or to the second order frequency (20) in LD measurement. As a result, in VCD we get

$$J_n(x) = \sum_{s=0}^{\infty} \frac{(-1)^s}{s!(n+s)!}\left(\frac{x}{2}\right)^{n+2s} = \frac{x^n}{2^n n!} - \cdots$$

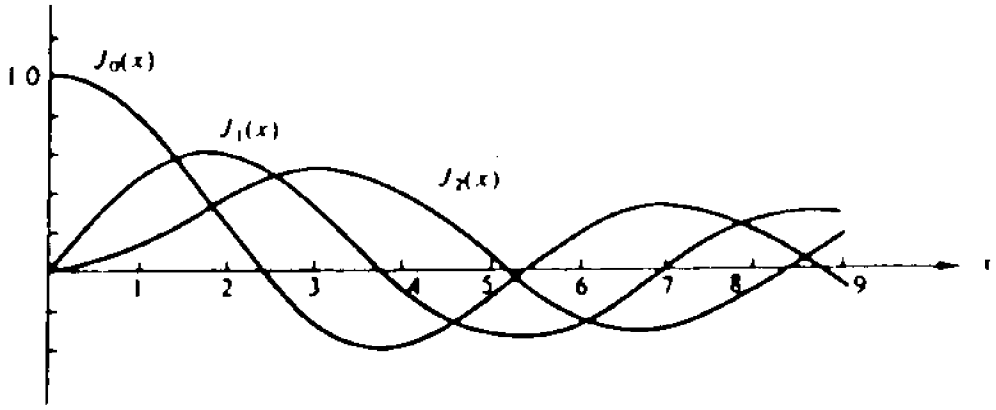

Figure 7. Bessel Functions, $J_0(X)$, $J_1(X)$, and $J_2(X)$ (from ref.[40] by Arfken)

$$\mathrm{Sin}[\alpha_o \sin(2\pi f_M t)] = 2J_1(\alpha_o)\sin(2\pi f_M t) \qquad (2.27)$$

where $J_1(\alpha_o)$ is the first order Bessel function. Obviously, α_o is chosen to have the maximum $J_1(\alpha_o)$ for a maximum observable signal. Therefore, $\alpha_o = 1.84$. Equation (2.21) becomes,

$$\frac{V_{AC}(\bar{\nu})}{V_{DC}(\bar{\nu})} = 2\ J_1(1.84)[\ 1.152\ \Delta A(\bar{\nu})] \qquad (2.28a)$$

$$= 2 \times 0.5819 \times 1.152\ \Delta A(\bar{\nu})$$

$$= 1.340\ \Delta A(\bar{\nu}) \qquad (2.28b)$$

The term $\sin(2\pi f_M t)$ disappears because the output of the lock-in amplifier, tuned to f_M, is a direct current (DC) signal proportional to the amplitude of the $\sin(2\pi f_M t)$ term. Here, by taking the ratio of $V_{AC}(\bar{\nu})/V_{DC}(\bar{\nu})$, the VCD spectrum, $\Delta A(\bar{\nu})$, is acquired rather simply. This ratio-taking process is called normalization of $V_{AC}(\bar{\nu})$.

2.1.4 Calibration of VCD Instrument[37,39]

In addition to the regular wavenumber calibration by a polystyrene film, the magnitude of a VCD spectrum needs to be calibrated as well. That is

because in a VCD measurement the ratio $\Delta A(\bar{\nu})/A(\bar{\nu})$, called the anisotropy, g, is a critical quantity. The anisotropy is used for identification of an optically active chemical and the determination of its optical purity.

The calibration is carried out by inserting a birefringent plate (B) and a second polarizer (analyzer, A) after the PEM instead of a sample. Figure 8a is the optical scheme, and 8b indicates the optical axes of the components. Plate B has its fast axis parallel to the X axis and its slow axis parallel to the Y axis. The second polarizer is aligned with the Y' axis and is thus perpendicular to the first polarizer (P).

Recalling Equation (2.3), the electric potential of the light leaving the PEM can be described by

$$\mathbf{E} = \mathbf{i}\, E_o \cos\delta + \mathbf{j}\, E_o \cos(\delta + \alpha) \qquad (2.29)$$

Again, α is the phase retardation induced by PEM. After passing the birefringent plate, which induces yet another phase shift, β, at a given wavelength,

$$\mathbf{E} = \mathbf{i}\, E_o \cos\delta + \mathbf{j}\, E_o \cos(\delta + \alpha + \beta) \qquad (2.30)$$

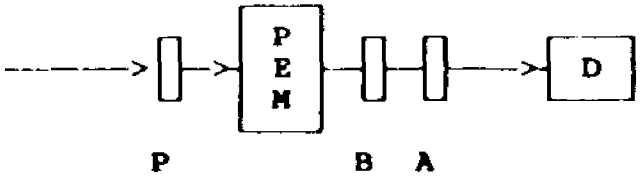

P: polarizer
B: birefringent plate, quarter-wave retardation plate
A: analyzer (second polarizer).

a) optics set-up

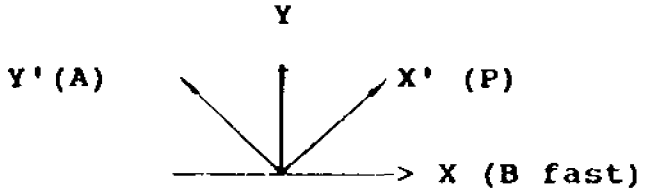

b) optical axes of first scan

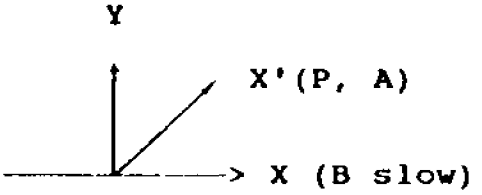

c) optical axes of second scan

Figure 8. Calibration Scheme

Following a derivation similar to that for Equation (2.4), replacing α by $(\alpha + \beta)$, one obtains,

$$\mathbf{E} = 1.414\hat{\imath}' E_o \cos[0.5(\alpha+\beta)]\cos[\delta+0.5(\alpha+\beta)] - 1.414\hat{\jmath}' E_o \sin[0.5(\alpha+\beta)]\sin[\delta+0.5(\alpha+\beta)] \qquad (2.31)$$

Since A only allows the $\hat{\jmath}'$ term to pass,

$$\mathbf{E} = -1.414\hat{\jmath}' E_o \sin[0.5(\alpha+\beta)]\sin[\delta+0.5(\alpha+\beta)] \qquad (2.32)$$

Therefore, the time-averaged intensity, $I(\bar{\nu})$, at the detector is given by

$$\begin{aligned} I(\bar{\nu}) &= 2E_o^2 \sin^2[0.5(\alpha+\beta)]\,\pi \\ &= \pi E_o^2 (1 - \cos\alpha\cos\beta + \sin\alpha\sin\beta) \\ &= \pi E_o^2 \{1 - \cos[\alpha_o \sin(2\pi f_M t)]\cos\beta \\ &\quad + \sin[\alpha_o \sin(2\pi f_M t)]\sin\beta\} \end{aligned} \qquad (2.33)$$

Substituting the Bessel function (Equation (2.25)), and considering that the lock-in amplifiers filters out all terms except the first order, the detector output, $V(\bar{\nu})$, becomes

$$V(\bar{\nu}) = \pi E_o^2[1 - J_o(\alpha_o)\cos\beta + 2J_1(\alpha_o)\sin(2\pi f_M t)\sin\beta] \qquad (2.34)$$

Therefore, after the lock-in amplifiers, the ratio of $V_{AC}(\bar{\nu})/V_{DC}(\bar{\nu})$ is

$$\frac{V_{AC}(\bar{\nu})}{V_{DC}(\bar{\nu})} = \frac{2J_1(\alpha_o)\sin\beta}{1 - J_o(\alpha_o)\cos\beta} \qquad (2.35)$$

Comparing to Equation (2.28a), the left sides of both equation are the same. Therefore,

$$1.152\ \Delta A(\bar{\nu}) = \frac{\sin\beta}{1 - J_o(\alpha_o)\cos\beta} \qquad (2.36)$$

If β is known, $\Delta A(\bar{\nu})$ can be calibrated since $J_o(\alpha_o)$ is already a known constant. A particularly practical example is that using a quarter-wave plate, $\beta = \pi/2$ (90°) at a particular wavelength. Equation (2.36) becomes

$$1.152\ \Delta A(\bar{\nu}) = 1$$

$$\Delta A(\bar{\nu}) = 0.868 \qquad (2.37)$$

The $\Delta A(\bar{\nu})$ scale, therefore, is calibrated at that wavelength.

However, the action of a quarter-wave plate is wavelength dependent. It can only retard $\pi/2$ at one

exact wavelength on the whole spectrum. The certainty of this position relies solely on the manufacturer's specification. Furthermore, there are only a few wavelengths at which quarter-wave plates are available. Thereby, the above calibration method is not practical. However, there is a way to achieve calibration without knowing the exact wavelength of the retardation plate.

First, a VCD scan is run over the entire region of interest with the same settings as above for the plate (B) and the second polarizer. Equation (2.35) still stands for this situation.

Second, another VCD scan over the same region is collected with both the plate (B) and the second polarizer (A) being rotated by 90° (*cf.* Figure 8c). Thus, two parameters have been changed here, comparing to the first run: i) The birefringent plate now retards the X axis, which was formerly the fast axis. So the phase shift induced by the plate is $-\beta$ instead of β. The total phase shift becomes $(\alpha-\beta)$ instead of $(\alpha+\beta)$. ii) The second polarizer allows only 1′ component to pass when deriving from Equation (2.31) to (2.32). Figure 9 depicts a sample spectra of the two calibration scans, plotted on the same graph.

After A, the electric potential is (recalling Equation (2.31)),

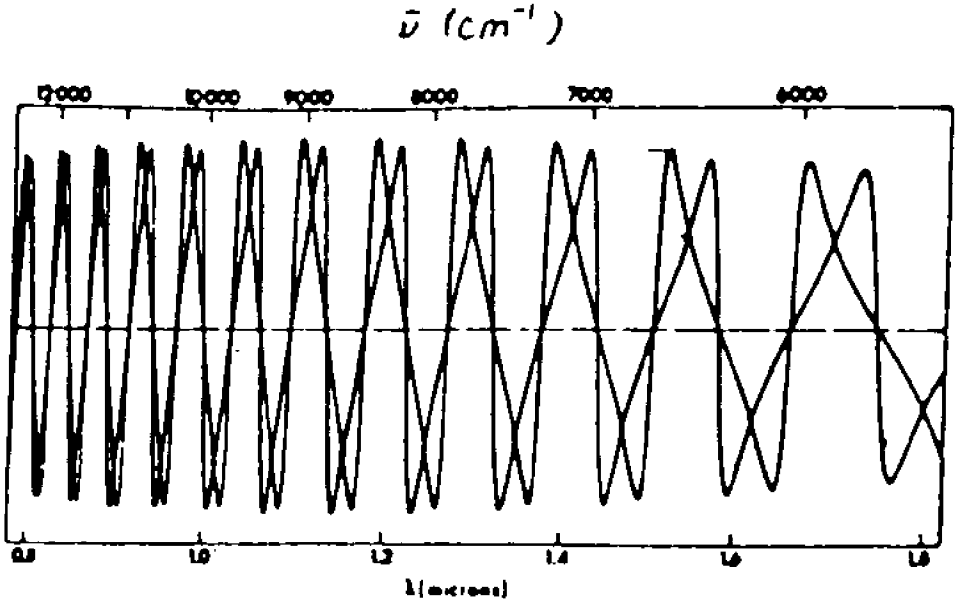

Figure 9. Sample Instrumental Calibration Spectra (from ref.[39] by Nafie *et al*)

$$E = 1.4141\,E_o \cos[0.5(\alpha-\beta)]\cos[\delta+0.5(\alpha-\beta)] \qquad (2.38)$$

The time-averaged intensity at the detector is given by

$$\begin{aligned} I(\bar{\nu}) &= 2E_o^2 \cos^2[0.5(\alpha-\beta)]\,\pi \\ &= \pi E_o^2 \,(\, 1 + \cos\alpha\cos\beta + \sin\alpha\sin\beta \,) \\ &= \pi E_o^2 \,\{\, 1 + \cos[\,\alpha_o \sin(2\pi f_M t)\,]\cos\beta \\ &\qquad + \sin[\,\alpha_o \sin(2\pi f_M t)\,]\sin\beta \,\} \end{aligned} \qquad (2.39)$$

After the same considerations as in the previous discussion, we obtain

$$\frac{V_{AC}(\bar{\nu})}{V_{DC}(\bar{\nu})} = \frac{2J_1(\alpha_o)\sin\beta}{1 + J_o(\alpha_o)\cos\beta} \qquad (2.40)$$

At the crossing points of the two spectra in Figure 9 the left sides of Equation (2.35) and Equation (2.40) are equal. Thus,

$$\frac{2J_1(\alpha_o)\sin\beta}{1 - J_o(\alpha_o)\cos\beta} = \frac{2J_1(\alpha_o)\sin\beta}{1 + J_o(\alpha_o)\cos\beta} \qquad (2.41)$$

Equation (2.41) has two solutions:

$$\text{i.}\quad 2J_1(\alpha_o)\sin\beta = 0 \qquad (2.42)$$

That means, $\Delta A(\bar{\nu}) = 0$. Those are the points on the zero line (*cf.* Figure 9). Since $J_1(\alpha_o) = J_o(1.84) = 0.5819 \neq 0$, so,

$$\sin\beta = 0, \tag{2.43}$$

$$\beta = \pi \pm n\pi \quad (n = 0,1,2...) \tag{2.44}$$

At these zero crossing points, the plate (B) retards the phase by an integral multiple of π (one half of the wavelength) of the infrared radiation.

ii. $$2J_1(\alpha_o)\sin\beta \neq 0, \tag{2.45}$$

That means $\Delta A(\bar{\nu}) \neq 0$. These are the non-zero crossing points. Therefore, it must be that

$$\cos\beta \; J_o(\alpha_o) = 0 \tag{2.46}$$

since $J_o(\alpha_o) = J_o(1.84) = 0.5819 \neq 0$,

$$\cos\beta = 0, \tag{2.47}$$

$$\beta = \pm 0.5\pi \pm n\pi \quad (n = 0,1,2...) \tag{2.48}$$

At these points

$$\frac{V_{AC}(\bar{\nu})}{V_{DC}(\bar{\nu})} = \pm\ 2\ J_1(\alpha_o) \qquad (2.49)$$

Comparing with Equation (2.28a), we find

$$1.152\ \Delta A(\bar{\nu}) = \pm\ 1$$

$$\Delta A(\bar{\nu}) = \pm\ 0.868 \qquad (2.50)$$

Those are the two groups of non-zero crossing points. At any of these points, the absolute value of the sensitivity of the instrument is known since the actual VCD has to be 0.868. One calibration curve will be a smooth curve linking all the positive non-zero crossing points covering the entire wavelength range. Any point on the curve must have a $\Delta A(\bar{\nu})$ value of 0.868. Any points on the other calibration curve linking all the negative non-zero points must have a $\Delta A(\bar{\nu})$ value of -0.868.

One other important fact being realized from the discussion of this calibration procedure is the sensitivity of the VCD measurement toward artifacts. An artifact can be generated by any optical element which alters the polarization state of light in combination with an intensity reduction, for example, by the solvent absorption because the technique of VCD measures precisely the difference in absorption

as the polarization state of light periodically changes. In the calibration setup, this sensitivity is utilized to serve us. The retardation plate alters the light polarization, while the second polarizer reduces light intensity (acting as an absorbing substance). As a result, an artificial VCD signal with a known magnitude is produced. However, any other unwanted signals generated due to the sensitivity would be artifacts.

To eliminate this kind of artifacts, the sources of reducing light intensity and the sources of altering light polarization must first be identified. In additional to solvent absorption, some other sources may also be likely to cause light reduction, such as the absorption by the water vapor in the air, and by the transmission optical elements (*i.e.* cell windows, lenses, and detector window). Some likely sources for altering the polarization state of light are: i) lenses and windows, which are usually stressed when polishing the surfaces, acting as a retardation plate; ii) off-axial mirrors, particularly paraboloidal and ellipsoidal mirrors, changing the light polarization upon reflection; and iii) detectors, often exhibiting polarization sensitivity.

2.2 Fourier Transform Infrared (Vibrational) Circular Dichroism with a Photoelastic Modulator (FT-VCD-PEM)

Fourier Transform Infrared (FT-IR) spectroscopy has revolutionized the field of infrared absorption spectroscopy, producing spectra of high signal-to-noise ratio in a much shorter data collection time the dispersive methods[41,42].

FT-IR spectroscopy demonstrates two major advantages over its dispersive counterpart: Fellgett's (multiplexing) advantage, which is due to the fact that a wide wavenumbers range can be measured all at once; and Jacquinot's (throughput) advantage, due to the fact that an interferometer can allow a large total light flux to reach the detector. The detector noise, therefore, is very small compared to the total signal. Since the detector is a major source of noise in the infrared, FT-IR spectroscopy produces spectra with a superior signal-to-noise ratio. One other FT-IR advantage is important for differential measurement. This is Connes' advantage, the excellent wavenumber accuracy (better than 0.01 cm^{-1}), which permits spectra to be subtracted accurately. Moreover, FT-IR spectra can have a high resolution (better than 2 cm^{-1}) throughout the entire spectral region. For a dispersive instrument, to

maintain a consistently high resolution, the exit slit width has to be adjusted according to the dispersion of the grating, which varies as the grating turns or when switching to another gratings as needed to cover a wide spectral range.

It was natural that Fourier transform spectroscopy should "invade" the field of vibrational circular dichroism not long after the dispersive VCD was operational. The reasons were two folds. First, the FT-IR technique had been matured and had begun to dominate the infrared instrumentation market by the late 70s. Second, VCD had been proved to be an undeniable new road to the understanding of molecular structures. Nafie and Diem first proposed the theory of FT-VCD-PEM[43] and reported the first results[44]. Others soon followed[6,7,45].

Very much like the dispersive VCD, the first FT-VCD utilized a conventional FT-IR spectrometer with the necessary components added to the sample compartment to produce the light modulation. It also employed a PEM and a lock-in amplifier set-up. Figure 10 is the block diagram of an FT-IR-VCD, published in reference[44] by Nafie *et al*. The measurement still consists of observing $V_{DC}(\bar{\nu})$, and $V_{AC}(\bar{\nu})$.

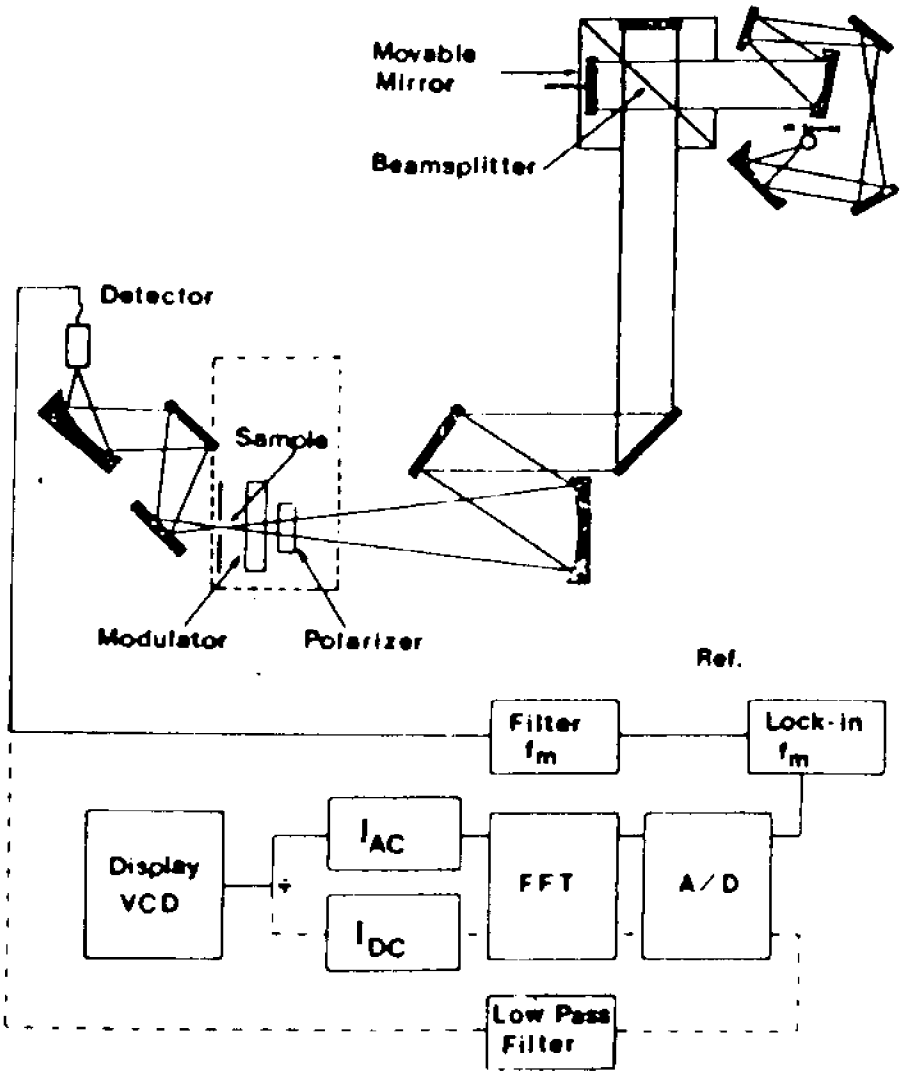

Figure 10. Block Diagram for Fourier Transform VCD with a Photoelastic Modulator (from ref.[44] by Nafie *et al*)

$$V(\bar{\nu}) = V_{DC}(\bar{\nu}) + V_{AC}(\bar{\nu}) \qquad (2.51)$$

where

$$V_{DC}(\bar{\nu}) = 0.5V_o(\bar{\nu})[10^{A_+(\nu)} + 10^{A_-(\nu)}] \qquad (2.52)$$

$$V_{AC}(\bar{\nu}) = 0.5V_o(\bar{\nu})[10^{A_+(\nu)} - 10^{A_-(\nu)}]\sin\alpha \qquad (2.53)$$

$$V_o = E_o^2 \qquad (2.54)$$

The signal is modulated at the PEM frequency, as in the dispersive VCD. Since it is also modulated at the Fourier frequency, the FT-VCD-PEM sometimes is called a doubly modulated FT-IR.

In a Michelson interferometer, the movable mirror undergoes a uniform translation motion at a velocity, V, . This action produces a time-dependent intensity, called an interferogram. Due to the periodic constructive and destructive phase interference, the infrared radiation at each wavenumber (frequency) in the interferogram oscillates sinusoidally at its own Fourier frequency, $2V\bar{\nu}$.

An interferogram can be expressed as a function of the path difference of the two mirrors, $\delta_x = 2Vt$ (t is the time the movable mirror has moved in one scan), by the following equation:

$$V(\delta_x) = \int_0^\infty V(\bar{\nu})\cos(2\pi\bar{\nu}\delta_x)\,d\bar{\nu} \qquad (2.55)$$

When an absorbing sample is placed in the beam, $V(\bar{\nu})$ can be substituted by Equation (2.51),

$$V(\delta_x) = \int_0^\infty [V_{DC}(\bar{\nu})+V_{AC}(\bar{\nu})]\cos(2\pi\bar{\nu}\delta_x)\,d\bar{\nu} \qquad (2.56)$$

Similar to a dispersive VCD, $V_{AC}(\delta_x)$ and $V_{DC}(\delta_x)$ are extracted separately, as the detector output is split into two paths. $V_{AC}(\delta_x)$ is demodulated at the PEM frequency, f_M, and then changed to digital form via an analog-to-digital converter (ADC) and stored. $V_{DC}(\delta_x)$ first passes a low-pass filter, to get rid of $V_{AC}(\delta_x)$, before being converted to a digital form and stored.

$$V_{DC}(\delta_x)= \int_0^\infty 0.5V_o(\bar{\nu})[10^{-A_+(\nu)}+10^{-A_-(\nu)}]\cos(2\pi\bar{\nu}\delta_x)\,d\bar{\nu} \qquad (2.57)$$

and

$$V_{AC}(\delta_x)= \int_0^\infty 0.5V_o(\bar{\nu})2J_1(\alpha_o)[10^{-A_+(\nu)}-10^{-A_-(\nu)}]\cos(2\pi\bar{\nu}\delta_x)\,d\bar{\nu} \qquad (2.58)$$

The respective Fourier transformation of Equations

(2.57) and (2.58) will yield $V_{DC}(\bar{\nu})$ and $V_{AC}(\bar{\nu})$. The ratio of the two will give a VCD spectrum, the same one observed from a dispersive VCD design (Equation (2.28)).

$$\frac{V_{AC}(\bar{\nu})}{V_{DC}(\bar{\nu})} = 2J_1(\alpha_o)[1.152\ \Delta A(\bar{\nu})] \qquad (2.42)$$

Because the Fourier transformation can only be done with an entire set of data (interferogram), the $V_{DC}(\delta_x)$ and $V_{AC}(\delta_x)$ were collected separately with the ADC set-up in Figure 10, and stored separately. Afterward, they are respectively transformed into $V_{DC}(\bar{\nu})$ and $V_{AC}(\bar{\nu})$. They could be collected simultaneously if two analog-to-digital converters were used.

Of the advantages FT spectroscopy has over its dispersive counterpart in a normal absorption spectroscopy, only a few were carried over to FT-VCD-PEM due to a variety of technical limitations. Some improvements, such as a better signal-to-noise ratio and a wider spectral range, have been achieved. Yet the magnitude of those improvements has not been as great as expected. Facing some new challenging problems, FT-VCD-PEM has not yet dominated the field of VCD, as did FT-IR in absorption spectroscopy.

This is because there are several serious technical problems in FT-VCD-PEM. First, the use of a PEM limits the coverage of the FT-VCD experiment, since the PEM is designed to produce the circularly polarized light waves at one setting, *i.e.*, one wavelength only, depending on the setting of α_o. In a dispersive VCD, one adjusts the α_o setting accordingly as the monochromator scans. In FT-VCD-PEM, however, the multiplexing nature does not allow any PEM adjustment during a scan. α_o is set at one wavenumber, usually the middle of a chosen region. The result is that the light waves of other wavenumber are only elliptically polarized. The farther away from the selected wavenumber, the worse the distortion of a circular polarization becomes. As a consequence, amplitude calibration is a must to correct the distorted spectra. One way, albeit undesirable, to lessen this problem is to cut the covered range of FT-VCD-PEM. Obviously, this approach also lowers the multiplexing advantage.

Second, in most commercial FT-IR instruments, the off-axial ellipsoidal or paraboloidal mirrors are used to focus a large, collimated light beam onto a small image spot on the high sensitivity detector. When a FT-VCD-PEM instrument is built on such a FT-IR instrument, a large offset on the spectral baseline

usually appears in VCD spectra. This type of artifact is called the polarization bias. As discussed in the previous section, this is due to the sensitive nature of VCD towards any light intensity variations generated by absorption combining with light polarization changes. The offset could be as large as ten times the VCD signal, and is not uniform throughout the spectrum. Thus, the offset has forced FT-VCD-PEM instrument users to run either the racemate or the other enantiomer of the samples under the same conditions to determine the true VCD baseline, which is subsequently used to correct the original spectrum. This method severely limits the application of VCD, as the enantiomeric or the racemic forms are not always available, particularly for some large biological molecules. Keiderling and Malon have reduced this problem by replacing the ellipsoidal mirrors with a lens and obtained satisfactory results[46].

Third, the dynamic range of several electronic components, such as the detector, the lock-in amplifier and the analog-to-digital converter (ADC), also restrict FT-VCD-PEM from fully exercising its advantages. This problem arises since VCD measures very small changes in absorbance (10^{-3}-10^{-6} absorbance unit) in the presence of a large signal, especially

at the centerburst in the interferogram. Furthermore, the gain of the lock-in amplifier has to be set to accommodate the centerburst, which may be two orders of magnitude greater than the peaks nearby in the interferogram. As a result, the sensitivity for measuring the nearby peaks must be somewhat sacrificed. A similar limitation also exists at the ADC, which is typically a 16-bit converter with a dynamic range of $1:2^{16} = 1:65536$. Obviously, it is difficult to extract a VCD signal of 10^{-5} or less of the total signal from a converter with a dynamic range less than five orders of magnitude while still expecting a reasonable signal- to-noise ratio. Reducing the intensity of the centerburst by cutting down the frequency coverage via an optical filter seems to be the only way to solve this problem. On account of these restraints, the FT-VCD-PEM generally covers only about 500 cm^{-1} or less.

For the same reasons mentioned earlier when discussing the demodulation process, the PEM modulation frequency, f_M, should be two orders of magnitude higher than the Fourier frequency, $2\pi\bar{\nu}\delta_x/t$. This is because the minimum time constant of the lock-in amplifier requires that difference in order to separate the two frequencies effectively.

In addition to the above hardware problems,

there are also some software problems. A normal VCD spectrum exhibits both positive and negative peaks, and the sum of all peak areas is close to zero. This behavior is called conservative. This was predicted theoretically and has been observed experimentally. As a result, an ideal VCD interferogram does not have a centerburst. Instead, it has two groups of peaks which are mirror images of each other, and are symmetrical about the zero-path-difference (ZPD) position. The ZPD position is where the centerburst occurs normally in an IR absorption interferogram. Therefore, the standard Fourier transform algorithm (Mertz and Forman method[41,49]) is inapplicable since it looks for an absolute maximum as the centerburst and treats the δ_x at the maximum as the zero-path-difference position[41].

This problem has been dealt with in several ways. One is called the "stored phase" method. One runs a normal IR absorption first and stores the spectrum before running its VCD. The phase for transforming the IR absorption spectrum is stored and later used in locating the ZPD position of the VCD spectrum. To prevent any changes caused by instrumental fluctuation, one should run the absorption and VCD spectra under the same conditions as near in

time as practicable. This method has been widely used, however, it has been found that quite often the transferred phase is not exactly correct[47]. The possible cause of it may be in the electronic paths of $V_{AC}(\delta_x)$ and $V_{DC}(\delta_x)$. Frequently, the deviation (phase shift) is small, sometimes as small as one data point. Even such a minute phase shift leads to a drastically different spectrum after Fourier transformation, as being found by many[7,48,49]. Therefore, other non-stored-phase methods have been developed.

Two methods are mostly acceptable in treating the transformation of the VCD interferogram. Keiderling *et al.*[46] and de Haseth *et al.*[49] separately demonstrated that the ZPD position can be located by utilizing the symmetric character of the VCD interferogram. Modifications to the software of the FT-VCD have been developed[49,50]. Nafie and coworkers took advantage of an imperfect VCD alignment, using the polarization bias to produce a large centerburst in the VCD interferogram. This method, however, requires enantiomeric or racemic forms to correct the baseline since the polarization bias is usually ten times larger than the VCD signals[48].

In Chapter Four, there will be further comparisons of advantages and disadvantages of dispersive VCD

and FT-VCD-PEM, with some specific results from the dispersive instruments at Hunter College and published results from FT-VCD-PEM.

2.3 Fourier Transform Infrared VCD with a Polarizing Michelson Interferometer (FT-VCD-PMI)

The creation of FT-VCD-PMI was the result of a desire to build a VCD instrument without a photoelastic modulator, to avoid the problems discussed in the last section associated with using a PEM in FT-IR method. Also, FT-VCD-PMI permits an expansion of the frequency range, particularly going down to far infrared region. Prior to the development of this type of instrument, vibrational circular dichroism had not been reported below 600 cm^{-1}. Instruments using PEMs can only go down to the limit of the crystal transparency (*e.g.*, CaF_2: 1100 cm^{-1}; ZnSe: 600 cm^{-1}; CdS: 400 cm^{-1}). Other crystal materials known to be transparent below 600 cm^{-1} have properties not suitable for a PEM, such as being too soft or hygroscopic.

Another reason to avoid using a PEM is its inability to produce perfect modulation at all wavelengths simultaneously. Therefore, as stated in the previous section, it is necessary to run an amplitude-calibration as well as to run the enantiomer or racemate for the baseline correction of the VCD spectrum. That is more than double the data acquisition time. As a result, a non-PEM method is desired.

The concept of the polarizing Michelson Interferometer (PMI), or Martin-Puplett Interferometer (MPI), first appeared more than twenty years ago[51, 52]. It is particularly suitable for the far-infrared region. Dignam and Baker first suggested using a PMI for VCD in 1981[53]. However, it took quite some time for the PMI principle to be recognized by VCD experimentalists. Polavarapu developed the theoretical formalism[54,55], and published a few calibration spectra to demonstrate the feasibility of this approach. Nafie *et al.* published the first experimental results on α-pinene in 1990[56].

The PMI is a modified Michelson Interferometer (*cf.* Figure 11a). The dielectric beamsplitter, normally used in the Michelson Interferometer, is replaced by a polarizing grid beamsplitter (B), and the flat mirrors by the roof-top mirrors (M_m and M_f). A roof-top mirror consists of two flat, front-surface-reflecting mirrors that are set perpendicularly to each other.(*cf.* Figure 11a) Additionally, a polarizer (P) is positioned at the entrance of the interferometer and another polarizer, called the analyzer (A), is placed immediately after the interferometer. The axis of P is 45° with respect to the grid direction of B. As a result, the linearly polarized beam leaving P

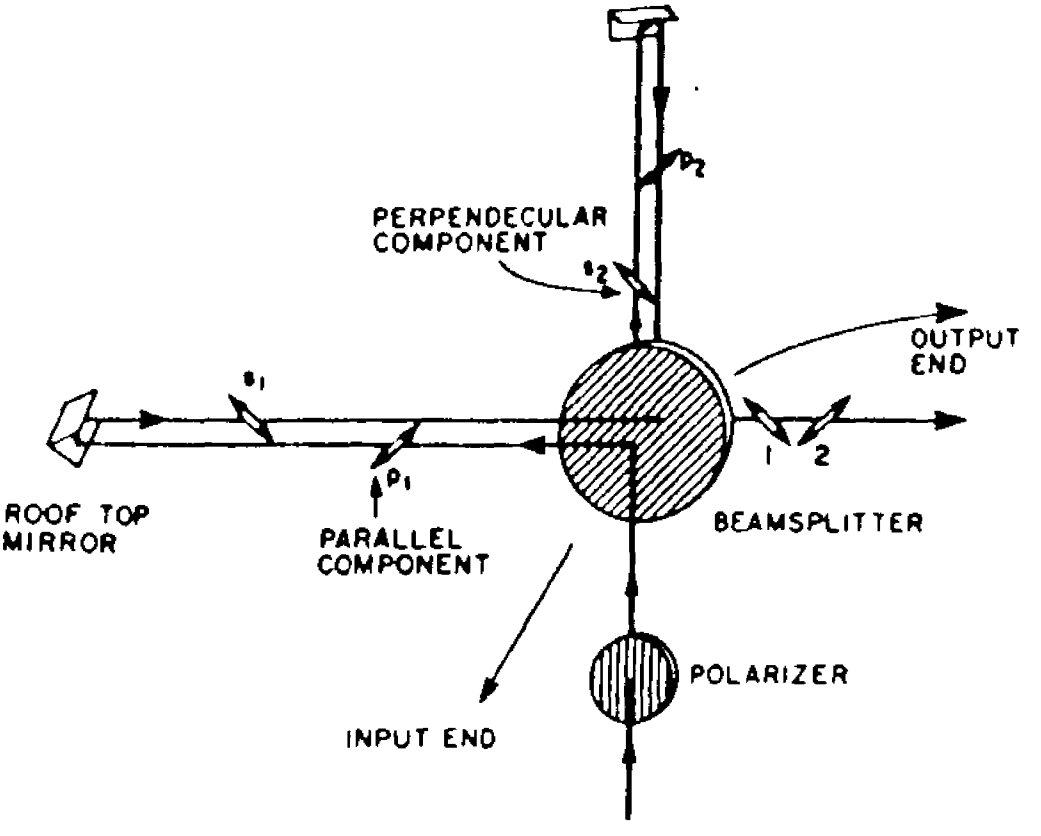

a) Polarizing Michelson Interferometer
(from ref.[55] by Polavarapu)

Figure 11. FT-VCD-PMI

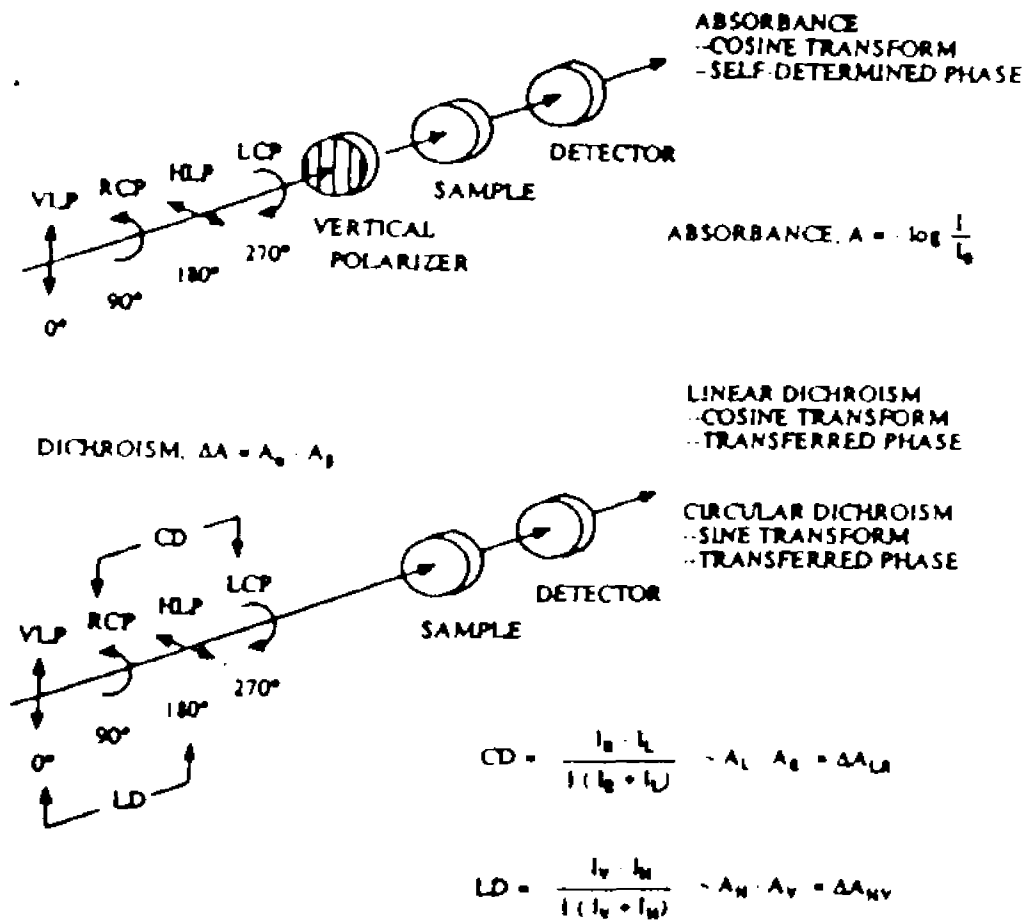

b) Diagram for Measuring Absorbance, Circular Dichroism, and Linear Dichroism (from ref.[56] by Nafie *et al*)

can be decomposed into two linearly polarized waves of equal amplitudes. One of the waves with its electric potential vector, polarized parallel to the grid direction of the beam splitter(B), will pass the beam splitter and propagates toward the fixed mirror (M_f). The other wave polarized perpendicular to the grid direction of the beam splitter will be reflected by the beam splitter towards the movable mirror (M_m). The roof directions of the roof-top mirrors are also aligned 45° with respect to the axis of B. This arrangement of mirrors rotates the polarization of the incoming light wave by 90° as the mirrors reflect the beams back to the beam splitter. As the result of these polarization rotation, the beam coming from M_f is reflected by B and the one from M_m passes B. Both beams recombine (and interfere with each other) and exit the interferometer. The axis of A is set at 45° with respect to the axis of B, as well, and can be parallel or perpendicular to the axis of P.

The PMI produces polarization interference phase retardation, resulting in full cycles of polarization modulation of each wavelength at its own Fourier frequency. The polarization modulation cycle is vertical linear, right circular, horizontal linear, left circular, and back to vertical linear (or any cyclic permutation of these four states alternat-

ing between linear and circular polarization states) (*cf.* Figure 11b).

Intensity modulation on the PMI, like on a conventional FT-IR spectrophotometer, is achieved by simply inserting the analyzer, whose axis is parallel or perpendicular to the axis of the first polarizer, after the interferometer. Thus, a standard FT-IR absorption spectrum can be obtained, since

$$V'(\delta_x) = \int 0.5V_o(\bar{\nu})10^{-A(\bar{\nu})}[1 \pm \cos(4\pi\bar{\nu}\delta_x)]d\bar{\nu} \qquad (2.60)$$

where, $V(\delta_x)$ is the observed interferogram and δ_x is the path difference between the movable mirror and the fixed mirror. $V_o(\bar{\nu})$ is the source intensity entering the interferometer. $0.5V_o(\bar{\nu})10^{-A(\bar{\nu})}$ is the IR spectrum, $V(\bar{\nu})$, which can be obtained by a cosine Fourier transform of $V'(\delta_x)$. The 0.5 accounts for the P cutting in half the light intensity from the light source. The plus or minus sign is determined by the orientation of the analyzer with respect to that of the first polarizer, parallel corresponding to positive (+) and perpendicular to negative (-).

Removal of the analyzer allows the circular dichroism measurement of an optically active sample

to be carried out through a sine Fourier transform of the complex interferogram:

$$V''(\delta_x) = \int 0.5V_o(\bar{\nu})10^{-A(\bar{\nu})}[1 + 1.15\Delta A(\bar{\nu})\sin(4\pi\bar{\nu}\delta_x)]d\bar{\nu} \qquad (2.61)$$

where

$$10^{-A(\bar{\nu})} = 0.5(\ 10^{-A_+(\bar{\nu})} + 10^{-A_-(\bar{\nu})}\ ) \qquad (2.62)$$

is the same quantity as the one defined above in Equation (2.60), and $\Delta A(\bar{\nu}) = A_-(\bar{\nu}) - A_+(\bar{\nu})$. The derivation of Equation (2.60) is similar to that described in the dispersive section. A reverse cosine Fourier transform of $V'(\delta_x)$ yields $0.5V_o(\bar{\nu})10^{-A(\bar{\nu})}$. A sine Fourier transform of $V''(\delta_x)$ will yield $0.5V_o(\bar{\nu})10^{-A(\nu)}$ x $[1.15\ \Delta A(\bar{\nu})]$. The ratio of those two reverse Fourier transformations will lead to $\Delta A(\bar{\nu})$, the VCD spectrum.

$$\frac{\int V''(\delta_x)10^{-A(\nu)}\sin(4\pi\bar{\nu}\delta_x)\ d\bar{\nu}}{\int V'(\delta_x)10^{-A(\nu)}\cos(4\pi\bar{\nu}\delta_x)\ d\bar{\nu}} = 1.15\ \Delta A(\bar{\nu}) \qquad (2.63)$$

The elimination of the PEM also allows the omission of the lock-in amplifier. Therefore, the only limiting factor left for a wider frequency coverage is the detector saturation. To enlarge the range

while still preventing detector saturation, different optical filters of a variety of cutoff ranges can be used.

The first reported FT-VCD-PMI spectrum by Nafie *et al.*[56] on (-)-α-pinene showed excellent agreement with FT-VCD-PEM result on the same sample. The signal-to-noise ratio was very good. However, it took nineteen hours to produce the spectrum, comparing to five and half hours needed in FT-VCD-PEM[21] and six hours or shorter for a dispersive VCD. The enantiomeric spectrum was still needed for baseline correction. This instrument was constructed to cover only the region between 800 cm^{-1} (HgCdTe detector cutoff) and 1600 cm^{-1} (filter cutoff to prevent detector saturation). By contrast, the prototype FT-VCD-PMI in Polavarapu's paper covers the range from 10 to 1000 cm^{-1}, although a result from any real sample has not yet been reported. As expected, the elimination of the PEM allows the FT-VCD-PMI to cover a wider range (up to 1000 cm^{-1}). However, further exploration and experimentation are needed to optimize the FT-VCD-PMI experiment.

Chapter Three

Dispersive VCD Instruments at Hunter College

This chapter concentrates on a detailed discussion of the design of the two dispersive vibrational circular dichrographs built at Hunter College. Their performance will be presented in the next chapter.

In the late 1970s and early 1980s the dispersive VCD system improved significantly with the arrival of the highly sensitive HgCdTe detectors and the commercial photoelastic modulators. The dispersive instrument constructed by Keiderling *et al.* produced some excellent spectra in the mid-infrared region[57]. All these, combined with the operational difficulties FT-VCD-PEM has been experiencing, have rekindled interest in dispersive VCD.

3.1 The First Dispersive VCD Instrument (VCD-I)[32]

VCD-I is designed primarily to study the conformation of small peptides in aqueous solution via

the amide III vibration. The assignments of that vibration has been studied carefully by isotopic substitutions[58]. Hence, the design objective is an instrument optimized around 1200 cm^{-1}, and also covering a reasonably wide range, 900 - 1800 cm^{-1}, which includes the amide III, II and I bands, with high sensitivity.

3.1.1 General optical considerations

The ultimate goal in designing this VCD instrument, as for any other spectrophotometer, was to get the greatest light throughput at the best resolution. These two mutually exclusive requirements (only for a dispersive instrument) must be balanced in the design, which attempts to optimize the system by carefully matching the size of light source, the optical aperture, the slit width (bandpass), and the grating groove density.

In this case, the throughput was of special importance because water, the solvent normally used, absorbs strongly in the region. For a cell with CaF_2 window and a 15 μm spacer, H_2O transmits only 25% of the light on average between 1200 and 1500 cm^{-1}, while D_2O transmits an average of about 70% between 1300 and 1800 cm^{-1}.

The spectral resolution requirement was somewhat relaxed; the design goal was to make it better than 15 cm^{-1} since in aqueous solution the half width at half height of most infrared peaks from samples of our interest in this region is greater than 15 cm^{-1}.

Several factors contribute to achieving that goal. First, a high brightness source is desired. Based on the principles of black-body radiation, the higher the color temperature, the higher the infrared output. Second, low F-number optics, including the monochromator, were selected, giving a large acceptance angle. Furthermore, for two mirrors (or lenses) of the same diameter, the one with lower F-number produces a shorter total optical path. The selection of the source and optics has to be done in a coordinated fashion. The low F-number and the size of optics require a small image size, consequently, a small source size. The small image size also allows a narrow slit width, therefore, maintaining high enough resolution (8 - 15 cm^{-1}). Moreover, the small image size is easily reduced and focused onto the tiny area of a high sensitivity detector, which is needed for the VCD measurement. The small active area of the semiconductor detector is a trade-off for its high sensitivity since the sensitivity, expressed by D^*, is inversely proportional to square root of the

area[41].

Third, whenever possible in the process of selecting the optics, using a concave mirror with metal coating on its front surface instead of a convex lens would result in higher throughput due to the fact that the light loss to the reflection of a mirror is generally much smaller than the transmission loss to a lens in the infrared. For example, the reflection loss is less than 1% on a gold-coated surfaces[59], whereas the light loss on a lens is generally greater. On an interface at which the light ray passes from one medium to another at normal incidence, the light intensity loss is, according to[2]:

$$\text{Intensity loss} = \frac{(n_2 - n_1)^2}{(n_2 + n_1)^2} \qquad (3.1)$$

Here, n_1 and n_2 are the refractive indices of the two interfacing media.

The light intensity loss would be 2.2% between air (n_1=1) and CaF_2 (n_2 = 1.35) on each surface. There are two surfaces on each lens (or window), so the total loss of light on a CaF_2 lens is 4.4%. BaF_2 has a similar reflective index, n = 1.4, and so it would

result a similar light loss. The loss from a ZnSe (n = 2.4) lens would be much greater, 34% all together, from the two surfaces of the lens. In addition, the use of mirrors avoids chromatic aberrations associated with using a lens, but introduces spherical aberration. Further thought has also been given to minimize the number of mirrors to reduce the reflective loss along the path.

Fourth, all optical components have been specially treated to give maximum light throughput. All reflecting surfaces, including those inside the monochromator (mirrors and grating), were gold-coated. The reflectivity of a gold-coated surface in the mid-IR region is 99% compared to 90% for an aluminum-MgF_2-coated surface. This is actually not a small matter since reflection losses can add up quickly. For example, if there are eight Al mirrors in a system, the loss would be $(1-0.90^8)=57\%$. In contrast, the loss would only be $(1 - 0.99^8) = 7.7\%$ if they are gold coated. Moreover, gold-coating also offers a long term chemical stability.

For the necessary transmission optics, especially the PEM crystal, it must be treated by a method called anti-reflection (AR) coating. The light loss at the surfaces between air (n = 1.0) and a crystal with a larger refractive index (*e.g.*, 2.4 for

ZnSe in the PEM) can be reduced drastically (to less than 0.1%) by gradually and sequentially coating the surface with certain substrates whose refractive indices are between 2.4 and 1.0. The difference in refractive indices between any two adjacent layers of the substrate is very small (less than 0.1).

3.1.2. Optics of VCD-I

Following the guideline of the above general considerations, VCD-I was conceived. Figure 12 is the optical layout of VCD-I and Table I is the specifications of elements used.

The infrared source is a high temperature Nernst glower (ARTCOR, Inc., Model 242-103-5) of small size (1.8 mm diameter x 12 mm useful length), radiating at a color temperature of 2200-2400 K. The glower is heated by 1.6 amp. AC at 60 Volts, and consumes about 100 watts power. Its lifetime is about 2000 hours.

A previously constructed dispersive VCD, for the mid-infrared region[57], employed a large carbon rod source operating at 330 amp. and 8.5 V, which produces a similar color temperature as Nernst glower. Its size, 8 mm x 100 mm, caused a serious

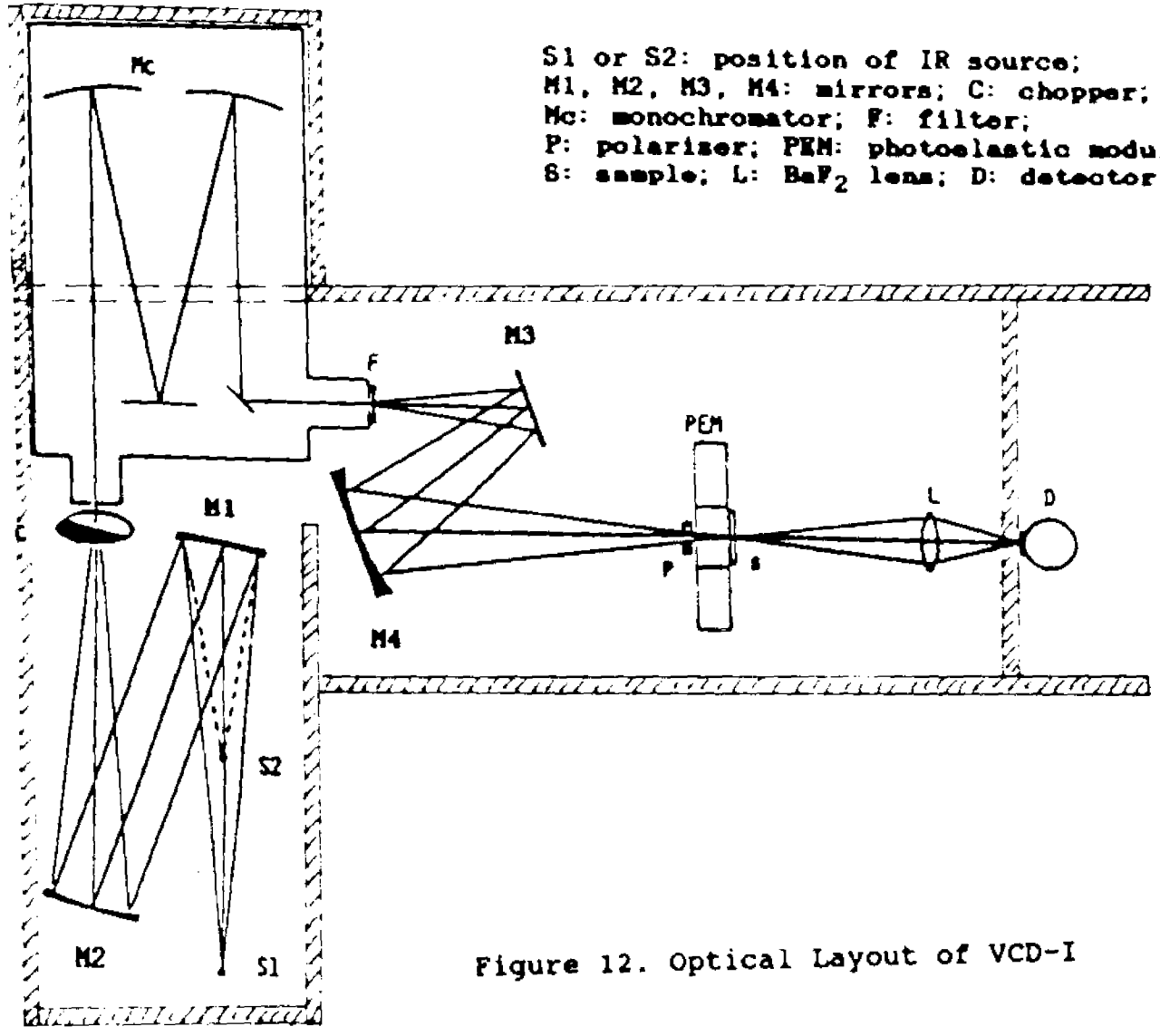

Figure 12. Optical Layout of VCD-I

Table I

VCD-I Component Specifications

Component	Specification
Nernst Glower Source	Brightness Temperature 2200 K 1.8 mm x 12.7 mm
Chopper	Mechanically modulates at 79.5 Hz
Monochromator	Czerny-Turner F/4.4, f = 320 mm ruled grating, 120 g/mm gold coated mirrors and grating
Polarizer	Gold wire grid on AgBr substrate
Photoelastic Modulator	ZnSe, octagonal, 12 mm thick 45 mm between opposing edges anti-reflection coated, modulates at 31.2 kHz
HgCdTe Detector	$D^* = 3.556 \times 10^{10}$ cm $Hz^{0.5} W^{-1}$ active area: 1.01×5.08 mm^2 range: 800 - 1800 cm^{-1}

problem. A long focal length monochromator (HR1000 by Jobin-Yvon) had to be used to preserve good enough resolution since the slit width (image size) was so large. Therefore, the F-number of the collection optics was relatively large (F/6.8). Furthermore, it was hard to reduce the image size so it would fit the detector size (2 mm x 10 mm). There are also some operational difficulties associated with the carbon rod. It must operate in an oxygen-free atmosphere in order not to burn. As a result, it needs an insulated and water-cooled housing with a window (CaF_2), as well as continuous nitrogen purging. The expected life time of each carbon rod is only 50-100 hours.

Since the Nernst glower and carbon rod have almost exactly the same color temperature that determines the optical power output per unit area, it is to the advantage of the Nernst glower to have a smaller image size. As a result, the design of VCD-I utilizes a lower F-number (F/4 or F/2), a shorter total path and a smaller detector than the previous VCD design. A shorter total pathlength makes the physical size of the instrument small and reduces the interference from the absorption by water vapor in the air. The smaller the active area of a semiconductor infrared detector the more sensitive it is (see 3.1.1). All above factors compensate the light reduc-

tion because of our smaller source size to a level that total light throughput of these two system are about same. In addition, the Nernst glower source does not need a water-cooled housing, nitrogen purging and an isolated chamber with a window. It also has a longer lifetime (greater than 20 times) and lower power consumption (only 1/30) than the carbon rod.

The mirrors, M_1 - M_4 (Ealing Electro-Optics, Inc.), are all gold-coated. The light collection mirror, M_1, can be set at either F/4 for one-to-one imaging, or F/2 for one-to-two imaging. When running in the amide I region, the light is focused one-to-one on the entrance slit of the monochromator in the F/4 setting, which matches the F-number of the monochromator. The entrance and exit silts are 10 mm high and their widths are set at 2.0 mm. M_1 and M_2 are 89 mm (3.5 inches) in diameter and 300 mm in focal length. For the measurements in the amide III region or lower, the F/2 collection is set to gain more light as the resolution of the monochromator is better in this region (see Table II), thus allowing the slit of the monochromator to be opened wider (up to 4.0 mm). M_1 is changed to a mirror of 102 mm (4 in.) diameter and 150 mm focal length. M_1 collects

the light from the source, and reflects a collimated beam. M_2 then focuses the beam onto the monochromator entrance slit with an F-number of 4.4.

An optical chopper (Laser Precision Corp., model CTX-534), operating at 79.5 Hz, is placed before the entrance slit of a digitally controlled monochromator (Instruments, SA, HR320). The chopper is referenced externally by a quartz frequency oscillator to reduce frequency jitter. The monochromator has a ruled grating (groove density 120/mm) and F-number of 4.4, and provides satisfactory optical resolution at a reasonable slit width(*cf.* Table II). The bandpass is 5.5 to 14.2 cm^{-1} at slit width of 2.0 mm between 1200 and 1800 cm^{-1}, and 3.1 to 11.0 cm^{-1} at slit width of 4.0 mm between 800 and 1200 cm^{-1}.

From Table II, one can see that, while satisfying the resolution criteria, the slit width can be set at 2.0 mm for the region above 1400 cm^{-1} (*i.e.*, the amide I and II regions), which requires the light collection optics be arranged F/4, and at 4.0 mm for the region below 1400 cm^{-1} (*i.e.*, the amide III region), which requires a F/2 setting to fill the slit for more light throughput.

Upon leaving the monochromator, the light passes either a 5-10 μm or an 8-15 μm bandpass filter

Table II

VCD-I Resolution Summary[a,b]

(HR320 Monochromator)

Wave-length [μm]	wave-number [cm^{-1}]	linear dispersion [nm/mm]	Bandpass at slit width 2 mm	3 mm	4 mm
				[cm^{-1}]	
5.556	1800	22.5	14.2		
6.250	1600	22.1	10.9		
7.143	1400	21.5	8.0	12.0	
8.333	1200	19.1	5.5	7.6	11.0
10.00	1000	16.8		5.0	6.7
12.50	800	12.2		2.3	3.1

a. calculated by equations given in Ref.[60]
b. included angle is 24°.

(Oriel Corp.), cutting off the higher order diffraction. M_3, a flat mirror of 50.9 mm (2 inches) diameter, changes the direction of light propagation, providing room for succeeding optics. M_4, a concave mirror of 76 mm (3 in.) in diameter and 150 mm in focal length, focuses the light beam through a polarizer and the photoelastic modulator (PEM) onto the sample, which is mounted directly behind the PEM.

In front of the PEM is a gold-wire grid polarizer (Perkin-Elmer Corp., 186-0243) on a silver bromide (AgBr) disk. The polarizer is aligned with its transmitting axis horizontal, because an experiment indicates this component is more intense than the vertical component.

The photoelastic modulator (Hinds International, Inc., model PEM-80, system III/ZS) has a clear aperture of 42 mm in diameter. Its heart is a broadband antireflection-coated ZnSe crystal (transmission > 90% between 12 and 5 μm). The stress axis of the PEM is 45° with respect to the horizontal, the direction of the linear polarizer. It modulates at 31.2 KHz, at which frequency it alternately produces left and right circularly polarized light. The modulation frequency is really the resonance frequency of the crystal, whose hardness and physical size determine

this frequency. After the PEM, a sample cell holder is mounted on the PEM housing. The polarizer, PEM and sample occupy a length of only six centimeters along the optical path. Because the sample is positioned at a focal point, the image size is small (1.8 mm x 10 mm for F/4 collection, 3.6 mm x 10 mm for F/2 collection), so small cells (15 mm in diameter) may be used.

A single BaF_2 lens, 50 mm in diameter and 50 mm in focal length, is placed after the sample to focus the light beam onto the detector. The lens was chosen to avoid the polarization bias associated with using a mirror. BaF_2 cuts off below 850 cm^{-1}, which is therefore the lower frequency limit of the VCD-I. To go to even lower wavenumber, one could change the lens to AR-coated ZnSe, for example; and the next barrier is the cutoff at about 600 cm^{-1} of ZnSe crystal inside the PEM . Depending on the collection aperture, the position of the lens is adjusted so that the image at the sample is demagnified to the approximate size of the detector element.

A high sensitivity detector (Infrared Associates, Inc., Model HCT-80) was selected. Its active element (1.0 mm x 5 mm) is a photoconductive mercury cadmium teluride (MCT or HgCdTe) with a peak D^* about 3.5×10^{10} $cmHz^{0.5}W^{-1}$ at 1000 cm^{-1}. MCT, operating

under liquid nitrogen cooling, is the most sensitive detector available in the region of interest. All optical components are enclosed in a plexiglass housing to permit dry air purging.

3.1.3 Electronics of VCD-I

Figure 13 is a schematic illustration of the VCD electronics. The signal from the detector is first amplified by a preamplifier (Infrared Associates), and subsequently is split into two paths for processing $V_{DC}(\bar{\nu})$ and $V_{AC}(\bar{\nu})$. One of them leads to a digital lock-in amplifier (Ludl Electronics Products, Ltd.), demodulating at 79.5 Hz to extract the $V_{DC}(\bar{\nu})$. This amplifier has a computer controlled, variable input gain of 1, 10 or 100, followed by a voltage-to-frequency converter and a fast, dual channel pulse counter. This amplifier is mounted in a rack, which also houses the monochromator motor drive, the PEM modulation controller, the detector power supply, and a communication interface (Intel PPI 8748). $V_{DC}(\bar{\nu})$ is directly read from the digital lock-in amplifier by a computer via a 24-bit parallel bus. Through the same channel, the computer also commands the monochromator wavelength position and the PEM modulation (α_o).

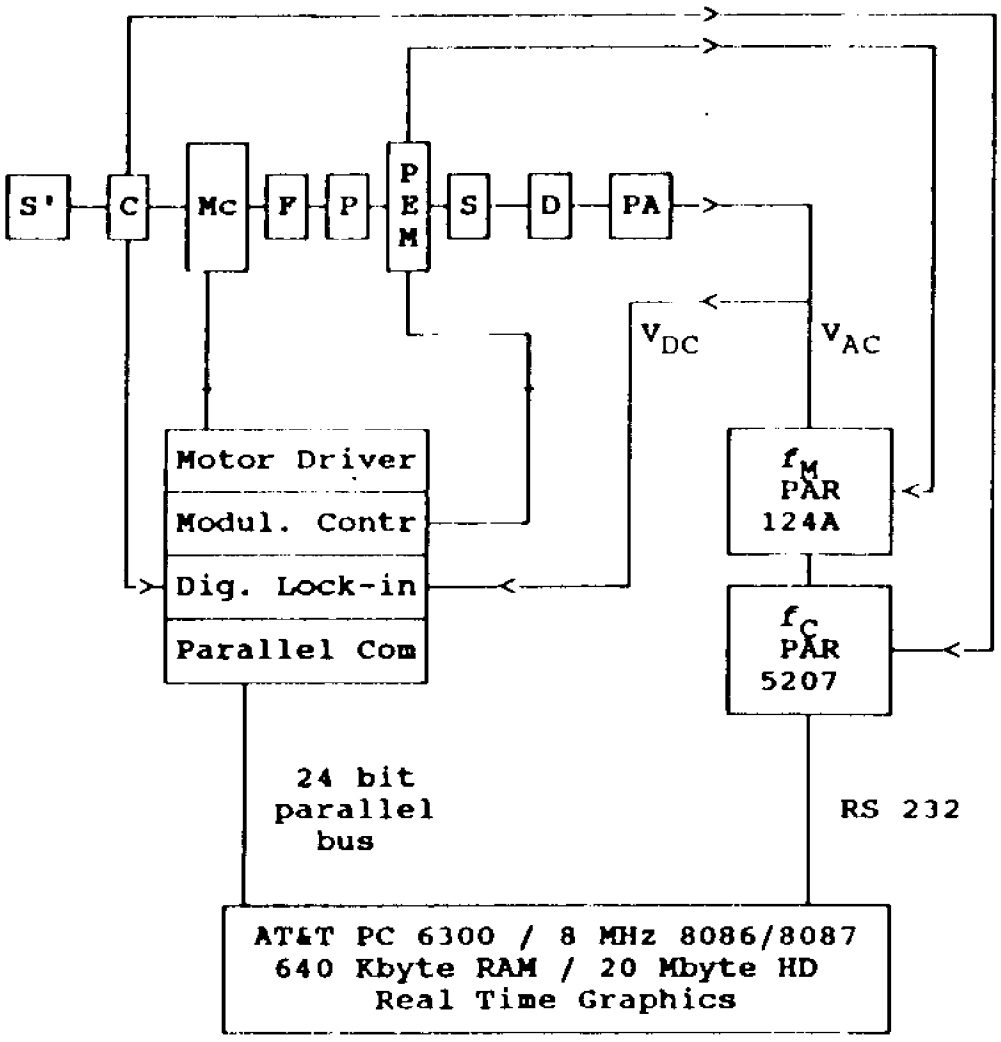

M: monochromator; PA: preamplifier
PAR 124A or PAR 5207: Lock-in Amplifier.

Figure 13. Electronic Scheme of VCD-I

(*cf.* text)

The typical detector output without sample is about one volt. With an H_2O sample in a CaF_2 cell and 15 μm spacer, the detector reads about 0.3 V (solvent transmission). For a sample with an absorbance 0.5 at a particular wavenumber, the detector outputs about 0.095 V, the $V_{DC}(\bar{\nu})$ for that particular sample. Assuming $\Delta A(\bar{\nu})$ is 10^{-4}, $V_{AC}(\bar{\nu})$ would be in the neighborhood of 1.9×10^{-5} V.

The above estimate of $V_{AC}(\bar{\nu})$ demonstrates the necessity of using a phase-sensitive detector, *i.e.*, a lock-in amplifier, to extract the small signal out of a noise level that is much larger (say, 1% of the transmittance, $V_{DC}(\bar{\nu})$, approximately in the millivolt range). The $V_{AC}(\bar{\nu})$ is processed by demodulating the detector output at the PEM frequency, 31.2 kHz, by a lock-in amplifier (Princeton Applied Research, model 124A) operating in band pass mode and minimum time constant (< 1 ms). The gain of this lock-in amplifier, defined by the ratio of full-scale dc output (10 volt) to the input sensitivity, is usually between 500 and 1000, *i.e.*, the input sensitivity range is set between 10 and 20 mV. At these levels, no signal overload occurs. Since the operating conditions are set such that the sample IR absorbance is between 0.5 to 1.0, which translates to a $V_{DC}(\bar{\nu})$ variation of less than one order of magnitude, the fixed sensi-

tivity setting of the PAR 124A is adequate.

The output of the PAR 124A is a 79.5 Hz signal (*cf.* Figure 14) since the VCD signal is only present during the "on" cycle of the chopper. Consequently, it is further demodulated at the chopper frequency, 79.5 Hz, by a second more sophisticated lock-in amplifier (PAR 5207), all functions of which can be monitored and serviced by an external computer. This is of great significance because $V_{AC}(\bar{\nu})$ can vary by several orders of magnitude. A fixed sensitivity accommodating the maximum signal would have to sacrifice accuracy of measurement for signals orders of magnitude smaller. The dynamic range of the measurement would be restricted. The PAR 5207 allows the sensitivity setting to be adjusted over the entire range from 100 nV to 5 V, so that the output signal preserves 3.5 digit accuracy. As a result, digital normalization becomes possible (*vide infra*). The input signal to the PAR 5207 is compared with the present sensitivity setting, which has steps of 1, 2, 5 and 10. If the signal is smaller than 40%, or larger than 110% the sensitivity setting, the setting is adjusted accordingly. Whenever the PAR 5207 switches its sensitivity setting, the computer pauses the scanning, and delays for a period equal to six times the

PAR 5207 time constant after the switching, then resumes the scan. The delay is needed for the PAR 5207 to stabilize so the output data is valid. However, because too frequent switching and delay can result in a very slow scan speed, a sensitivity limit is defined in the computer program to avoid the unnecessary switching of the sensitivity setting when the signal is very small, such as at the zero crossing in a VCD spectrum or when there is no signal, for example, outside an absorption band. Therefore, the PAR 5207 is programmed not to switch its sensitivity setting for the instrumental noise. The output of the PAR 5207, a digital signal corresponding to $V_{AC}(\bar{\nu})$, is sent directly to the computer via a standard RS232 serial communication port at 1200 baud.

Figure 14 shows the wave forms at various points, which illustrates the evolution of the VCD signal and helps to illustrate the design of the instrument.

The figures presented are at only one spectral point (a certain $\bar{\nu}$) during a given data acquisition time, *e.g.*, one second. The abscissae are time, and the ordinates are signals expressed either in light intensity, I, or a voltage.

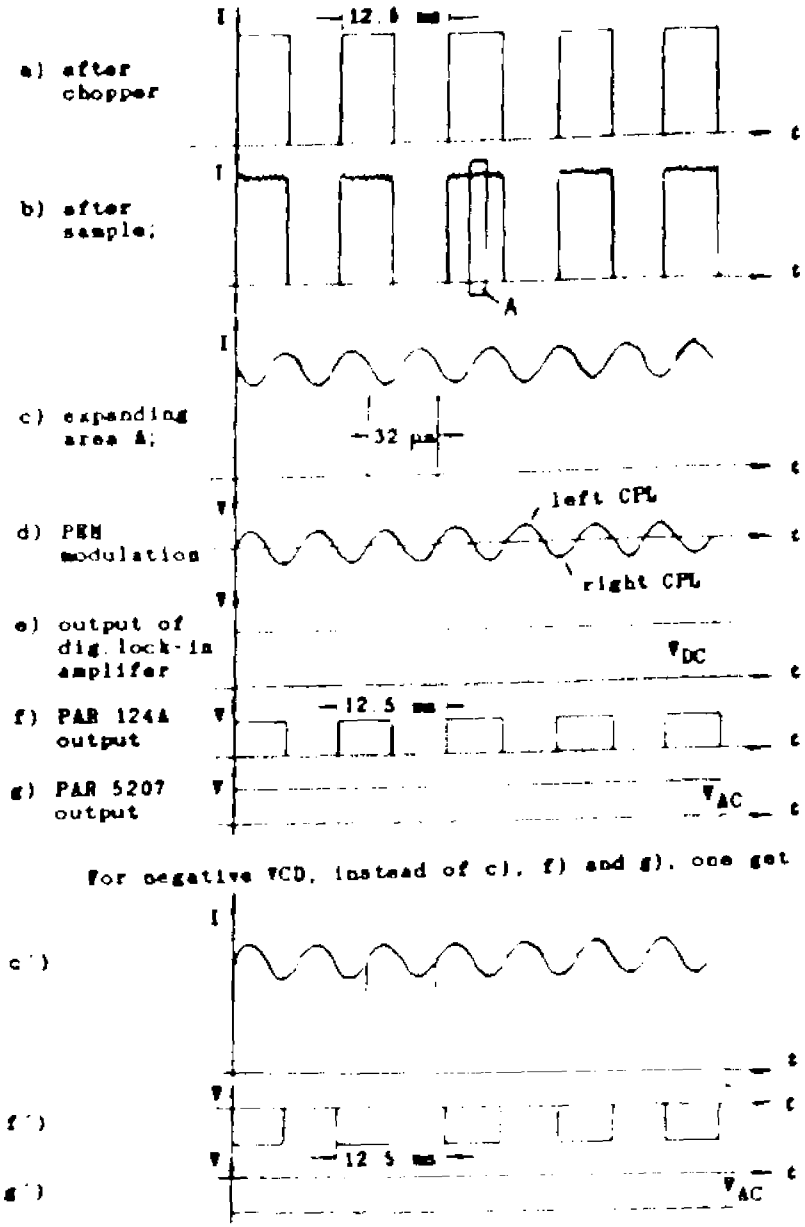

Figure 14. Wave Forms of VCD Signal

The chopper produces a square-wave (a), whose pattern is modified after the sample (b), and on top of the average absorption there is the differential absorption (c). The difference is synchronized with the PEM modulation frequency (d) (the graph shown results a positive $V_{AC}(\bar{\nu})$). After filtering out the high frequency component ($V_{AC}(\bar{\nu})$) of (b), the digital lock-in amplifier takes the average difference between "on" and "off" cycles of the square-wave within a given data acquisition time and outputs $V_{DC}(\bar{\nu})$ (e). By contrast, the PAR 124A first filters out $V_{DC}(\bar{\nu})$, and outputs the averaged difference in transmission between left and right circularly polarized light, $T_L(\bar{\nu})-T_R(\bar{\nu})$ (f) with an 180° phase shift. This is necessary since the definition of $\Delta A(\bar{\nu})$ is $A_L(\bar{\nu})-A_R(\bar{\nu})$, and the higher a transmission, the smaller is the corresponding absorption. Subsequently the PAR 5207 demodulates at 79.5 Hz, yielding $V_{AC}(\bar{\nu})$ (g). A negative $V_{AC}(\bar{\nu})$ would have an 180° phase shift in each $V_{AC}(\bar{\nu})$ graph, demonstrated by (c'), (f'), and (g').

An important difference between Hunter College's VCD-I system and others is the use of the digital normalization. As stated in the previous chapter, $\Delta A(\bar{\nu})$ is proportional to the ratio of $V_{AC}(\bar{\nu})/V_{DC}(\bar{\nu})$. VCD-I simultaneously measures $V_{AC}(\bar{\nu})$ and

$V_{DC}(\bar{\nu})$, calculates $\Delta A(\bar{\nu})$, and displays all of them in real time on the computer screen. The corresponding VCD spectrum ($\Delta A(\bar{\nu})$ versus wavenumber) is displayed as well.

All the previously constructed dispersive VCD instruments used an analog circuit for the normalization. Normalization was done via a so-called autogain circuit, whose principle is similar to what the commercial UV-visible CD has been using. The circuit monitors the transmission as the monochromator scans, and maintains $V_{DC}(\bar{\nu})$ (the input to the first lock-in amplifier) constant. As a result, the $\Delta A(\bar{\nu})$ is then directly proportional to the $V_{AC}(\bar{\nu})$. The way to maintain the $V_{DC}(\bar{\nu})$ constant in the commercial CD instrument is by changing the gain of its detector, a photomultiplier tube, by changing the voltage applied to it. In the infrared, however, the semiconductor detector offers no such luxury. Therefore, another method was sought. The most advanced method employs a special lock-in amplifier, demodulating at f_C, in the $V_{AC}(\bar{\nu})$ path between the preamplifier of the detector and the lock-in amplifier tuned to f_M. The gain of this special lock-in amplifier is controlled by a feedback circuit so its output is kept constant. The elimination of such an autogain circuit in our system

appears to have improved the spectral signal-to-noise ratio.

The PEM is synchronized to the wavelength of the monochromator in order to achieve the quarter-wave modulation at every wavelength during a scan. The data are, therefore, directly in $\Delta A(\bar{\nu})$ units. This and the excellent reproducibility of VCD-I demonstrate that the instrument need not be frequently calibrated, as was necessary in the other previously constructed dispersive and FT-VCD-PEM spectrometers, which all utilized a fixed retardation. The synchronization is done by issuing a voltage to the PEM modulation control unit from a digital-to-analog converter, which receives a signal from the computer that is proportional to the monochromator wavelength. This voltage is recalculated at each wavenumber as the monochromator steps in a linear wavenumber increments, typically one cm^{-1}.

controlling all electronics, including the monochromator stepping motor, the synchronized PEM modulation level and two of the three lock-in amplifiers, is performed by an AT&T personal computer, Model 6300, incorporating 8 MHz, 16-bit 8086/8087 processor, 640 Kbyte RAM, and a 20 Mbyte hard disk. The software, written by Professor Max Diem and Mr. Arthur Barlow, is completely menu driven and controls

the data acquisition and the storage of IR absorption and VCD spectra. An infrared transmission spectrum is collected during a "prescan" (scanning forward without a sample, then scanning backward with the sample), and the infrared absorption spectrum is computed. This prescan is also useful in determining suitable experimental conditions, such as the sample concentration and the cell pathlength.

The data acquisition time is typically one second per point, and is chosen to be the same as the response time on the lock-in amplifier, the PAR 5207. Both are input from a menu display before any scan. The time constant can be changed to 0.3, 3 or 10 second. The timing in the $V_{DC}(\tilde{\nu})$ data acquisition is derived from a timer within the digital lock-in amplifier. At each data point, the timer starts, and the $V_{DC}(\tilde{\nu})$ signal counts are acquired until the preselected time expires. During the preselected time, the chopper is "on" for 79.5 times. The $V_{DC}(\tilde{\nu})$ signal is actually the average of the difference between the "on" and "off" cycles of the chopper within that time frame. Subsequently, the $V_{DC}(\tilde{\nu})$ is normalized with respect to the input gain and the time constant, and converted to a voltage. The analog time constant of the PAR 5207 in the $V_{AC}(\tilde{\nu})$ path is

also set the same as the data acquisition time by the computer. The output of the PAR 5207, which has four significant figures and already normalized with respect to the gain of the PAR 5207, is then normalized with respect to the gain of the first lock-in amplifier (PAR 124A), as well. Subsequently, $\Delta A(\bar{\nu})$ is calculated and displayed on the screen. Afterward, the wavelength position of the next data point is computed from the linear wavenumber increment (one cm^{-1}), the monochromator is scanned to the new position, and the PEM control voltage is calculated and adjusted to this new wavelength. The software is written in Magic/L (Loki Engineering, Inc.), a language combining the concept of FORTH with the structure of PASCAL or "C" compilers.

The performance of VCD-I will be the subject of the next chapter.

3.2 The Second Dispersive VCD (VCD-II)[61]

It was apparent after VCD-I was operational that the VCD spectra in the amide I region of some small peptides in the aqueous solution were very interesting, and were easily interpreted by the coupled oscillator model. Furthermore, other projects involving another category of biologically significant molecules, nucleic acids, also exhibited results that could be nicely interpreted and led to conformational understanding of the molecules. The probe for the DNA is the carbonyl (C=O) stretching on the bases of the nucleic acids, also in the region of 1550-1750 cm^{-1}. However, the noise level of the spectra obtained on VCD-I was consistently higher than what we would have liked. The reason was mostly the lowered responsivity of the detector, which at 1670 cm^{-1} drops to 50 percent of the maximum. More than 40 scans are needed in order to get a reasonable signal-to-noise ratio. We concluded that a new instrument dedicated to the region of 1550 - 1750 cm^{-1} with a superior S/N was needed. That was the design objective for the VCD-II.

The optical and electronic design of VCD-II are, understandably, very similar to those of VCD-I, therefore, only the parts of major difference will be

discussed.

3.2.1 Optics of VCD-II

Figure 15 and Table III present the optical part of VCD-II.

The mirrors, M_1 - M_3, (Ealing Electro-Optics, Inc.) are all gold-coated. The collection mirror (M_1, d = 101.8 mm, *i.e.* 4 in., and f = 200 mm) gathers light at F/3.0 from the source, the same model Nernst glower used in VCD-I, and focuses the image at the entrance slit of the monochromator, while matching its F-number (F/5.7). An optical chopper (same model as the one in VCD-I) operates at 45 Hz. The monochromator (Instrument, SA, HR640) has a ruled grating (groove density 150g/mm) and scans faster than the HR320 used in VCD-I. The mirrors and the grating inside the monochromator were, unfortunately, not gold coated because the monochromator is on loan from the manufacturer. They are, however, standard aluminum coated.

Table IV demonstrates clearly that setting the slit width at 3.0 mm satisfies the resolution requirement very well for the region between 1500 to 1800 cm^{-1}. After the monochromator is a 5-10 μm band-

S´: IR source; M1, M2, M3: mirrors; C: chopper;
F: filter; P: polarizer; PEM: photoelastic modulator;
S: sample; L: CaF_2 lens; D: MCT detector.

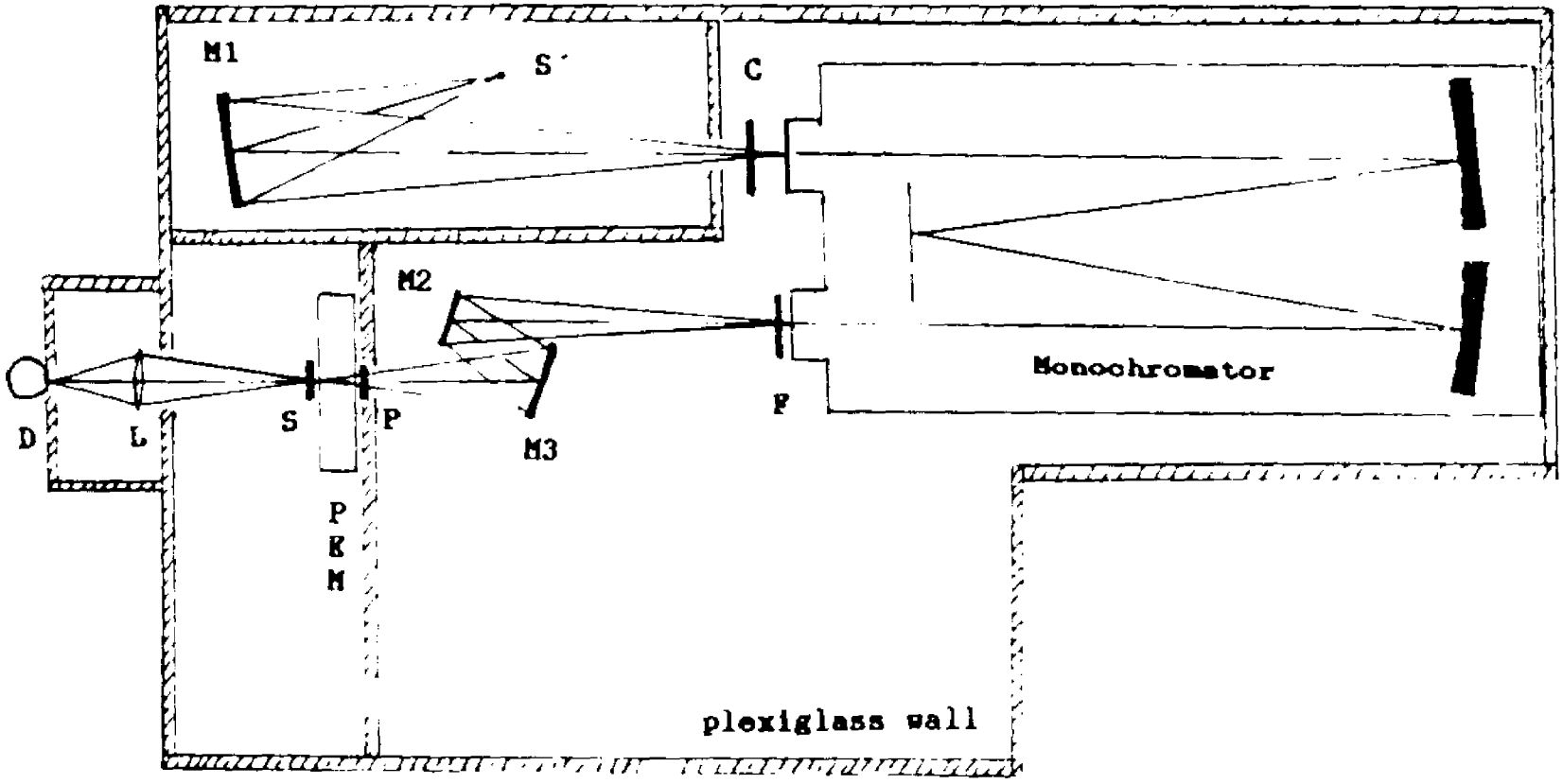

Figure 15. Optical Layout of VCD-II

Table III

VCD-II Components Specifications

Component	Specification
Nernst Glower Source	ZrO_2 with rare earth metal Brightness Temperature 2200 K 1.8 mm x 12.7 mm
Chopper	Modulates at 45 Hz
Monochromator	Czerny-Turner configuration F/5.7, f = 640 mm ruled grating, 150 g/mm
Polarizer	wire grid on CaF_2 substrate
Photoelastic Modulator	CaF_2 octagonal crystal 35.5 mm clear aperture modulates at 56.7 kHz
HgCdTe Detector (dual element)	$D^* = 8.9.68 \times 10^{10}$ cmHz$^{0.5}$W^{-1} area: 1.01 x 2.03 mm^2 range: 1575 - 3225 cm^{-1}

Table IV

VCD-II Resolution Summary (HR640 Monochromator)

Wavelength [μm]	wavenumber [cm^{-1}]	linear dispersion [nm/mm]	Bandpass at slit width 2 mm [cm^{-1}]	3 mm [cm^{-1}]	4 mm [cm^{-1}]
5.556	1800	22.5	14.2		
5.000	2000	8.902	7.11	10.66	14.22
5.263	1900	8.783	6.33	9.50	12.66
5.556	1800	8.644	5.59	8.39	11.19
5.882	1700	8.481	4.89	7.34	9.79
6.250	1600	8.286	4.24	6.36	8.47
6.667	1500	8.052	3.62	5.43	7.24

included angle is 18.221°

pass filter (Oriel Corp.), cutting off higher order diffraction above 2000 cm^{-1}. M_2 is a flat mirror of 50.9 mm (2 in.) in diameter. M_3, a concave mirror of d = 76.2 mm (3 in.) and f = 150 mm, refocuses the light beam through a polarizer and the photoelastic modulator onto the sample position.

The infrared grid polarizer (Cambridge Physical Sciences, model IGP 227-25) in front of the PEM is on a calcium fluoride (CaF_2) substrate disk and is aligned with its transmitting axis horizontal for the more intense component. The heart of photoelastic modulator (Hinds International, Inc., model PEM-80, system II/CF) is a CaF_2 crystal with a clear aperture of 35 mm. The stress axis of the PEM is also 45° with respect to the horizontal. It modulates at 57.6 kHz, higher than the one used in VCD-I because it uses a smaller crystal than VCD-I and CaF_2 is harder than ZnSe. Similar to VCD-I, a sample cell holder is mounted on the PEM housing. Once again, the polarizer, PEM and the sample occupy only a short stretch in the optical path. A CaF_2 lens, then, focus the light beam onto a HgCdTe detector.

The detector (Infrared Associates, Inc., Model HCT-80 6-7 Dual Element), specially made at our request, has an active element consisting of two 1.01 mm by 1.01 mm HgCdTe pieces, placed vertically to-

gether. Its peak D^* is about 8.969×10^{10} $cmHz^{0.5}W^{-1}$ at 1785 cm^{-1}. However, the responsivity drops drastically below 1600 cm^{-1}, which becomes the low-end cutoff of VCD-II. We were told that it is extremely hard to make a detector with the requested sensitivity in the region between 1400-1600 cm^{-1}. All optical components are enclosed in a plexiglass housing to permit dry air purging. In this instrument, the sample chamber is isolated from the rest of system and is purged separately. So, whenever changing the sample cell, the rest of the system is not exposed to the humid air outside, and the sample chamber can be purged dry in a relatively short time. As a result, scanning can proceed with little disturbance.

3.2.2 Electronics of VCD-II

The similar electronic scheme as VCD-I were set up with some minor changes. (*cf.* Figure 16)

The transmission ($V_{DC}(\bar{\nu})$) is processed by a home-built phase sensitive detector (designed around two circuit boards produced by Evans Associates, Lock-in Module, model 4110), demodulating at 45 Hz. The amplifier can be set manually at a variable gain of 1, 10, and 100, and an analog time constant of

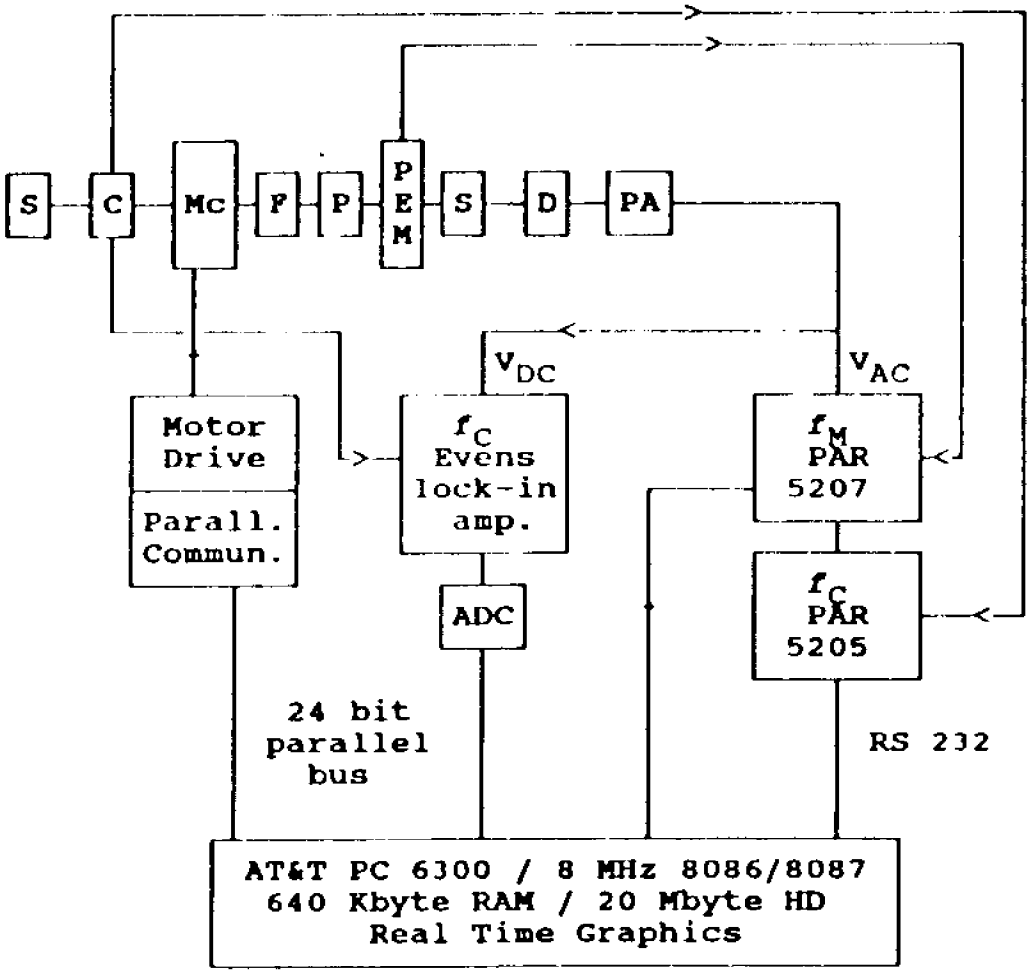

Figure 16. Electronic Scheme of VCD-II
(*cf.* text)

0.3, 1 and 3 second. Before any scan, a computer menu requests the selected time constant, which should be set the same as the data acquisition time. The output of this lock-in amplifier is, then, sent to an analog- to-digital converter (ADC) inside the computer. Subsequently, $V_{DC}(\bar{\nu})$ is normalized with respect to the gain and time constant.

The typical detector output for the instrument (*i.e.*, air transmittance) is about 2.5 V, which leaves some room to maneuver the sample concentration or/and the cell path length. With a CaF_2 cell containing D_2O and 15 μm spacer, the detector reads about 1.75 V (solvent transmission).

For a sample with an absorbance of 1, the detector outputs about 0.175 V, the $V_{DC}(\bar{\nu})$. Assuming $\Delta A(\bar{\nu})$ is 10^{-4}, V_{AC} would be in the neighborhood of 3.5×10^{-5} V.

In the $V_{AC}(\bar{\nu})$ detection chain, the first lock-in amplifier (PAR 5207) demodulates at the PEM frequency, 57.6 kHz, operating in the band pass mode at the minimum time constant of 1 ms. Its sensitivity is set by the computer (write-only) at beginning of each scan via a serial port (com2), normally at 10 mV. So the gain is 1000. Its output is subsequently fed into the second lock-in amplifier (PAR 5205), demodulating at the chopper frequency, 45 Hz. Like the PAR 5207 in

VCD-I, all functions of this PAR 5205 are monitored and serviced by a computer so that the sensitivity setting is adjusted to preserve the output signal with four significant digits. The principle of sensitivity adjustment is the same as described in the previous section, and need not to be repeated here. The output of PAR 5205, a digital signal ($V_{AC}(\bar{\nu})$), is directly read by the computer via a standard RS 232 serial port (com1), and is subsequently normalized with respect to the gain of PAR 5207.

The PEM is fixedly set for the quarter-wave retardation at 6.00 μm. This is considered adequate because the small range VCD-II is covering, from 5.71 to 6.25 μm (1750-1600 cm^{-1}). Thus, any distortion on the circular polarized wave at the other wavelengths would be minor. The same model personal computer and the communication means used in VCD-I are on duty to control this system, as well. The similarly packaged software is written in MAGIC/L, the same language as in VCD-I.

$\Delta A(\bar{\nu})$ is computed, and displayed on the screen along side with wavenumber ($\bar{\nu}$), $V_{DC}(\bar{\nu})$ and $V_{AC}(\bar{\nu})$, as well as a spectrum, $\Delta A(\bar{\nu})$ vs. wavenumber. The computer then goes on to calculate the wavelength (in μm) of the next data point from a wavenumber linear

increment, and signals the stepping motor of the monochromator to scan to that new wavelength, hence, starts another cycle of measurement.

The most dramatic improvement of VCD-II over VCD-I in the region of 1600-1750 cm^{-1} is the signal-to-noise ratio, which is more than three times better. For a normal aqueous solution sample, the level of signal-to-noise ratio from a single VCD scan is large enough to allow the operator to make some judgments on the sample, such as concentration. Some specific spectra will be present in the next chapter to elaborate on the improvement.

Chapter Four

Performance of Dispersive VCD

In this chapter, the representative data collected on VCD-I and VCD-II demonstrate the performances of these instruments. Some specific comparisons with FT-VCD-PEM reveal the advantages and disadvantages of the dispersive VCD instruments. Topics also discussed here are the improvement of VCD-II over VCD-I in signal-to-noise ratio in the region from 1600 cm^{-1} to 1750 cm^{-1}.

4.1. Performance of VCD-I[32]

The performance of VCD-I can be gauged by considering the spectra, Figures 17 and 18. These are the raw spectra of α-pinene, (+) and (-) respectively, collected on VCD-I in the region of 1050- 1350 cm^{-1}. Both samples were neat liquids (99% pure) from Aldrich, directly used in sample cells with CaF_2 windows without any further purification. The optical purity of (-)-α-pinene is only 81%. The variable

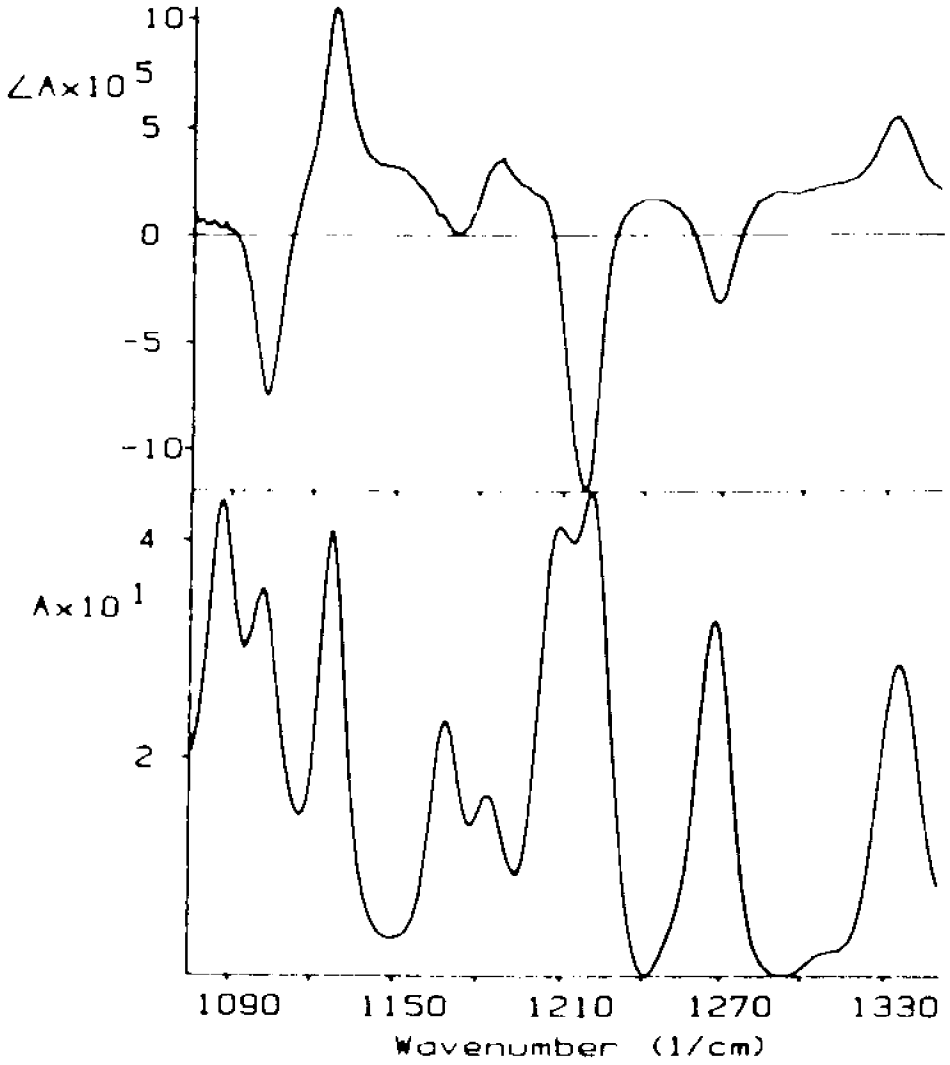

Figure 17. Raw Spectra of Neat (+)-α-Pinene, 50 μm CaF_2 cell, optical purity 98%; top: VCD (10 scans); bottom: IR.

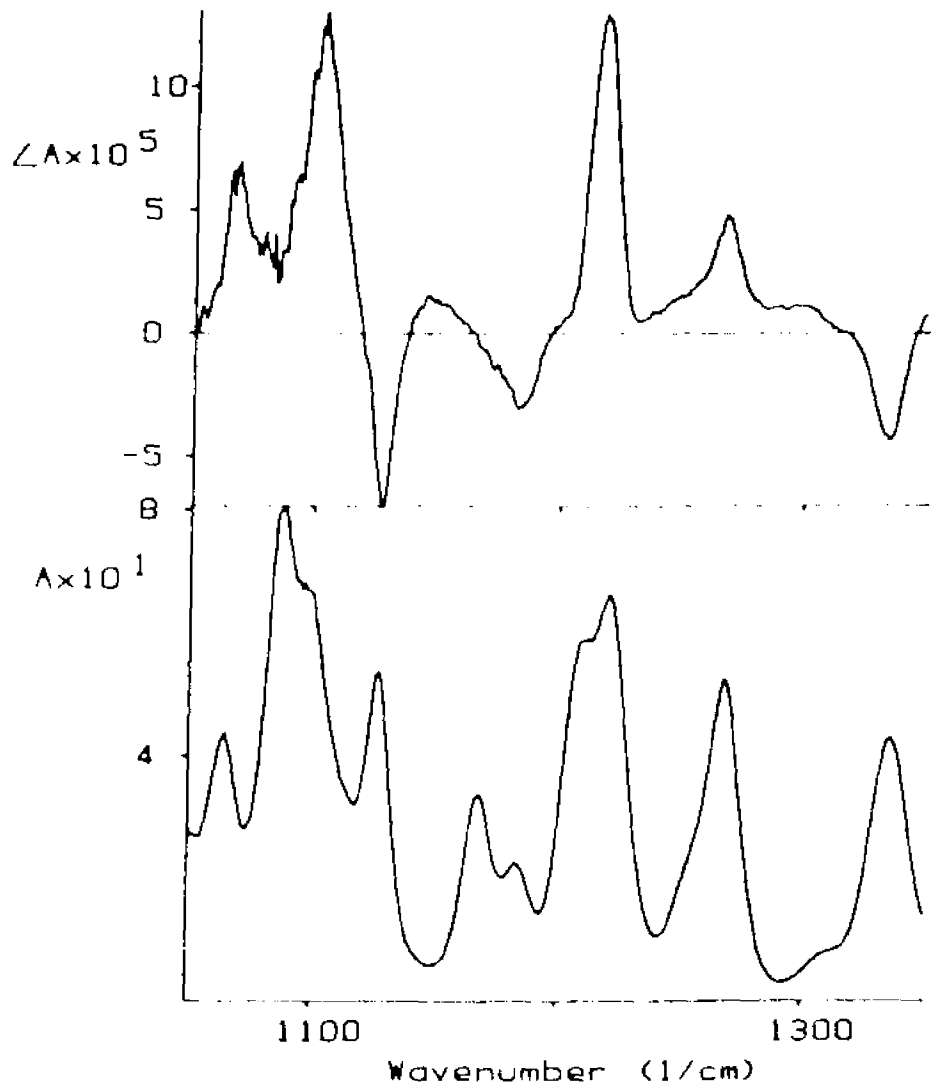

Figure 18. Raw Spectra of Neat (-)-α-Pinene, 100 μm CaF_2 cell, optical purity 81%; top: 10 VCD scans; bottom: IR.

pathlength cell used to contain the sample is set at 100 μm. The optical purity of (+)-α-pinene, however, is 98% and the sample is run in a fixed pathlength cell with a 50 μm teflon spacer. Each VCD spectrum is the average of 10 scans, and it takes two and a half hours to complete the acquisition. Figure 19 displays a randomly selected scan that constitutes Figures 17. It typifies an individual scan, whose scanning time is only 15 minutes with already an excellent signal-to-noise ratio. α-pinene has been a standard for instrument testing in the vibrational optical activity, including both the studies in VCD and Raman optical activity (ROA). The latter technique measures the difference in Raman scattering between left and right circularly polarized laser beam. It is common to utilize an α-pinene spectrum as a performance indicator of a particular instrument. Based on the α -pinene data, a direct comparison of a FT-VCD-PEM instrument and a dispersive instrument, therefore, is possible. There is a little baseline offset in Figures 17 and 18, but an enantiomeric baseline correction is not necessary since all bands are distinct, the baseline is quite flat and the baseline offset is very small.

The excellent signal-to-noise ratio, the small baseline offset, and straight baseline are definitely

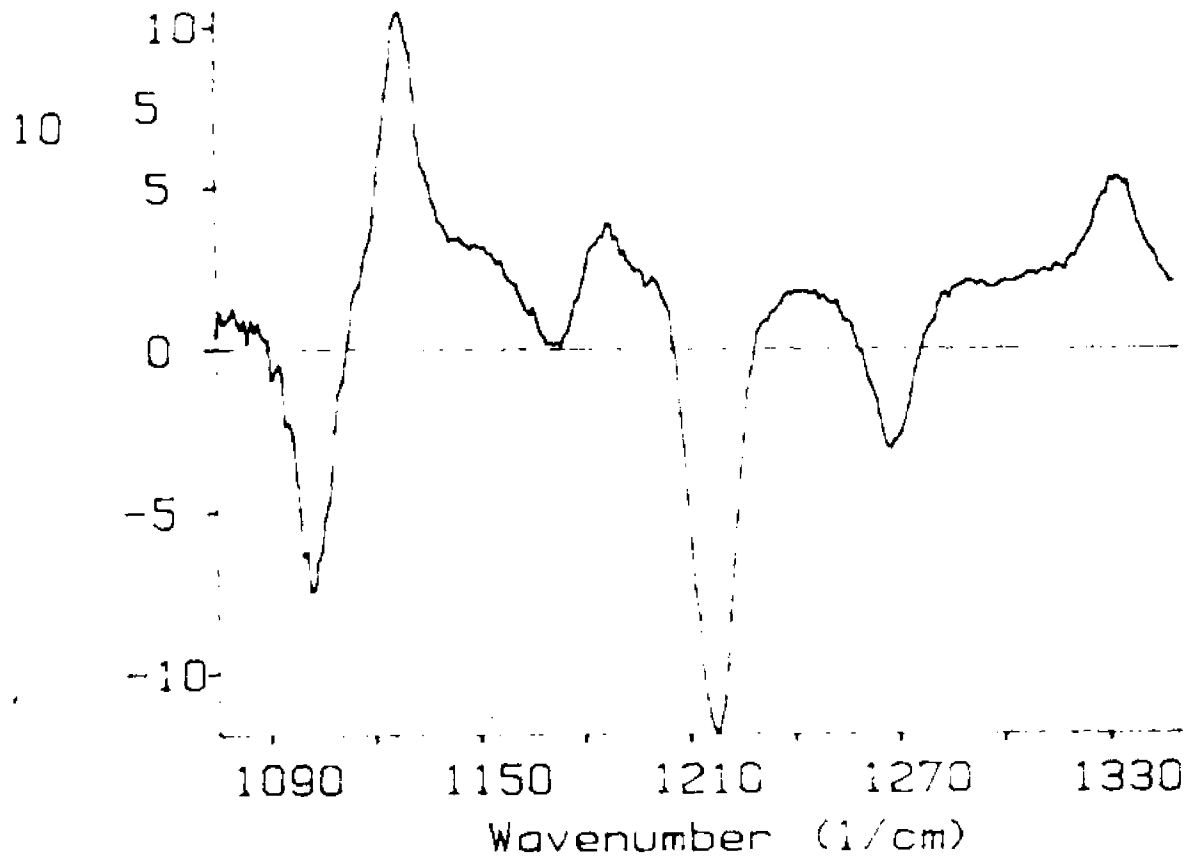

Figure 19. A Single VCD Spectrum from the acquisition of Figure 17; 15 minutes scanning time.

signs of a superior instrument performance. One other indication of the excellent performance of VCD-I is the remarkable quality of Figures 17 and 18 being almost perfect mirror images to each other. This is exactly what optical activity theory predicts.

Next, the spectral difference in Figures 17 and 18 will be discussed. There two major sources, namely the cell pathlength and the optical purity, contributing to the difference. The cell pathlengths ratio of (+)-α-pinene vs. (-)-α-pinene is 0.5. A better measure of the pathlength ratio should be the average ratio of the absorbances for each pair of corresponding peaks in the region. The average is 0.68. It may be used to calibrate the difference between the two cell pathlengths. This difference just about compensates the difference in the optical purities of the two enantiomers: in the (+)-α-pinene sample, the 98% optical purity means it also contains 2% (-)-α-pinene, as a result, VCD intensities are proportional to only 96% neat (+)-α-pinene; for the (-)-α-pinene sample of 81% optical purity (containing 19% (+)-α-pinene), VCD intensities can only be proportional to 62% neat (-)-α-pinene. Hence, the optical purity ratio of (+)-α-pinene versus (-)-α-pinene is 1.54. Since 1/1.54 = 0.65, this factor almost compensates for the pathlength difference. The small dip on the

racemate baseline about 1175 cm^{-1} is believed to be due to a distinct absorption peak that appeared at the same wavenumber on the instrument transmission spectrum. The interference is thought to be the second order diffraction of the CO_2 absorption band at 2350 cm^{-1}.

Figure 20 shows the raw VCD spectrum in the 900-1150 cm^{-1} region of (-)-α-pinene and the instrument baseline by just scanning without sample, not even an empty cell. Again, the spectra are the average of 10 scans, and the scanning time was about two hours each for the sample and the baseline spectrum. The KBr cell of variable pathlength was set at 50 μm. In the spectrum shown, the raw VCD data of (-)-α-pinene are superimposed on a curved baseline, reproducible in the baseline scan. The baseline curve is due to the proximity of the transmission cutoff of the BaF_2 lens. The continuing decline of the baseline is clearly shown in Figure 21. That explains the baseline change between the previous figures from a sloping baseline in Figure 20 to a flat one in Figure 17. Figure 21 is the average of seven scans of neat (-)-α-pinene in a fixed path (50 μm) cell with BaF_2 windows. The total scan time was two hours and twenty

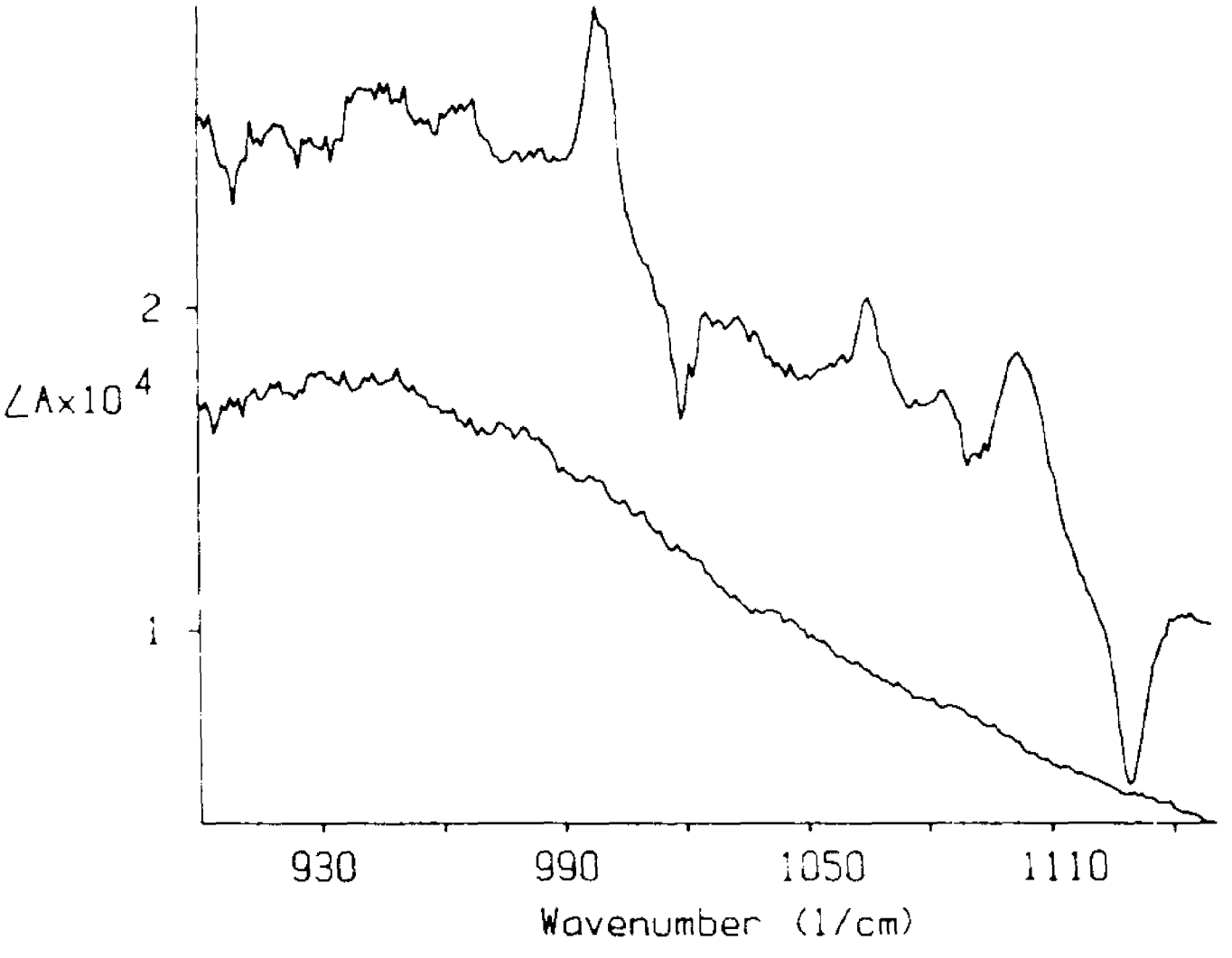

Figure 20. VCD Spectrum of Neat (-)-α-Pinene, in 50 μm KBr cell(upper) and instrument baseline (scanning without sample), 10 scans each.

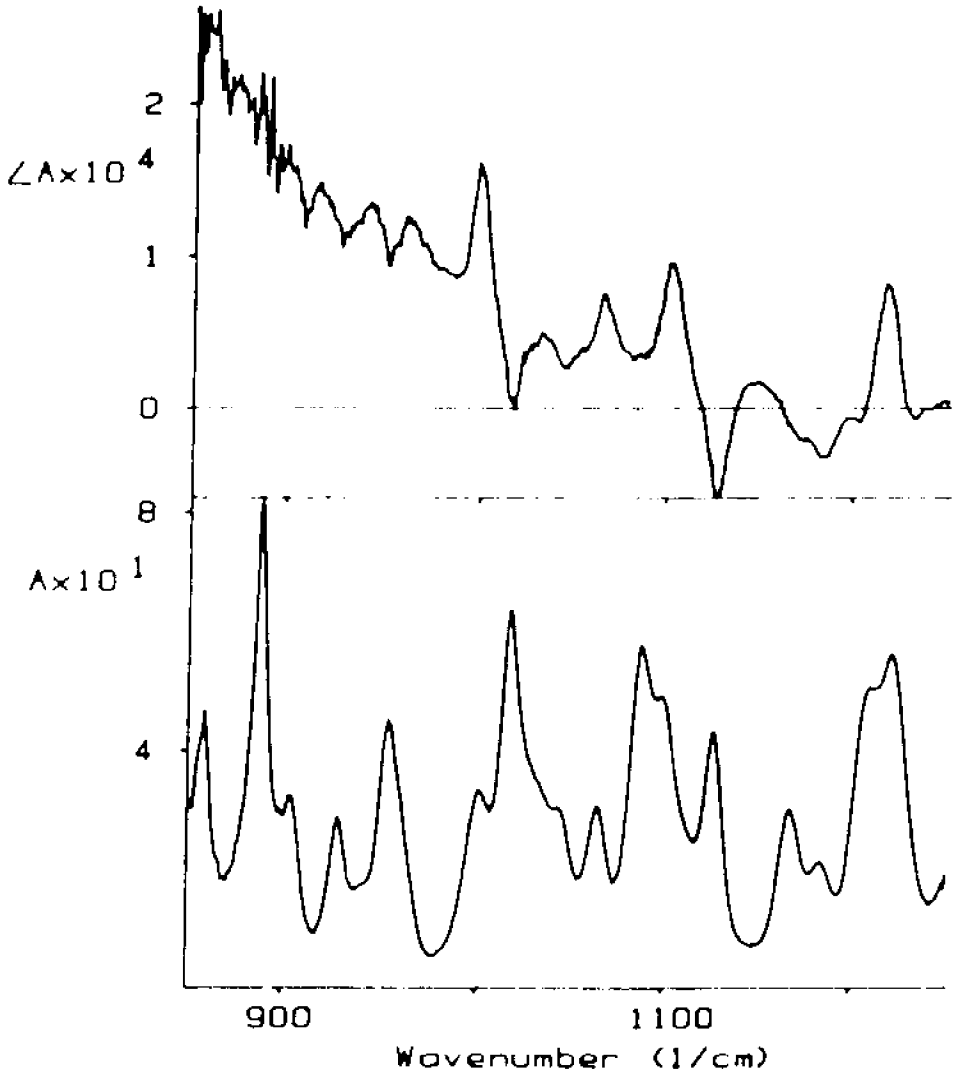

Figure 21. Spectra of Neat (-)-α-Pinene, in 50 μm BaF_2 cell; top: VCD; bottom: IR.

minutes. The noise level increases considerably at the low end of the spectrum because of the BaF_2 lens cutoff. From the spectra shown, the sample absorption obviously does not affect the instrumental baseline, which, therefore, can be subtracted from the sample spectrum easily. Figure 22 shows the VCD spectrum of Figure 20 after baseline correction (top), and its corresponding absorption spectrum (bottom).

The independence of the VCD-I instrumental baseline toward the sample absorbance is an important difference between it and the other instruments built previously. It is important for a VCD instrument to be free of absorbance artifact, so as to avoid the need for the other enantiomer or the racemate to establish the true baseline. This is especially true for samples like large biological molecules because the enantiomer or racemate are not available. The absorbance artifact is one of the major problems troubling the users of FT-VCD-PEM instrumentation, as described in Chapter Two. On the VCD-I dispersive unit, there is no need for a baseline correction in the instances of Figures 17 and 18 for all practical purposes. As a result, scan time and samples are saved. In the lower frequency region (*cf.* Figure 20), a simple subtraction of an instrumental baseline (just VCD scan without a sample), or a solvent base-

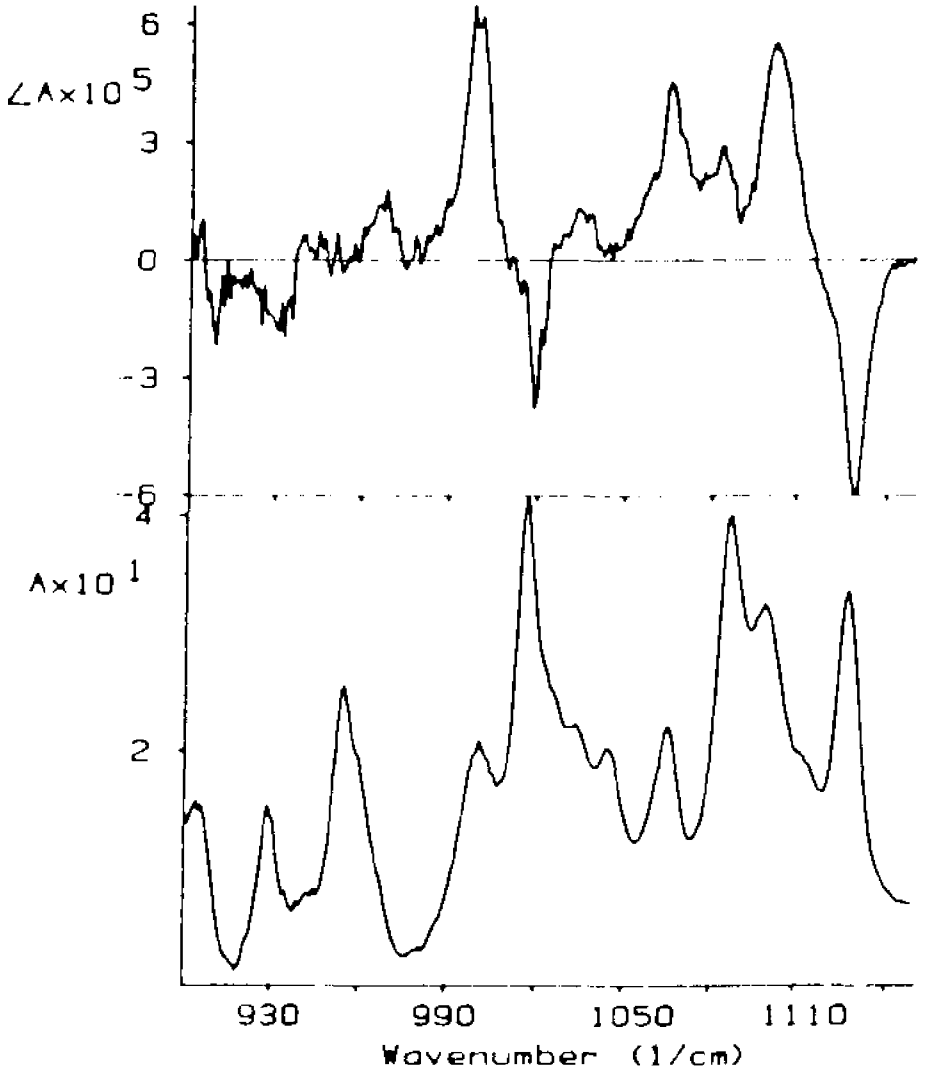

Figure 22. Spectrum of (-)-α-Pinene; top: VCD, Fig.20 after subtracting instrument baseline; bottom: corresponding IR.

line (VCD scans of the solvent only), usually corrects the VCD spectrum of the sample. Since the baseline is perfectly reproducible, using a previously collected solvent (or instrumental) baseline under the same condition is acceptable. However, when VCD signals are very small, the solvent background subtraction method is also utilized even in the high frequency region, 1050-1350 cm^{-1}. Moreover, the enantiomeric or the racemate baseline, when available, has also sometimes been applied as the baseline to ensure the trustworthiness of the spectra. This is especially desirable in cases when signals are not distinct even after multiple scans (30 or more), such as the amide III bands of some small peptides.

Spectra in Figures 18 and 22 are nearly identical to those (-)-α-pinene spectra, collected from FT-VCD-PEM by Nafie *et al.*[48] (*cf.* Figure 23) and by Polavarapu[45], with approximately the same scanning times. The reason for our breaking the spectra into two parts on VCD-I is the need to change the optical filters. One covers 800-1250 cm^{-1}, and the other covers 1050-2000 cm^{-1}.

VCD-I demonstrates some capabilities which compares favorably to FT-VCD-PEM in the high frequency region. In a single VCD scan (*cf.* Figure 19), it

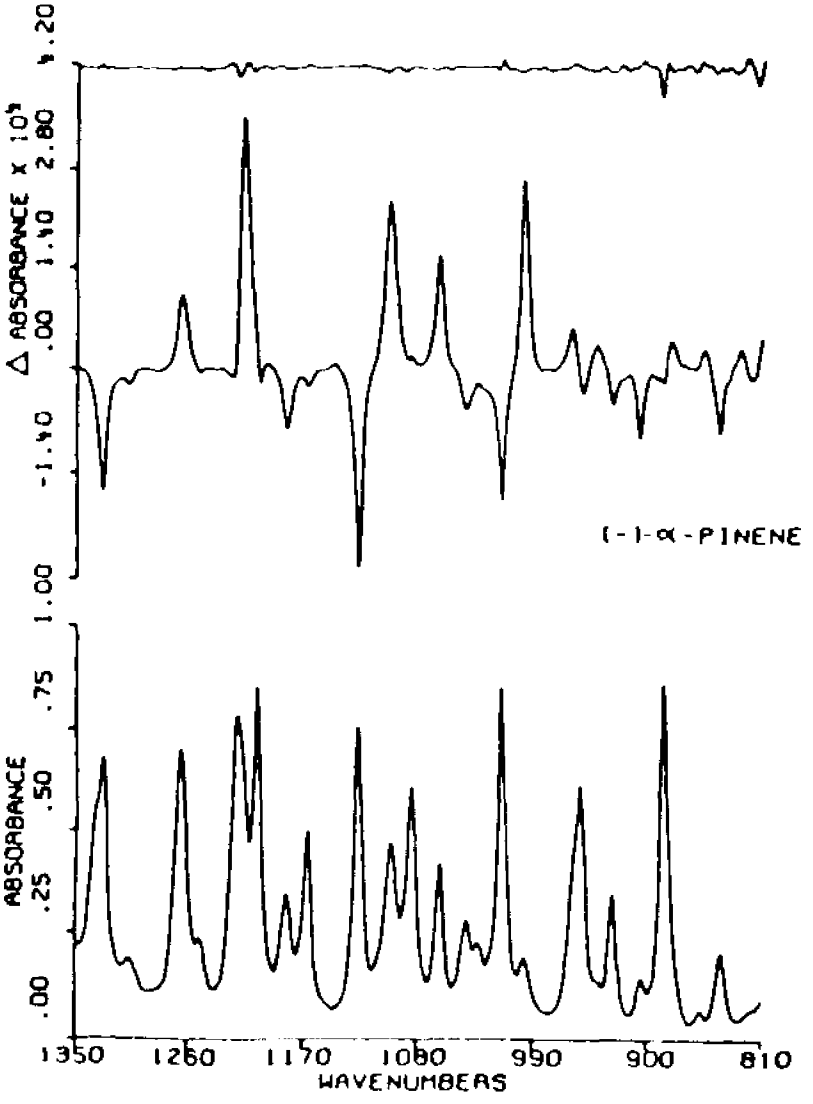

Figure 23. Spectra of (-)-α-Pinene, collected on FT-VCD-PEM, from ref.[48] by Nafie *et al.*

could distinguish all the α-pinene peaks that FT-VCD-PEM has identified. This, combining with the real time display of the spectrum on the screen, enables an operator to monitor the spectrum and, if needed, take appropriate actions promptly. Such actions include making quick judgments on the sample conditions, and identifying and correcting any problems; for instance, too large a sample concentration or too long a cell pathlength. All of these have dramatically improved the reliability of VCD measurement, and saved a lot of experimental time.

The VCD-I instrument benefited from a dramatic improvement when the BaF_2 lens was unexpectedly popped out its mount and dropped on the optical table. That resulted in a massive crack going through the entire lens, though the lens did not break. Figure 24 is a typical spectrum of (-)-α-pinene before the lens cracking accident. Comparing to Figure 18 for the exact same sample, the baseline offset almost disappeared as the result of the lens cracking! The explanation may be a release of stress in the BaF_2 crystal, the lens material. This stress was most likely caused by the machining of the curved surfaces of the lens. The dropping and subsequently cracking of the lens released the tension within the lens. As discussed in section 2.1.2, an isotropic

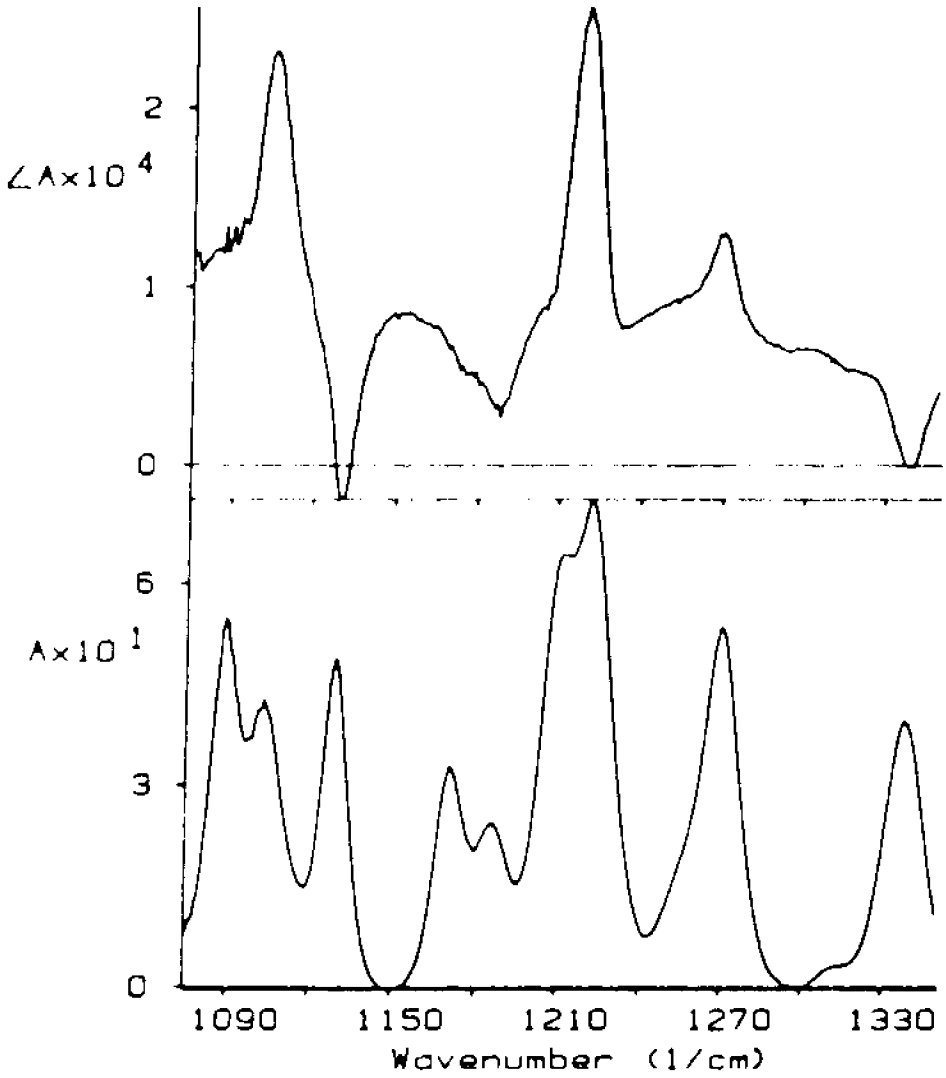

Figure 24. VCD Spectrum of Neat (-)-α-Pinene, in 50 μm CaF_2 cell, 10 scans, before cracking BaF_2 lens.

crystal can be birefringent when it is under stress. The birefringence accounted for the baseline offset in the VCD spectrum. The lesson here is that all lenses, maybe even all refractive optical components, used in a VCD spectrometer should be stress free. A number of methods can be used. For example, after the grinding, the lens should be heated to a temperature just below the crystal melting point, then permitted to cool down extremely slowly. This would allow the crystal unit cell to realign, and release the stress in the lens.

As stated in Chapter Three, VCD-I was designed for the studying amide I, II and III vibrations of small peptides. Following are some VCD and corresponding IR absorption spectra of L-alanine, L-alanyl-L-alanine and L-alanyl-L-alanyl-L-alanine, respectively. They exemplify the performance of VCD-I for peptides in aqueous solution. To run a VCD spectrum of a neat liquid has become trivial (*e.g.*, α-pinene) because of its high concentration and no solvent interference. However, running a sample in aqueous solution is much more difficult, because of the strong water absorption and low sample concentration. It is a remarkable achievement to observe high quality VCD spectra in aqueous solution. All the VCD spectra in this group of samples have been corrected

with enantiomeric background since all the enantiomers (D-alanyl peptides) were available. For the amide III region, the samples were directly weighed and dissolved in H_2O. For amide I region, the samples were deuterated by first dissolving in excess D_2O, lyophilizing, then again dissolving in an exact amount of D_2O to produce the desired concentration. Thus, the amide I' mode (the prime denotes a deuterated peptide linkage) was actually observed. Figure 25 and 26 are the spectra of L-alanine in the amide III region (1250-1500 cm^{-1}) in H_2O and D_2O, respectively[76]. The two solution concentrations were the same, 1.2 M, and so were the cell pathlengths, 15 μm. Each spectrum is the average of 8 scans and the total scanning time is one hour and forty minutes each. The assignment for the positive-negative couplet at 1307 and 1355 cm^{-1} in H_2O solution are the two C_α-H deformation modes[58,62], the vibrational motions of which are perpendicular to each other. Of course, there is no amide linkage in this molecule.

L-alanyl-L-alanine data were collected in a fixed path cell with CaF_2 windows and 15 μm teflon spacer. Figure 27 shows 10 VCD scans from 1250 to 1500 cm^{-1}, and total data acquisition time was two hours, with a sample concentration of 0.5 M. The peak

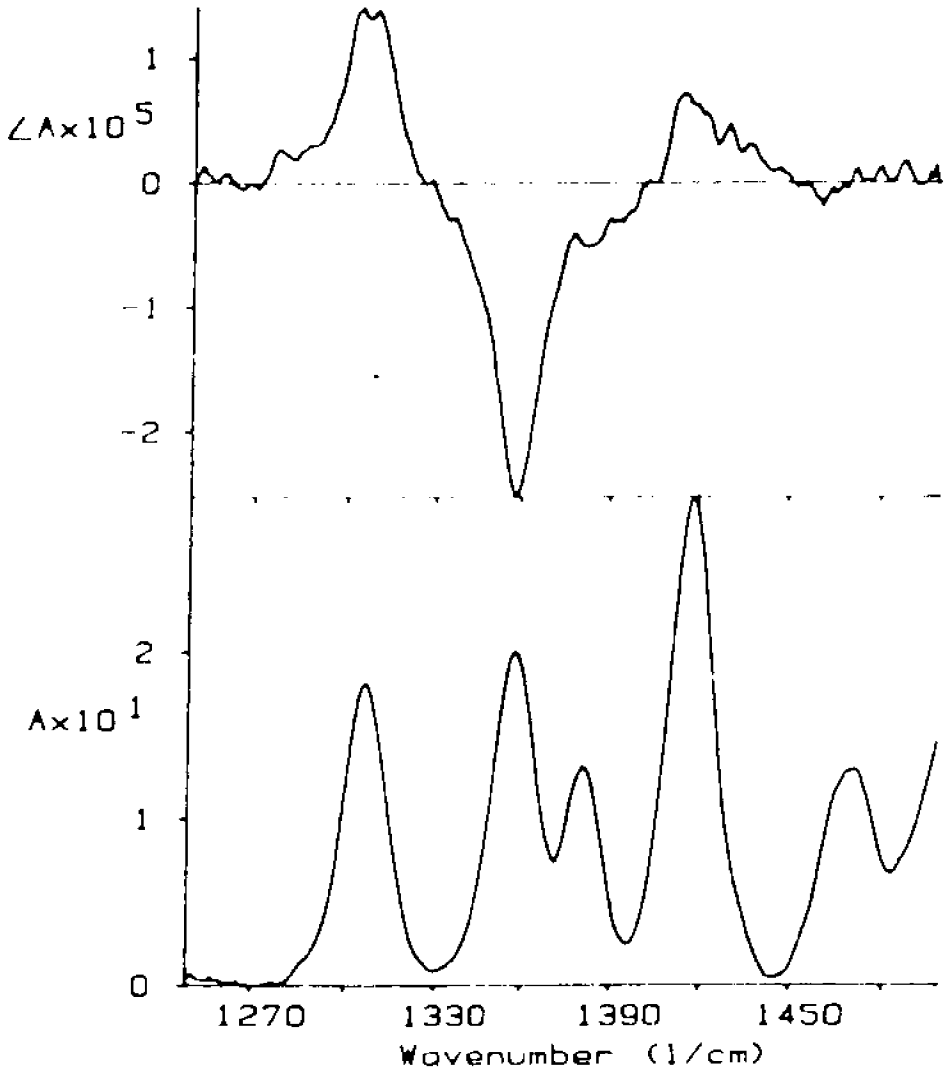

Figure 25. Spectra of L-Alanine, in 15 μm CaF_2 cell, 1.2 M in H_2O; top: VCD, 8 scans average, enantiomeric baseline corrected; bottom: IR.

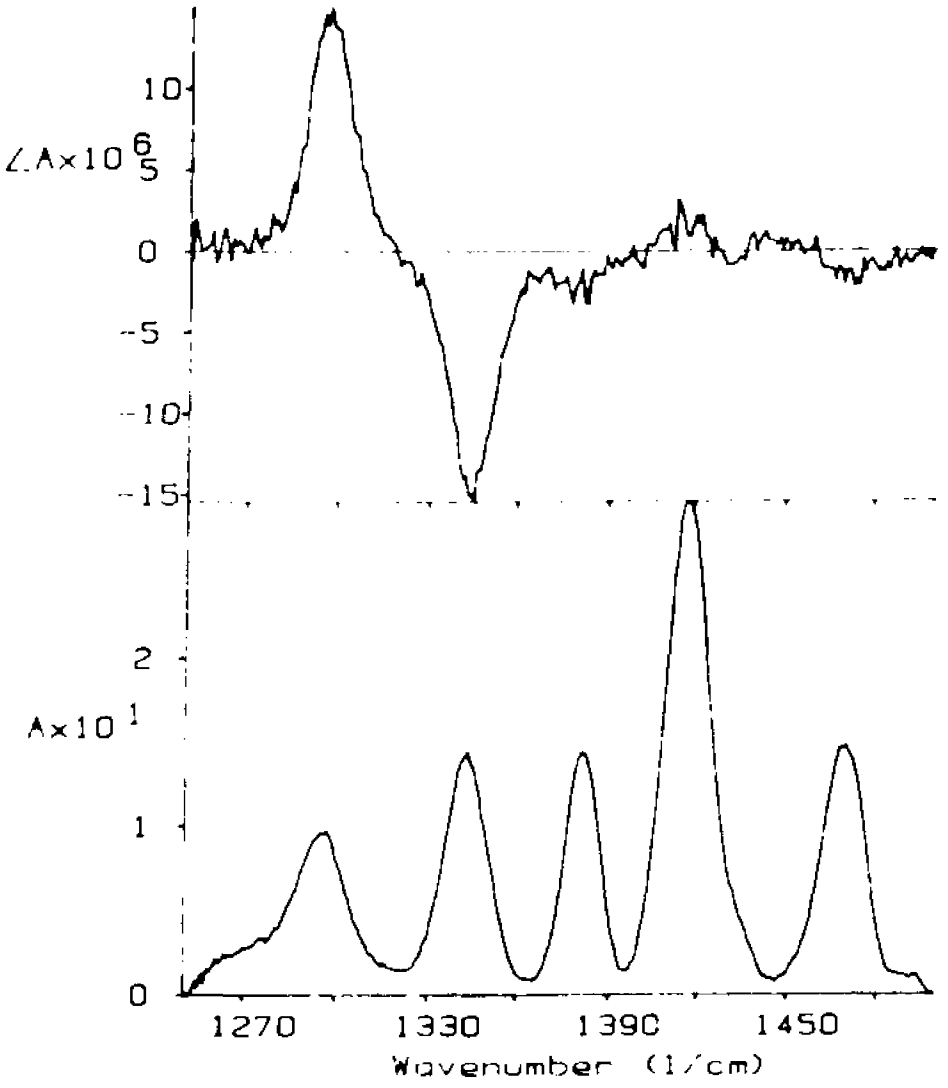

Figure 26. Spectra of L-Alanine, in 15 μm CaF_2 cell, 1.2 M in D_2O; top: VCD, 8 scans average, enantiomeric baseline corrected; bottom: IR.

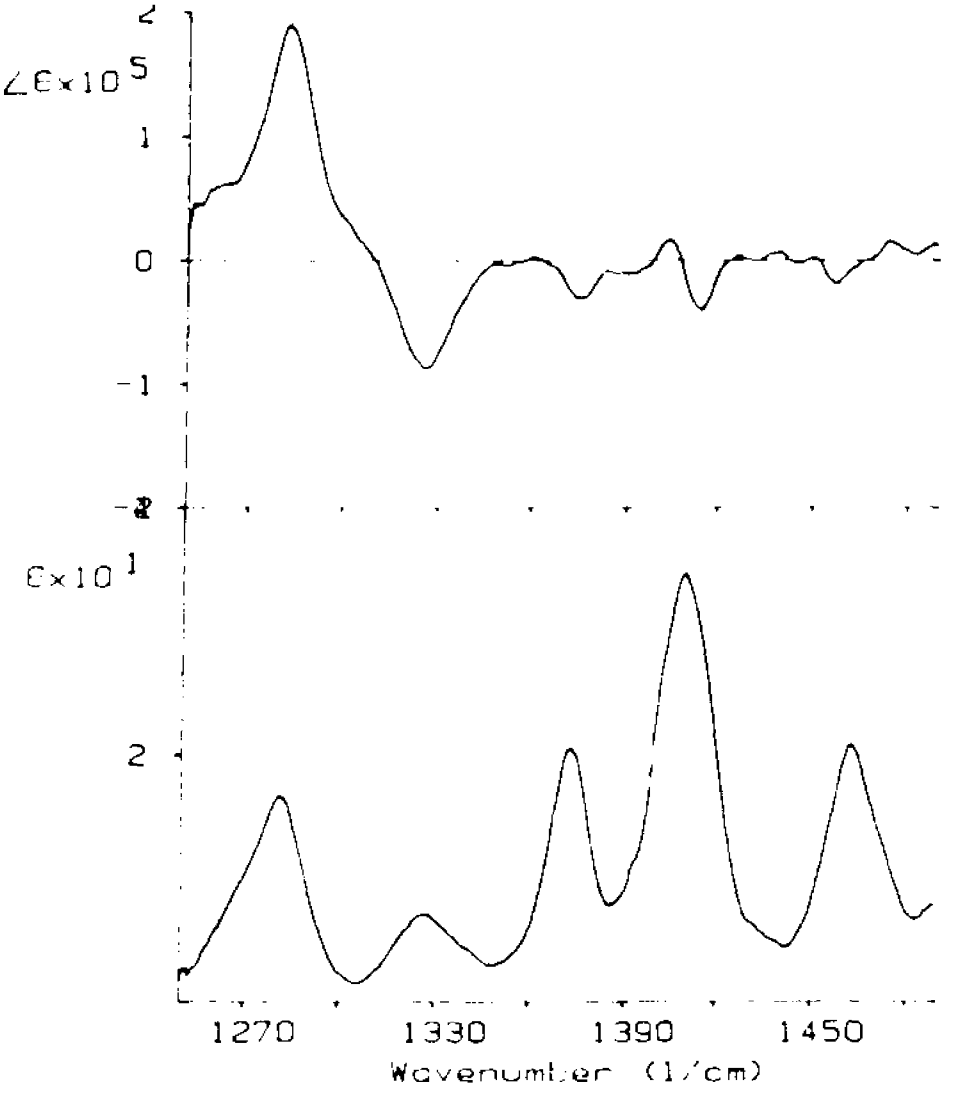

Figure 27. Spectra of L-Alanyl-L-Alanine, in 15 μm CaF_2 cell, 0.5 M in H_2O; top: VCD, 10 scans average, enantiomeric baseline corrected; bottom: IR.

at 1285 cm^{-1}, traditionally called the Amide III band, was distinct in H_2O in both VCD and IR absorption. This peak is about three times as high as the next peak at 1295 cm^{-1}. Figure 28 and 29 are the spectra of L-alanyl-L-alanine in D_2O, in the amide III' and the amide I' regions, respectively. The VCD spectra are also 10 scans averaged. The sample concentration was 1.0 M in Figure 28, and was 0.5 M in Figure 29.

There are some obvious changes in the amide III' region, comparing Figure 28 to Figure 27. The next chapter will address the interpretation of these spectral changes. Here the emphasis is on the observation that there is not much VCD signal at the Amide I' band 1675 cm^{-1} (*cf.* Figure 29).

Next, Figure 30 is the infrared absorption and VCD spectra of L-alanyl-L-alanyl-L-alanine in H_2O from 1250 to 1425 cm^{-1}. The sample concentration is 0.65 M. Figure 31 is the infrared absorption and VCD spectra of L-alanyl-L-alanyl-L-alanine in D_2O from 1250 to 1750 cm^{-1}. The VCD spectrum is the average of 10 scans. The sample concentration is 0.493 M, and a fixed path cell used a 15 μm teflon spacer and CaF_2 windows, as well. The most interesting observation of Figure 31 was that amide I' peaks show a distinct negative-positive couplet. Figure 32 is the raw VCD spectra of L-alanyl-L-alanyl-L-alanine, D-alanyl-D-

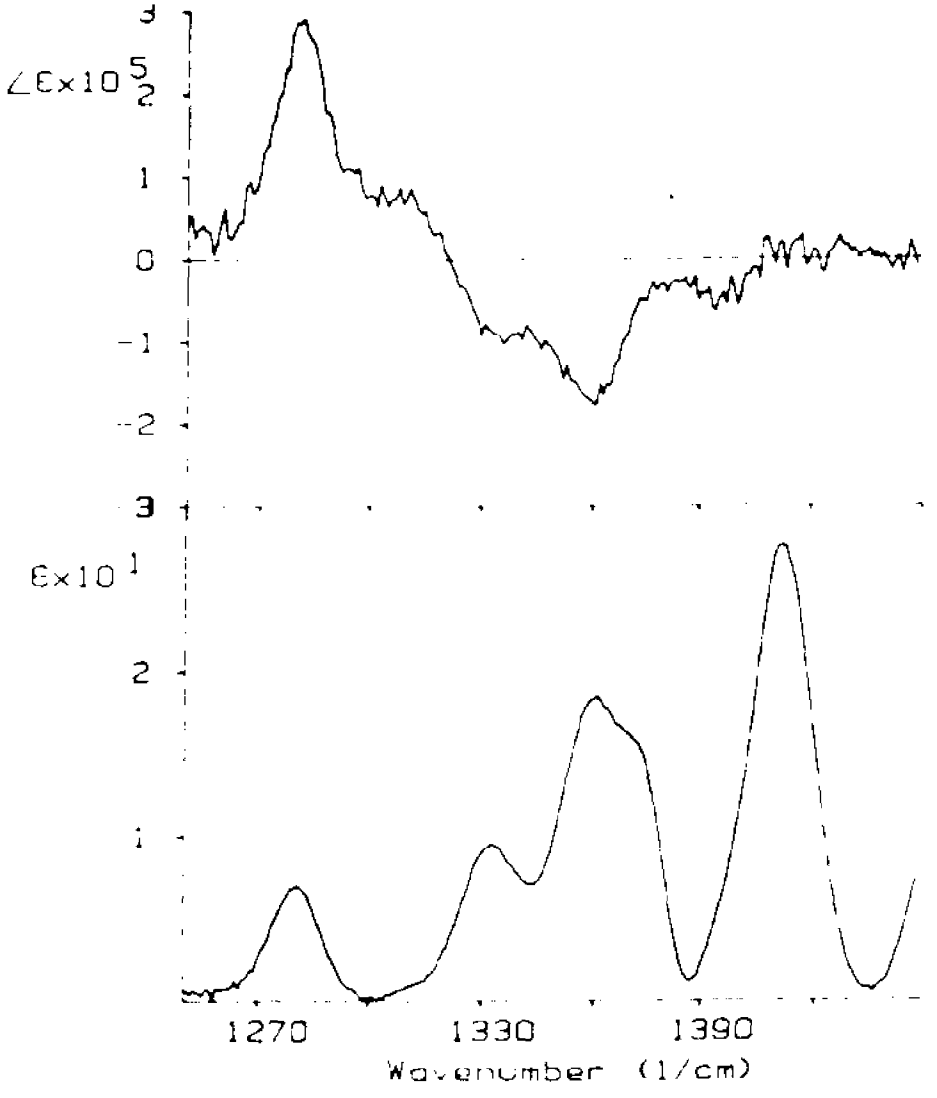

Figure 28. Spectra of L-Alanyl-L-Alanine in 15 μm CaF_2 cell, 1.0 M in D_2O; top: VCD, 10 scans average, enantiomeric baseline corrected; bottom: IR.

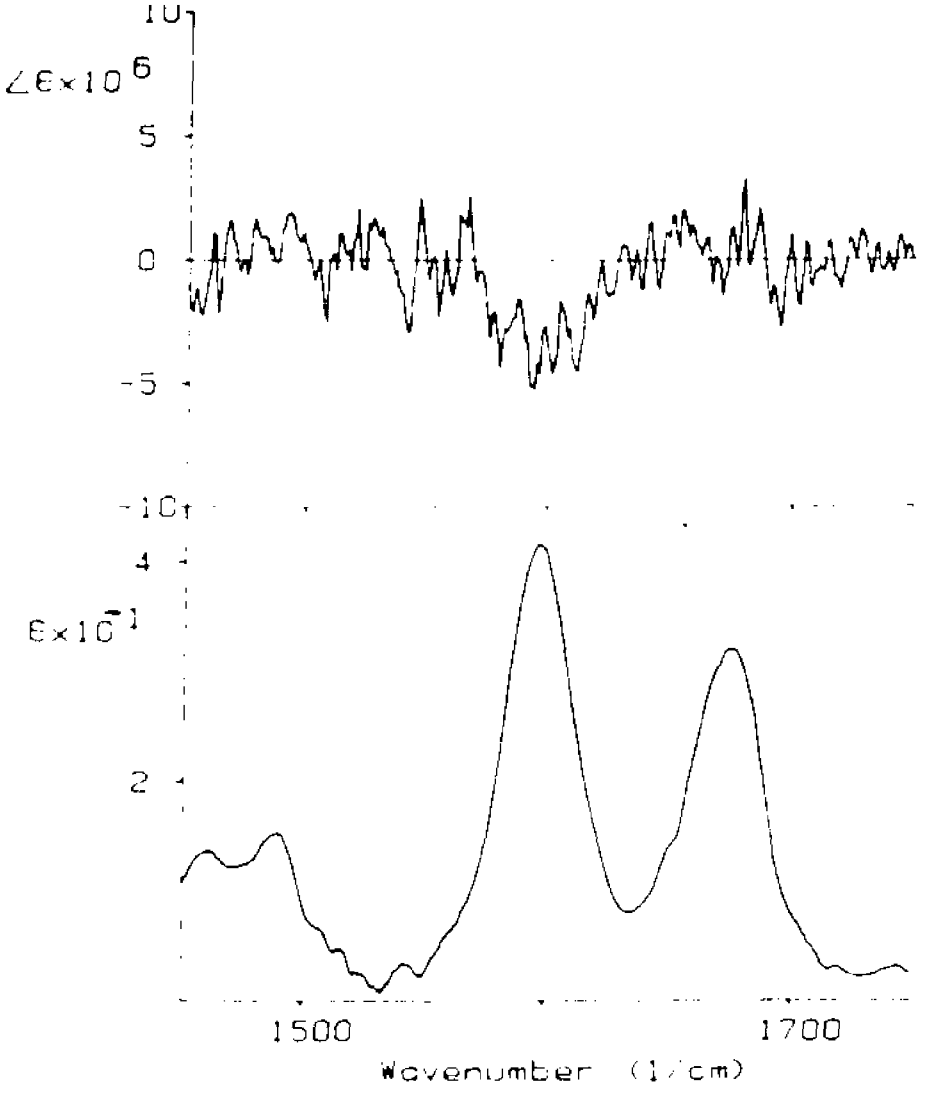

Figure 29. Spectra of L-Alanyl-L-Alanine in 15 μm CaF_2 cell, 0.5 M in D_2O; top: VCD, 10 scans average, enantiomeric baseline corrected; bottom: IR.

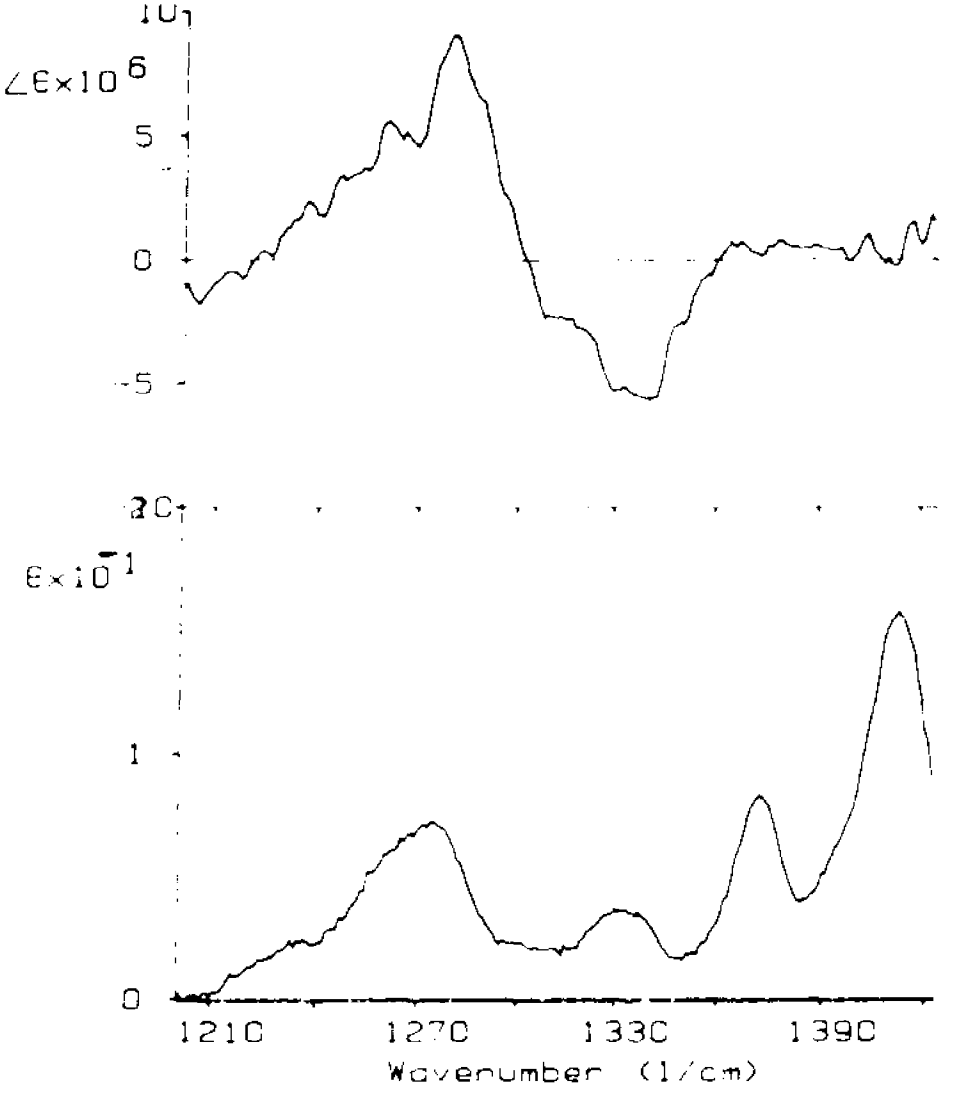

Figure 30. Spectra of L-Alanyl-L-Alanyl-L-Alanine in 15 μm CaF_2 cell, 0.65 M in H_2O; top: VCD, 10 scans average, enantiomeric baseline corrected; bottom: IR.

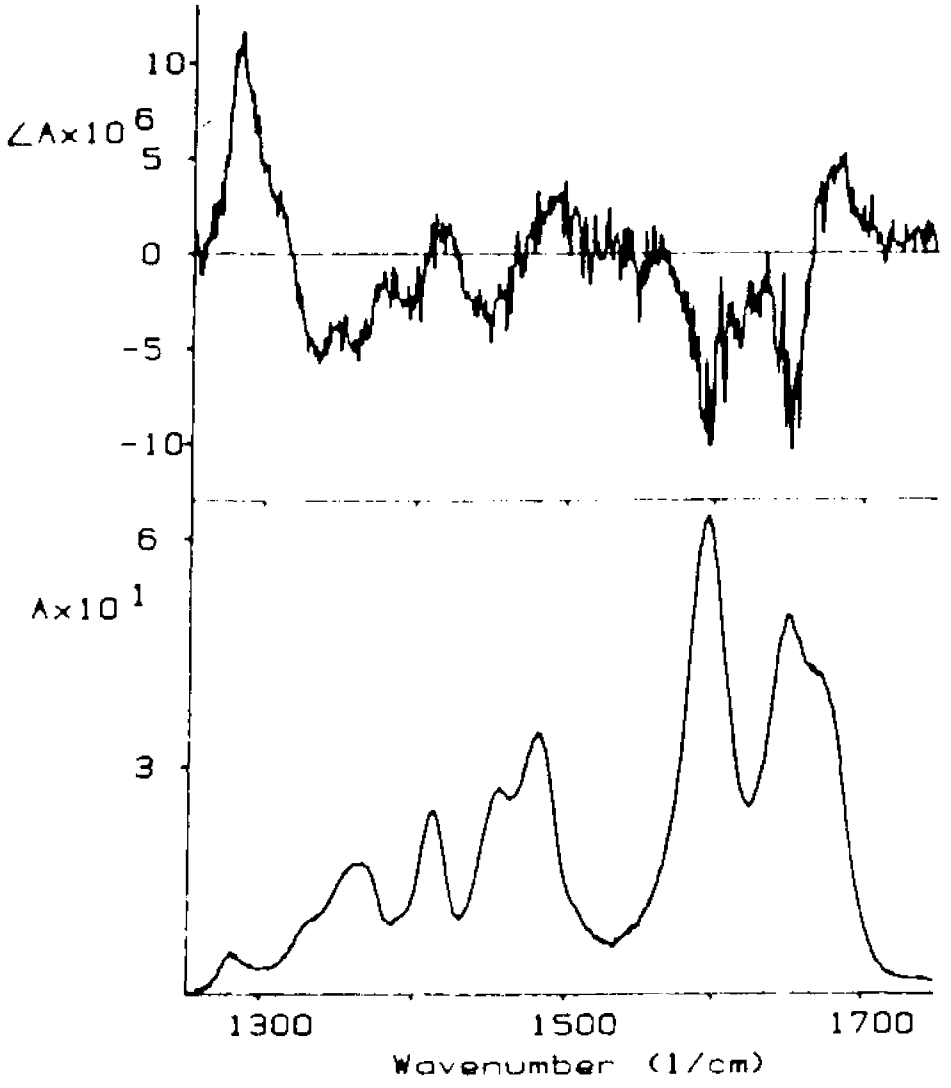

Figure 31. Spectra of L-Alanyl-L-Alanyl-L-Alanine in 15 μm CaF_2 cell, 0.49 M in D_2O; top: VCD, 10 scans average, enantiomeric baseline corrected; bottom: IR.

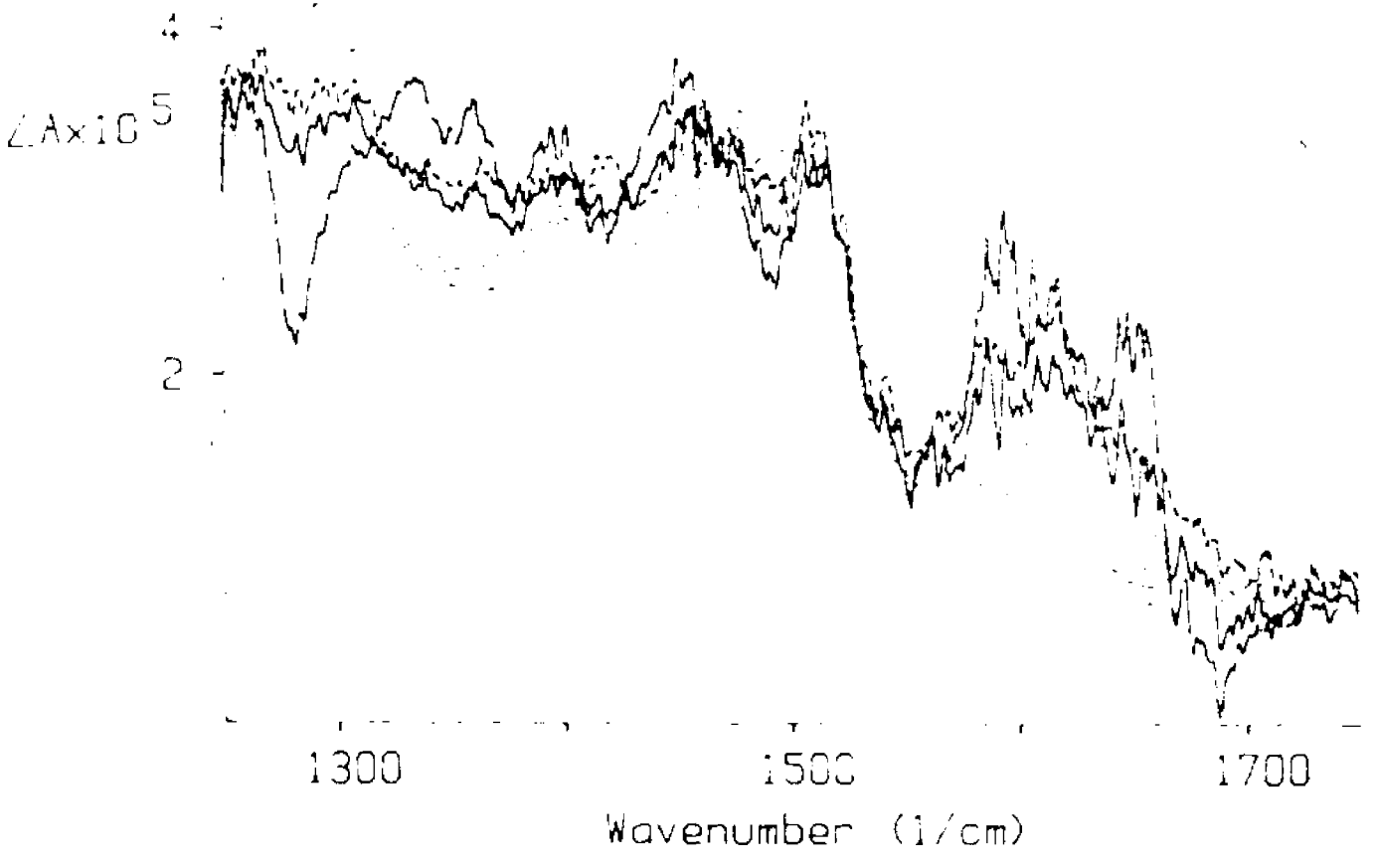

Figure 32. Raw VCD Spectra of L-alanyl-L-Alanyl-L-alanine (···) and D-alanyl-D-alanyl-D-alanine (-·-); same condition as Fig.31; and Enantiomeric baseline (——) and D_2O (---).

alanyl-D-alanine, the enantiomeric background (the average of L-alanyl-L-alanyl-L-alanine and D-alanyl-D-alanyl-D-alanine), and D_2O. Figure 31 is the result of the raw VCD spectrum of L-alanyl-L-alanyl-L-alanine after subtracting the enantiomeric background. As another clear demonstration of the instrument independence of the sample absorbance, the VCD spectrum of D_2O follows exceptionally close to the spectrum of the enantiomeric background. This also means that the VCD spectrum of D_2O can be used in place of the enantiomeric baseline. The close agreement between the D_2O VCD and the enantiomeric baseline reaffirms the reliability of the method of subtracting the solvent VCD as the baseline on the VCD-I instrument, for all practical purposes. The overall slope of the VCD baseline mimics the D_2O transmission spectrum. The spectra shown above, collected within reasonable scanning time, exhibit good signal-to-noise ratio. The interpretation of those spectra will be the subject of the next chapter.

4.2 Dispersive VCD vs. FT-VCD-PEM

In this section a direct comparison of FT-VCD-PEM and the dispersive instrument describes the advantages and disadvantages of the two techniques. The comparison is possible, based on the (-)-α-pinene spectra collected on the Hunter College dispersive VCD unit and the published spectra collected on a Fourier transform infrared VCD unit with a photoelastic modulator (FT-VCD-PEM) under the same conditions [48]. The discussion concentrates on several specific aspects.

FT-VCD-PEM instruments' performance has been superior to those early versions of the dispersive instrument in many respects, such as scanning time and spectral resolution. But unlike FT-IR absorption spectroscopy, FT-VCD-PEM has not become a dominant technique. In Chapter Two, several general problems that limit the FT-VCD-PEM from exercising the full advantages associated with Fourier transform method were discussed. Since the 1980s, dispersive systems have been improving. The popular perception that FT-IR is always much better than dispersive IR is not necessarily true here, and the dispersive VCD still has its advantages. As a result, the two experimental approaches will co-exist in the foreseeable future,

and be complementary to each other because each meets different criteria according to specific problems.

Figure 23 shows the VCD and the corresponding IR spectra of (-)-α-pinene, published by Nafie, *et al.*[48], collected on a FT-VCD-PEM instrument. Figure 23 has a similar signal-to-noise ratio as Figure 18, the same sample collected on VCD-I. The total time of six and half hours for data acquisition on the dispersive unit, covering a similar range (Figure 18 + Figure 22), is only a little longer than the time of 5.5 hours the FT-VCD-PEM unit took. Although FT-VCD-PEM reportedly has since been further improved (in a private communication, Prof. L.A. Nafie indicated that the data acquisition time on their newly optimized FT-VCD-PEM had been shortened somewhat), the expected FT-IR advantage, of about two orders of magnitudes time saving, has not been materialized. Noticeably, the impressive capability for the dispersive instrument of a 15 minute, single scan (*cf.* Figure 21) in the high frequency region is a particular show of strength.

More importantly, for the specific sample of α-pinene, the Hunter College dispersive instrument has demonstrated that the instrument baseline does not depend on the sample absorbance. In the high frequen-

cy region, there is little offset and almost no baseline correction is needed, while in the low frequency region the sloping baseline, due to the transmission cutoff of the BaF_2 lens, can be easily corrected by a simple subtraction of a solvent (or instrumental) VCD spectrum. This eliminates the dependence on the enantiomer or the racemate for the baseline correction, yet maintains the reliability of the VCD signal from only one enantiomer. By contrast, with the exception of Keiderling's new "lens set-up", the data from all other FT-VCD-PEM must employ an enantiomeric or a racemate baseline correction since the VCD spectra are superimposed on the corresponding absorption spectra. That is, in additional to a large offset and a sloping baseline, a VCD spectrum also resembles partially the corresponding absorption spectrum. The only exception is a modified FT-VCD-PEM in Keiderling's laboratory at the University of Illinois at Chicago[46,6]. It uses a lens, instead of the conventional ellipsoidal mirror, after the sample in the optical path to focus the light onto the detector. This drastically reduces the offset and artifacts in VCD spectra, enabling reliable VCD measurement from a single enantiomer to be made. However, such a change also brings an additional difficulty to the software, as discussed in Chapter

Two, and needs extra software and hardware efforts, to overcome the difficulty.

FT-VCD-PEM has achieved simultaneous coverage of the entire mid-infrared region (850-1900 cm^{-1}) with a moderately high resolution (better than 4 cm^{-1}). This is very attractive for applications of analytical purpose. Also, there is definitely an advantage for FT-VCD-PEM in view of the commercial application: to a moderately priced, high quality FT-IR instrument add a few components, both in hardware and software, and FT-VCD-PEM can be achieved, whereas a dispersive unit has to be specially designed and built at a similar or higher cost.

An intriguing issue is which approach is better suited to a specific situation. The VCD technique is most useful for molecular conformation study in solution, specially, of biologically significant molecules. In the infrared, solvent absorption bands present considerable interference problems that permit the collection of VCD data only in several regions of spectral windows. Thus, in most cases, a set of spectra must be acquired in different solvents to form a complete VCD spectrum, say from 600-3500 cm^{-1}. However, the "complete" spectrum is often not wanted, and data for one or a few bands would be

become the dominant technique in the field of vibrational circular dichroism.

4.3 Performance of VCD-II[61] and its improvements vs. VCD-I in the region between 1600 - 1750 cm^{-1}

The spectra calculated via the coupled oscillator model (COM) as a function of the molecular conformation (*cf.* Chapter Two) compare reasonably well the observed VCD spectra for the C=O stretching region. The derived molecular conformation, in turn, is used to interpret the observed spectra. The initial success with several small peptide samples in the amide I' region led to other research projects involving polypeptides and DNA model samples, which greatly broadened the systems in which our research group is involved. The COM calculation for the DNA data has also resulted in very favorable agreements. However, DNA data collected under normal conditions do show poorer signal-to-noise ratio. Therefore, multiple scans needed to improve the S/N ratio took a long data collection time. The encouraging, yet to be improved, results in the 1550 - 1750 cm^{-1} region on both larger peptides and DNA samples demonstrated the need for a dedicated instrument for this region. This was the justification for building the second VCD instrument. The main designing improvements for the VCD-II were a higher detector sensitivity, a better resolution (6 cm^{-1}), as well as better dry air purging

than that of the VCD-I.

Figure 33 (part of Figure 31) and Figure 34 are spectra of L-alanyl-L-alanyl-L-alanine, obtained under the same conditions from VCD-I and VCD-II, respectively. Figure 33 is the average of 10 scans on VCD-I. Figure 34 is the average of 10 scans on VCD-II and Figure 35 is one single scan out of Figure 34. The signal-to-noise ratio of the spectrum in Figure 33 and those of Figure 35 are about the same! This translates to an improvement the signal-to-noise ratio by a factor of more than three (square root of 10). Similar spectral improvements were reported by M. Gulotta from our research group on her samples of some small DNA model oligomers.

Moreover, the ability to identify VCD signals in a single scan is really helpful. In cases where the sample condition or the instrument settings are not chosen appropriately, the operator can, during the first scan, recognize that a problem exists, and take proper action to correct the problem. This saves a lot of valuable time and sample.

In addition, since the throughput of VCD-II is higher than VCD-I, it allows use of a longer cell pathlength (up to 100 μm). That, in turn, gives some flexibility in the concentration requirement (down to

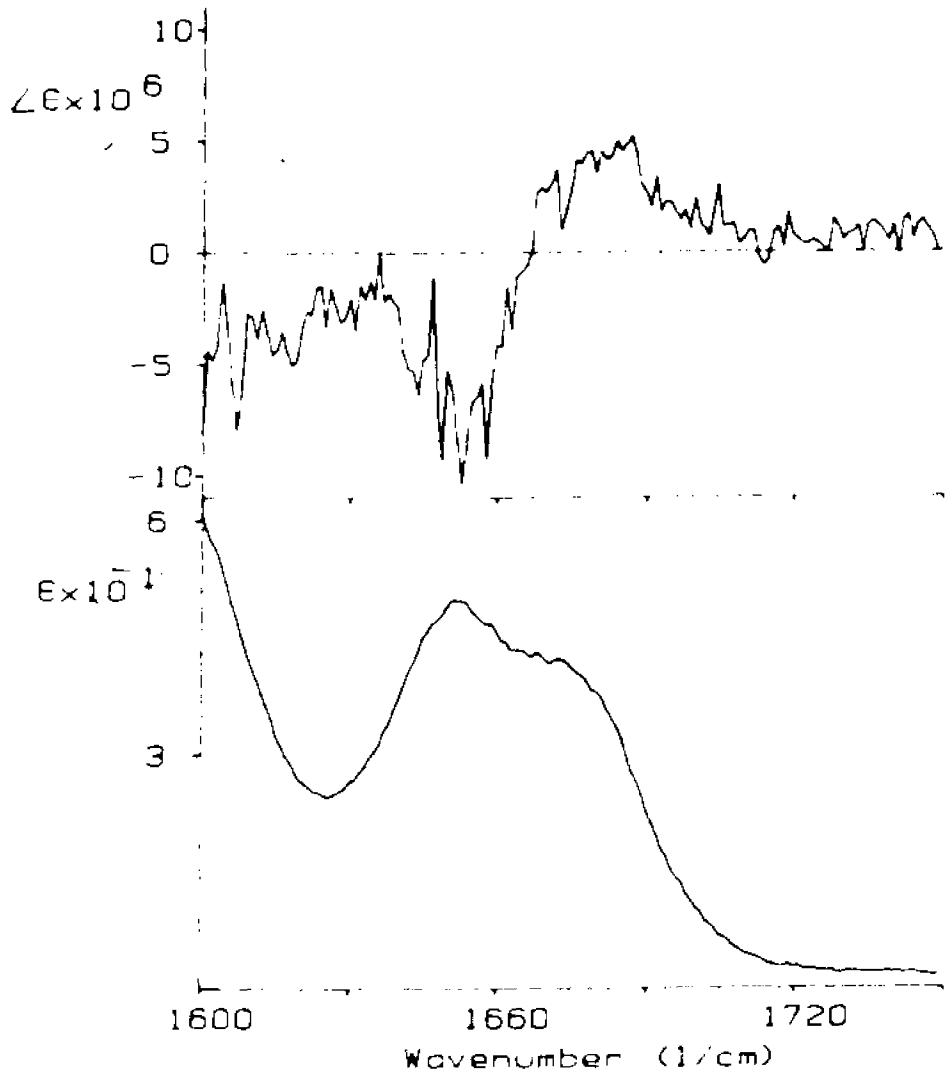

Figure 33. Spectra of L-Alanyl-L-Alanyl-L-Alanine, collected on VCD-I, part of Fig.31.

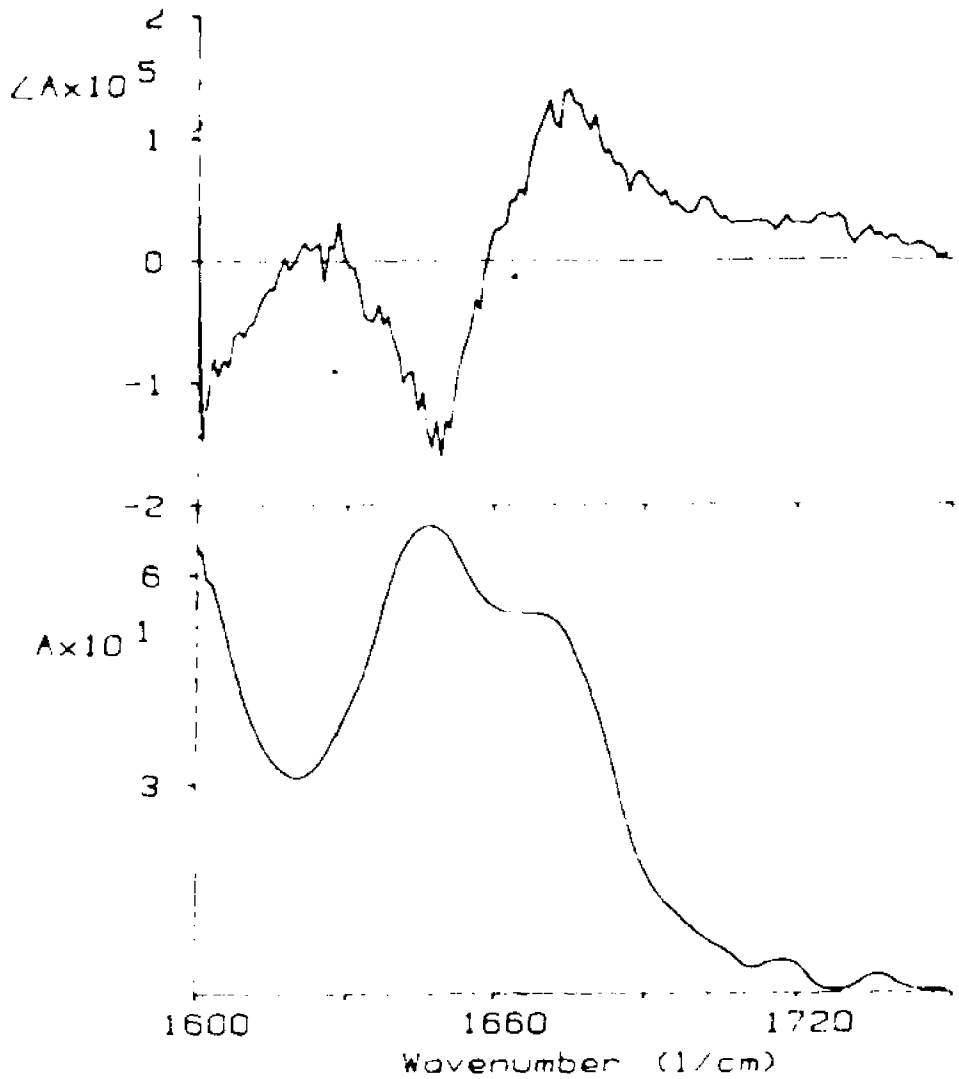

Figure 34. Spectra of L-Alanyl-L-Alanyl-L-Alanine, collected on VCD-II, 0.5 M in D_2O, CaF_2 windows, 15 μm spacer; top: VCD(10 scans) enantiomeric baseline corrected; bottom: IR.

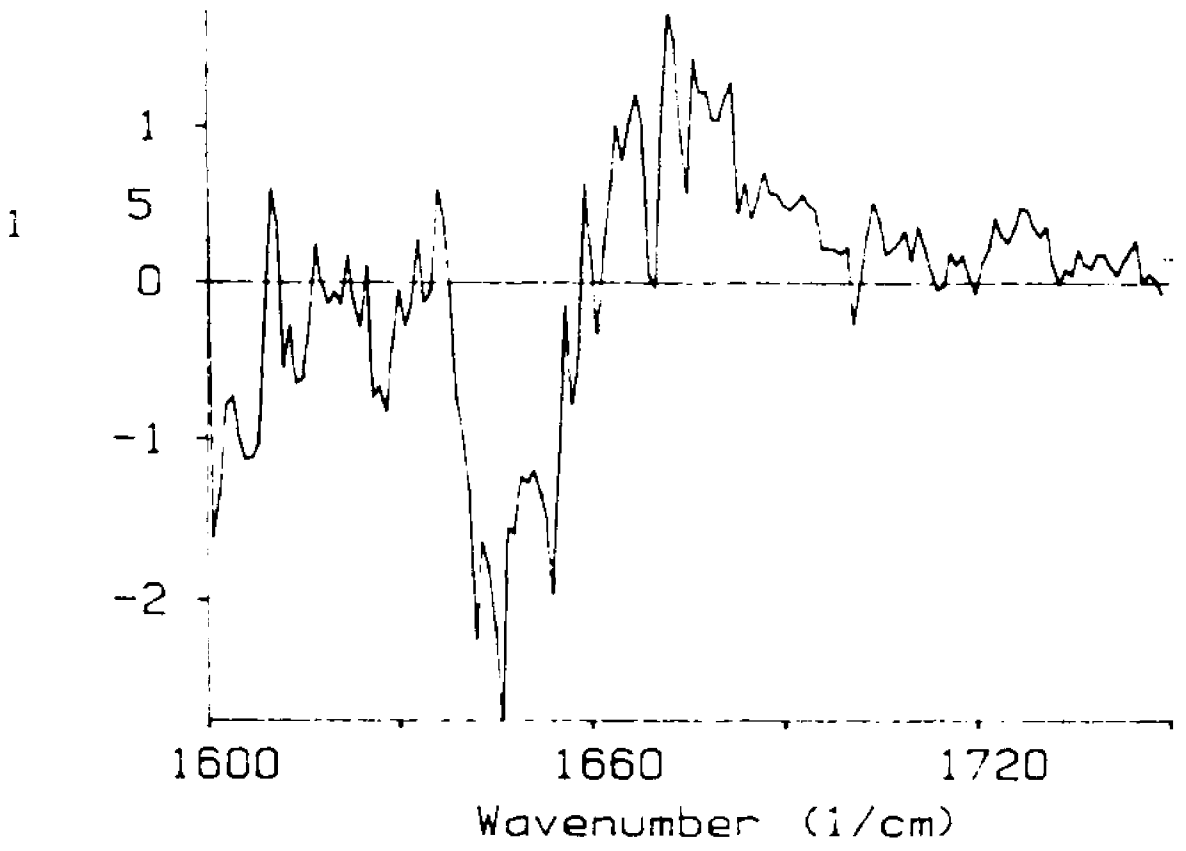

Figure 35. Single VCD Spectrum of L-Alanyl-L-Alanyl-L-Alanine, collected on VCD-II, same condition as Figure 34.

a few mg/ml).

Because of the substantial absorption of water, VCD-I can only use 15 μm or 25 μm spacers. The 15 μm teflon spacer corresponds to the thinnest one found commercially. As a result, the sample usually had to be made as concentrated as possible (30 mg/ml or higher). It is not so on VCD-II.

Since VCD-II is covering the 1600-1750 cm^{-1} region, the strong absorption by atmospheric water vapor in this same region interferes with the VCD measurement. To avoid such interference, VCD-II needs not only a good dry air purging, but also an air-tight configuration to keep humid air out. The new design incorporates a sealed enclosure with an isolated sample chamber. Whenever changing the sample cell, as normally done for any single beam instrument, the outside humid air can only enter the sample chamber. It affects only 20 cm optical path out of the total of about 400 cm. Moreover, the sample chamber is small, and has its own purging line as well. Therefore, its humidity can be reduced quickly. As a result, VCD-II can be maintained extremely dry, most often at 0 % reading of relative humidity on the LCD Digital Hygrometer (model 3309-50, Cole-Parmer Instrument Co.). Figure 36 is a VCD-II transmission

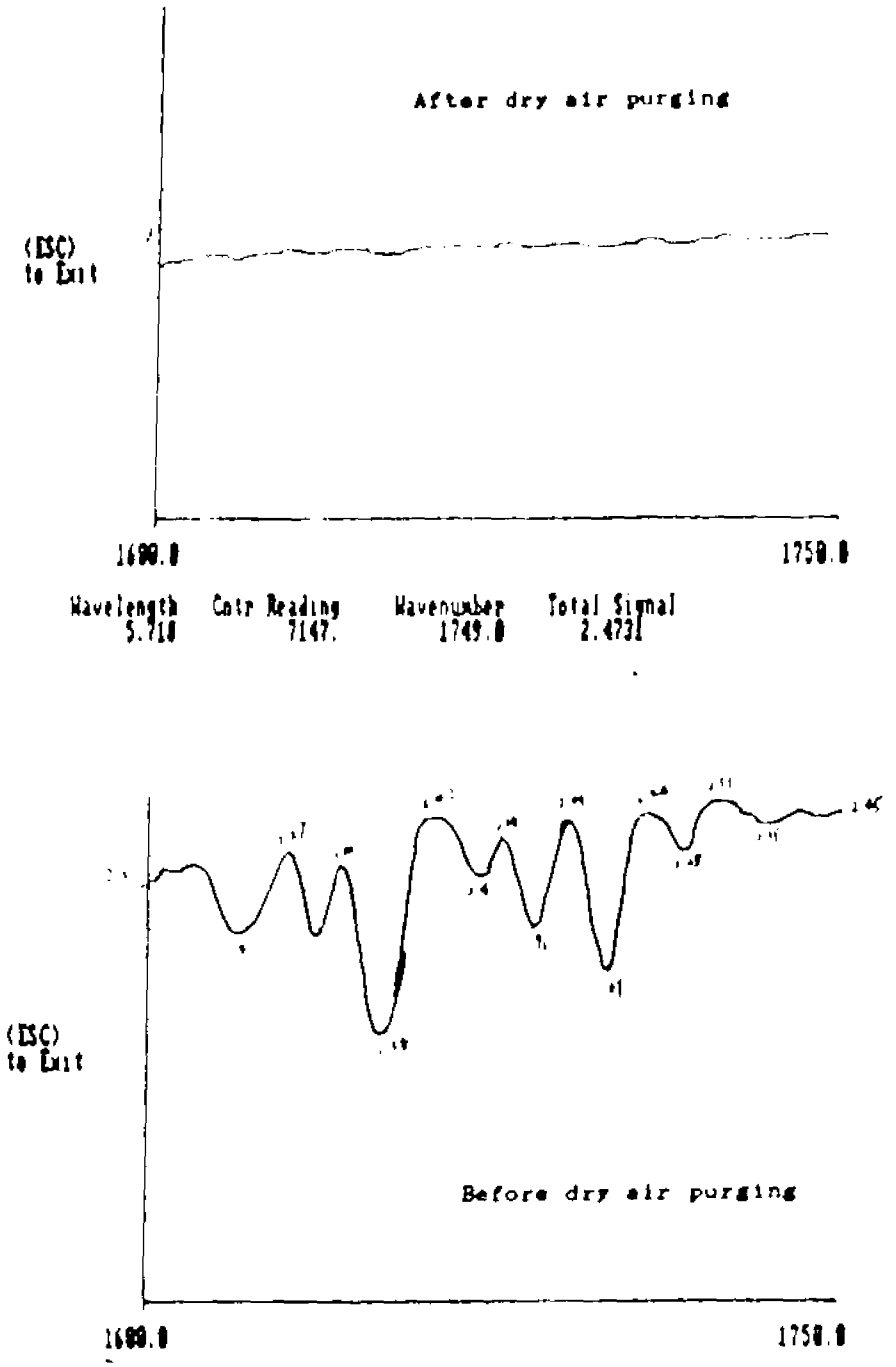

Figure 36. Transmission Spectrum of Air (instrument background) on VCD-II.

spectrum of air only, before and after the dry air purging. The flat line in the spectrum after the purging, free of H_2O absorption peaks, is the best illustration of the effectiveness of the dry air purging.

Finally, an improvement on VCD-I is worth mentioning. The source of poor signal-to-noise ratio in the amide I (6 μm) region for the VCD-I is principally due to the low response of the old detector, most sensitive at 12 μm. Substituting a new detector on VCD-I, with a maximum D^* of 5.11×10^{10} $cmHz^{\frac{1}{2}}W^{-1}$ in the 6-7 μm wavelength region, has lifted the VCD-I performance in the 1550 - 1750 cm^{-1} to a degree comparable to that of VCD-II. Figure 37 is a VCD spectrum of α-helical polylysine, collected by C. Farrell of our research group. It is the average of 12 scans. The sample was dissolved in basic D_2O at pD of 12.5 and concentration of 25 mg/ml. The CaF_2 cell pathlength was 50 μm. Its signal-to-noise ratio is roughly comparable to that obtained on VCD-II.

In summary, VCD-I is a broad band instrument, covering from 800 cm^{-1} to 1800 cm^{-1} with the original detector. However, with a new narrow-band detector, it yields a sensitivity similar to that of VCD-II. VCD-II is specially designed for the 6 μm region with a very high sensitivity with water vapor interfer-

ence. However, the detector respond drops sharply when scanning below 1600 cm^{-1}.

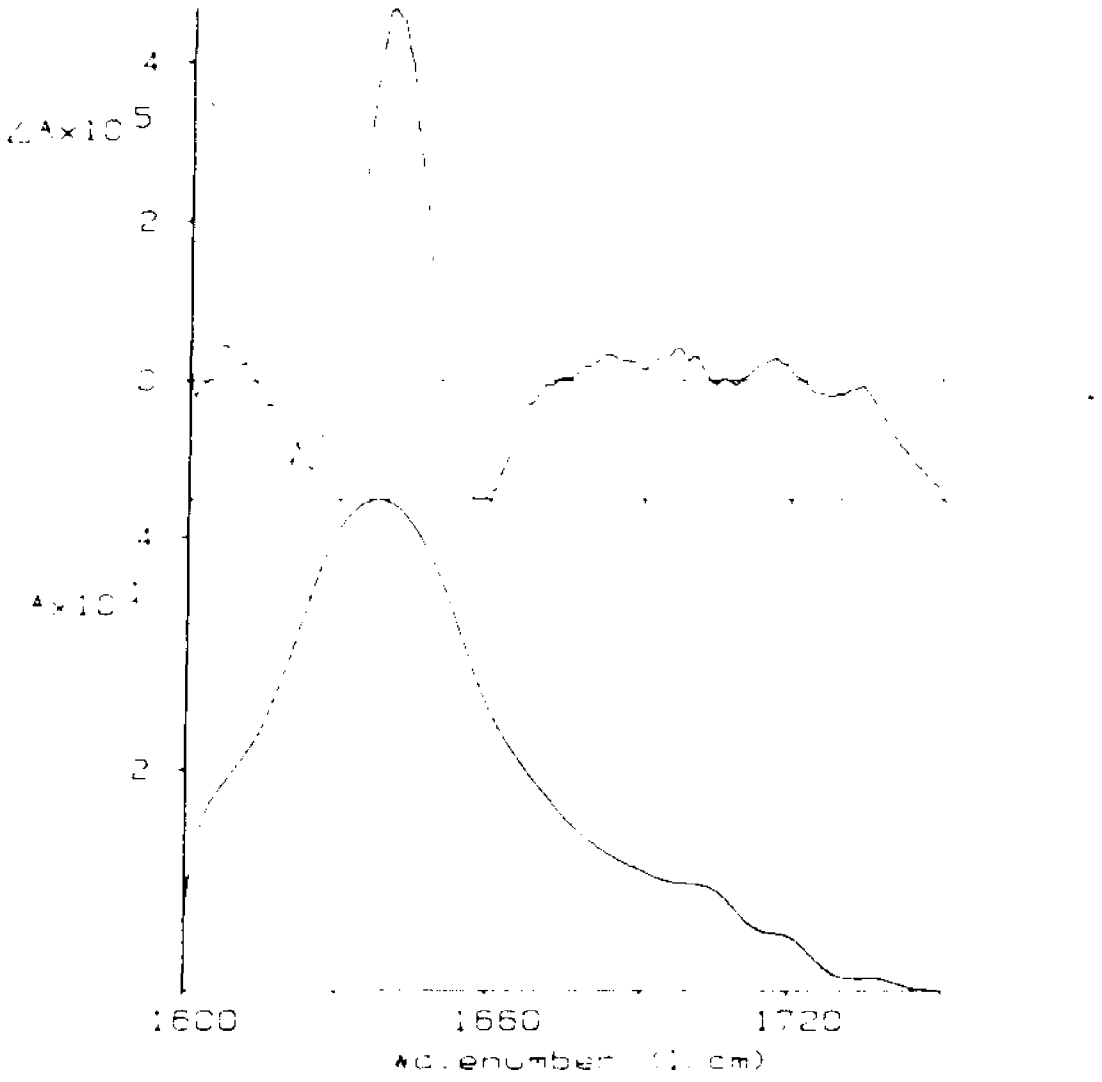

Figure 37. VCD Spectra of Poly-L-Lysine, in basic D_2O (pD ca. 12.5), 25 mg/ml, in 50 μm CaF_2 cell, 12 scans average, corrected by solvent VCD. Collected by Codelia Farrell on VCD-I with new detector.

Chapter Five

Results and Discussions

In this chapter, the discussion will center around the interpretations of two sets of data: i) alanyl-alanine in the amide III region; and ii) alanyl-alanyl-alanine in the amide I' region. Those investigations exemplify the applications of infrared vibrational circular dichroism, particularly in the conformational studies of biologically significant molecules in aqueous solution phase.

5.1. Vibrational Circular Dichroism of Alanyl Dipeptide in the Amide III Spectral Region[22]

Before Diem *et al.* published the first VCD result in the amide III vibration region in 1988[22], there had been several reports of VCD observations in regions of the amide A, amide I and amide II vibrations of the peptide linkages[63-70]. Those VCD results, particularly those in the amide I region, had demonstrated the conformational sensitivity of

VCD. Furthermore, it had been shown that the information derived from VCD complements that obtained from the electronic CD[67].

The structural sensitivity of VCD originates from the coupling of vibrational motions that are a few bonds apart, and the coupling happens at the time scale of molecular vibrations. Yet, in most of those early investigations, the peptides were studied in nonaqueous media. It is understandable that several earlier groups mostly shied away from water as the solvent because of its enormous absorption in the mid-infrared region. Still, Diem's group took on the challenge, worked with samples in aqueous solution in the mid-IR region extensively and has been proving that VCD is a novel probe of stereochemical sensitivity for molecules in water. These studies in aqueous solution will have a special implication for molecules of biological significance.

The frequency shift of the amide III vibration of peptides in 1250 - 1350 cm^{-1} region exhibits qualitative peptides conformational sensitivity, and consequently has been used to complement crystallographic and electronic CD information[71]. Thus, the significance of amide III VCD measurement lies in the possibility of further exploring the secondary struc-

ture of peptides. However, the amide III vibration is far less defined in terms of atomic displacements than other amide vibrations of the peptide linkage, such as amide A (mostly N-H stretching) or amide I (mostly C=O stretching) modes. Moreover, deuteration of a peptide changes the composition of the amide III vibration significantly. Therefore, only data taken in H_2O solution contain the original amide III vibration, while data obtained in D_2O do not. This is true mostly because the N-H deformation coordinate couples with the C_{α}-H deformation coordinates, whereas the N-D does not.

To test the feasibility of observing VCD in the amide III region in aqueous solution, one of the simplest chiral dipeptides, alanyl-alanine (*cf.* Figure 38 for the structure of L-alanyl-L-alanine, hereafter, abbreviated as L-L), was examined. One other reason for choosing this molecule is the extensive work and knowledge Diem's research group had acquired on the alanyl dipeptides via vibrational spectroscopic studies[58,62]. The molecule, therefore, fits well in the overall scope of an on-going research project. The study includes all four diastereomer forms (*i.e.*, L-L, L-D, D-L, D-D) to test the sensitivity of the VCD signal toward changes in the stereochemical structure.

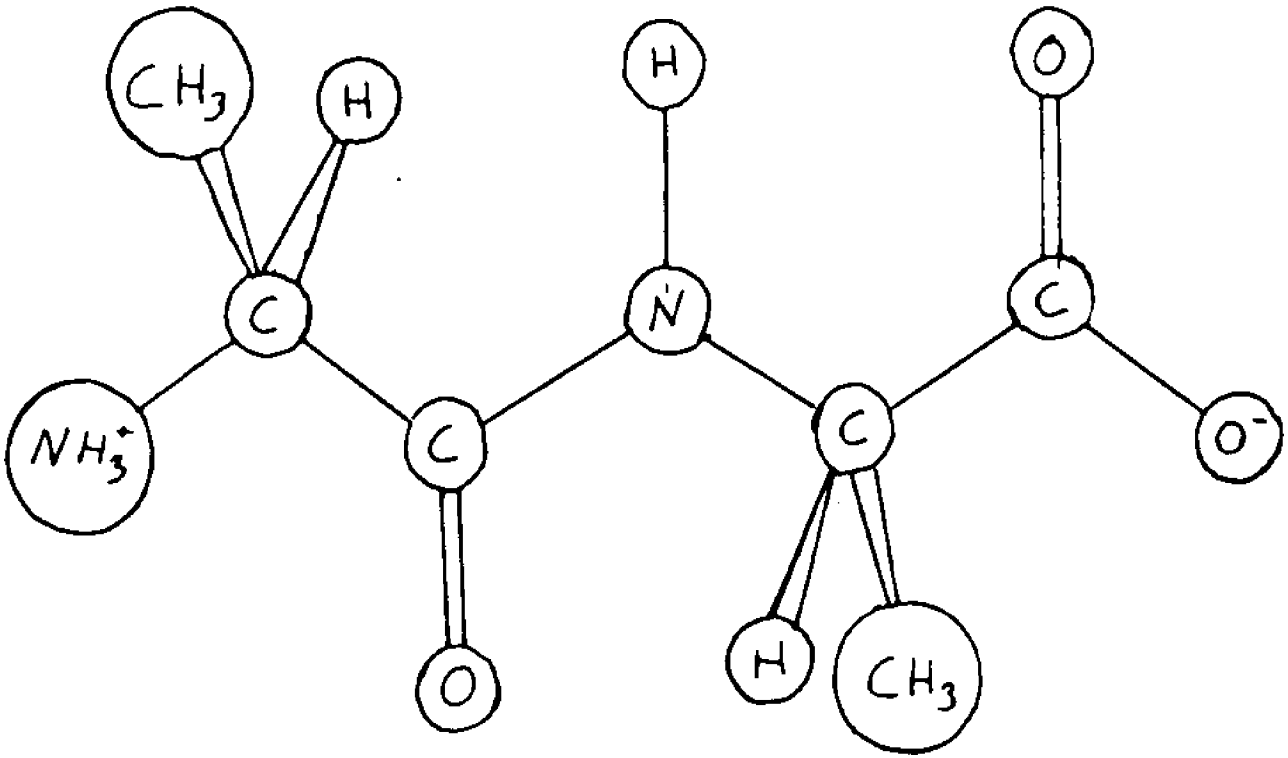

Figure 38. Structure of L-alanyl-L-alanine, L-L

A previous study[58,62], investigating the vibrations of various diastereomeric and isotopically substituted alanyl dipeptides in the 1200 - 1800 cm^{-1} region, led to a detailed assignment of the vibrations in the amide III spectral region. The study concluded that the amide III region contains primarily the methine deformation modes at the chiral carbon atoms and the in-plane deformation of N-H in the peptide linkage. The methines include one at the amine terminal residue, C_{α}^{N}-H, and another one at the carboxylic acid terminal residue, C_{α}^{C}-H. The finding of this extensive coupling between those vibrations resulted in a postulation of delocalized C_{α}-H/N-H deformation coordinates to describe the coupling. One of the resulting delocalized coordinates at 1280 cm^{-1} is commonly referred as the (old) "amide III" mode. The new assignment disagrees with the previous assignment[72], which assumed a coupling between the N-H in-plane deformation and the C-N stretching motion, but agrees with the normal coordinate calculations on small alanyl oligomers[73]. It also agrees with the normal coordinate calculations for alanyl-alanine [74]. The VCD results in the amide III region substantiate the earlier conclusion regarding the coupling of C_{α}-H/N-H coordinates and open a possibility of utilizing the amide III VCD as a new tool in

studying the peptide conformation.

Before discussing the VCD results of the alanyl dipeptides, it is appropriate to first briefly review the vibrations in the 1200-1700 cm^{-1} spectral region of alanine and alanyl-alanine. Table V is the summary of the vibrations of L-alanine. The data are taken from references 75 and 76, and Figure 25 in Chapter Four. The two vibrations at 1307 and 1355 cm^{-1} are assigned to two C_{α}-H deformations, which are degenerate in a symmetric molecule such as $CHCl_3$. In alanine, the asymmetric environment of the chiral center perturbs the degeneracy. These vibrations disappear upon deuteriation of the C_{α}-H. These deformation vibrations exhibit opposite sign in its VCD spectra (*cf.* Figure 25 in Chapter Four), as expected from two states that were degenerate originally but now have been perturbed and split. The other vibrations of alanine at 1379, 1409 and 1462 cm^{-1} are the methyl symmetric deformation, the symmetric stretching of carboxylic anion, and the methyl antisymmetric deformation modes, respectively[75]. The methyl deformation modes show no detectable VCD intensity[76]. (*cf.* Figure 25)

Table VI summarizes the vibration assignments of alanyl dipeptides in the 1200 - 1700 cm^{-1} region,

Table V

Vibrational Frequencies, Assignments, and VCD Intensities of L-alanine in Aqueous Solution in the 1200 - 1700 cm^{-1} Region

frequency[a] cm^{-1}	IR intensity[b] A	VCD intensity[b] $\Delta A \times 10^5$	assignment[c]
1307	0.14	5.3	$\delta(C_\alpha\text{-}H)$
1355	0.15	-5.5	$\delta(C_\alpha\text{-}H)$
1379	0.10		$\delta^s(CH_3)$
1409	0.23	1.8	$\nu^s(CO_2^-)$
1462	0.10		$\delta^{as}(CH_3)$
1590			$\nu^{as}(CO_2^-)$

a. The frequencies are taken from ref.75.
b. Infrared absorption and VCD intensities are presented in absorbance, rather than extinction units, due to uncertainty of the uncalibrated path length (about 15 μm, C = 1 M in H_2O).
c. Symbols used: δ, deformation; ν, stretch; s, symmetric; as, antisymmetric.

Table VI

Vibrational Frequencies, Assignments, and VCD Intensities of alanyl-alanine in Aqueous Solution in 1200-1700 cm^{-1} Region

frequency[a] cm^{-1}	IR intensity[b] A	VCD intensity[b] $\Delta A \times 10^5$	assignment
	L-alanyl-L-alanine		
1280	0.15	1.8	c
1325	0.06	-0.7	c
1340			c
1372	0.2		$\delta^s(CH_3)$
1407	0.34		$\nu^s(CO_2^-)$
1460	0.2		$\delta^{as}(CH_3)$
1590[d]	0.65	-0.5	$\nu^{as}(CO_2^-)$
1665[d]	0.45		amide I'
	L-alanyl-D-alanine		
1280	0.15	-1.3	c
1325	0.05		c
1340	0.03	0.4	c
1372	0.2		$\delta^s(CH_3)$
1407	0.34		$\nu^s(CO_2^-)$
1460	0.19		$\delta^{as}(CH_3)$
1590[d]	0.65	-0.5	$\nu^{as}(CO_2^-)$
1665[d]	0.45		amide I'

a. The frequencies are taken from ref.75.
b. *cf.* comment b of Table Five; C=1M, pathlength 15 μm.
c. Coupled C_α^N-H/N-H/C_α^C-H deformation; *cf.* text.
d. D_2O data; C = 0.5 M, about 15 μm path length.

based on the Raman data of six isotopically substituted dipeptides. In D_2O, the amide I' band is about 1670 cm^{-1} and the antisymmetric stretching mode of carboxylic anion is at 1590 cm^{-1} (*cf.* Figure 39,40, 41).

For a better clarity, the VCD and IR absorption spectra of L-alanyl-L-alanine (solid) are plotted against the spectra of L-alanyl-D-alanine (dash). The respective concentration for each sample was 0.5 M in H_2O in Figure 39 (1250-1490 cm^{-1}), 1.0 M in D_2O in Figure 40 (1250 -1450 cm^{-1}), and 0.5 M in D_2O in Figure 41 (1450- 1750 cm^{-1}).

The symmetric CO_2^- stretching (1407 cm^{-1}), the antisymmetric methyl deformation (1460 cm^{-1}), and the symmetric methyl deformation (1372 cm^{-1}) vibrations occur nearly at the same wavenumbers as in alanine itself. The next group of vibrations toward the lower wavenumber are the methine (C_α-H) and the N-H in-plane deformation modes. In the alanyl-alanine, one expects to observe four C_α-H deformation vibrations, two from the $C_\alpha{}^C$-H and two from the $C_\alpha{}^N$-H. Indeed, all four vibrations turn up at 1276 and 1329 cm^{-1} for the $C_\alpha{}^C$-H deformations, and 1305 and 1355 cm^{-1} for the $C_\alpha{}^N$-H deformations, in Raman[62] as well as in infrared spectroscopies (*cf.* Figure 40). The minor shift

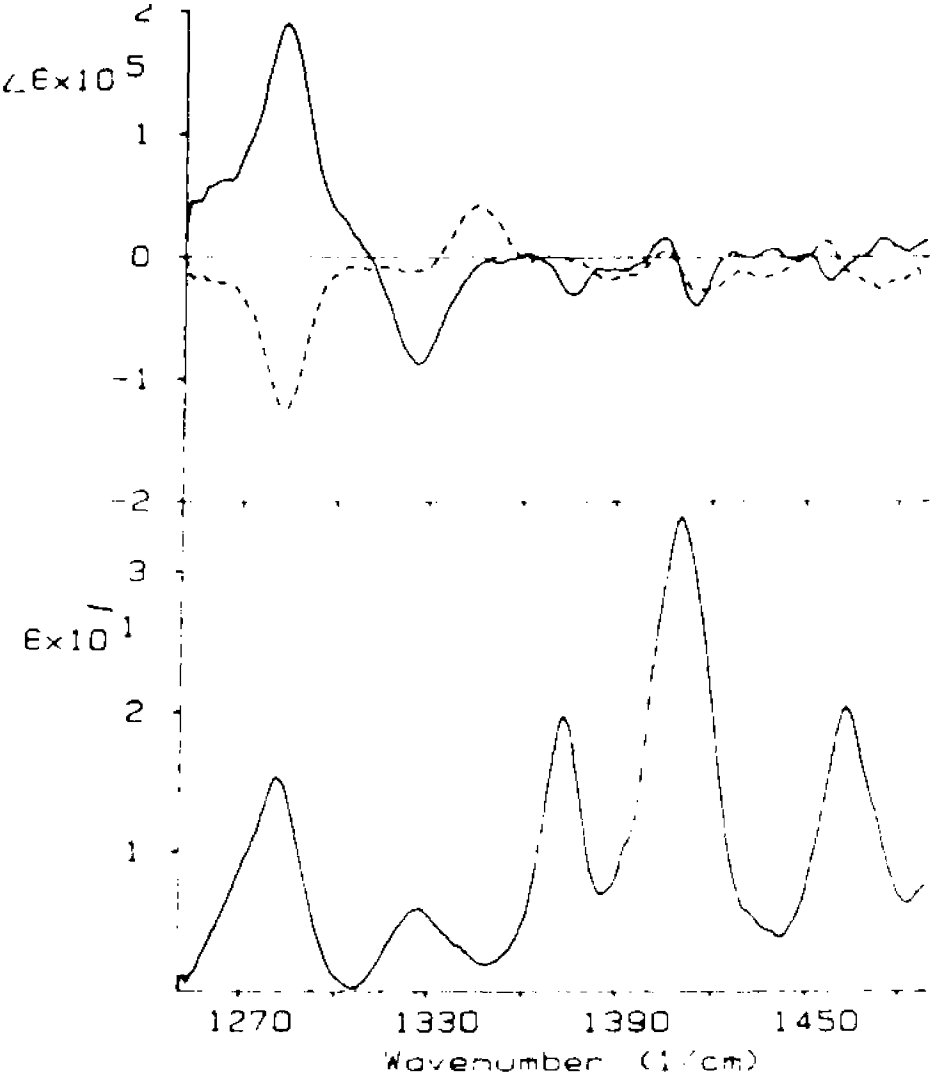

Figure 39. Spectra of L-L (solid) and L-D (dash) in H_2O, both C = 0.5 M; top: VCD; bottom: IR.

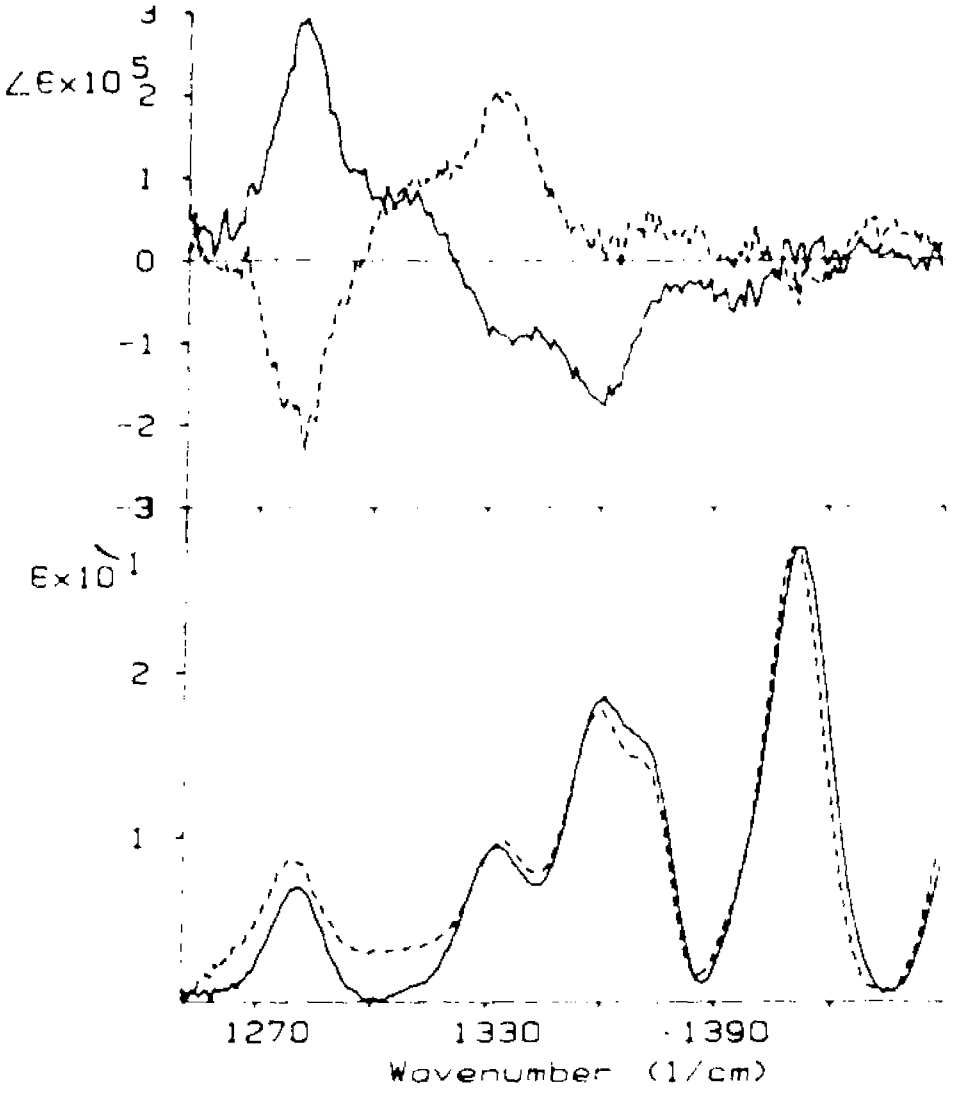

Figure 40. Spectra of L-L (solid) and L-D (dash) in D_2O, both C = 1.0 M; top: VCD; bottom: IR.

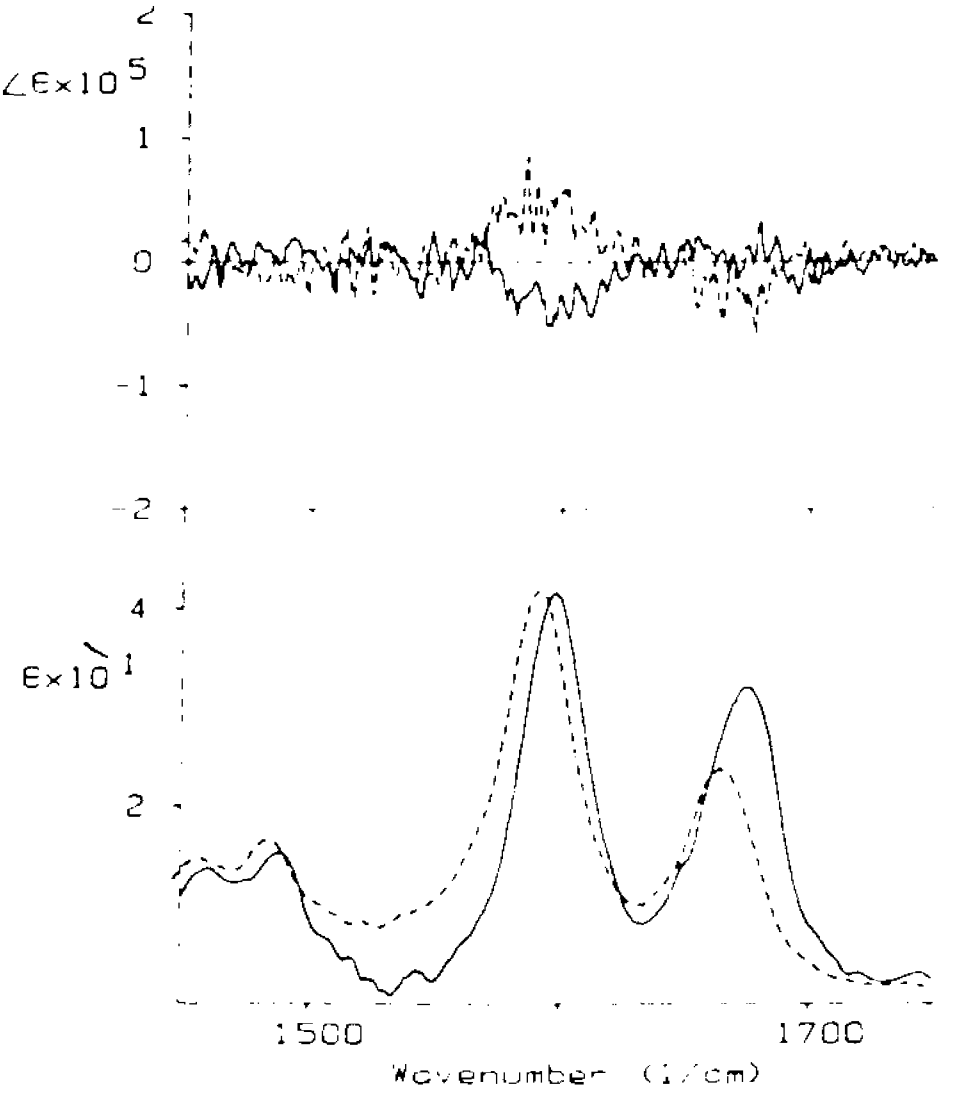

Figure 41. Spectra of L-L (solid) and L-D (dash) in D_2O, both C = 0.5 M; top: VCD; bottom: IR.

toward lower wavenumber of the $C_\alpha{}^C$-H vibrations in D_2O solution from those in H_2O is expected because of the isotopic substitution at the nitrogen atom (including the NH_3^+)[75].

The spectrum of L-alanyl-L-alanine in H_2O for the amide III region (*cf.* Figure 39, bottom) is markedly different from the one in D_2O[25,58,62]. It is neither similar to that of L-alanine, nor resembles a simple addition of the C_α-H and N-H deformations. Detailed isotopic studies revealed that the original N-H in-plane deformation, at 1336 cm^{-1}[62], mixes heavily with two of the four C_α-H deformations. Thus, the strong and unsymmetrically looking band at *ca.* 1280 cm^{-1}, which had previously been assigned to the amide III vibration, is a superposition of one original $C_\alpha{}^C$-H deformation at 1266 cm^{-1}, one highly coupled vibration at 1281 cm^{-1}, and one uncoupled $C_\alpha{}^N$-H deformation at 1305 cm^{-1}. The highly coupled band at 1281 cm^{-1} is one of the resulting vibrations by the three coupling coordinates, the N-H (1336 cm^{-1}), one of $C_\alpha{}^C$-H (1329 cm^{-1}) and one of $C_\alpha{}^N$-H (1355 cm^{-1}) deformations coordinates. The assignments of the two bands occurring at 1325 and 1340 cm^{-1}, in both Raman and infrared, are the remaining two linear combinations of the aforementioned three coupling coordinates.

These two vibrations show distinct frequency

and intensity differences between the L-L and D-L diastereomers in Raman and infrared spectra (*cf.* Figure 39, bottom). The differences are attributed to the different coupling between these interacting coordinates caused by the geometric dissimilarity. Thus, the VCD spectra of these vibrations are of particular interest since such coupling should disclose itself in distinct VCD features.

The VCD spectral results support the above postulate not only by a perfect agreement in the three wavenumbers, but also by a further distinction in the corresponding intensities, which clearly demonstrate the unique sensitivity of VCD towards the diastereomers. The distinction is far better than the IR absorption or Raman spectroscopy in this region. Figure 39 are the VCD and corresponding infrared spectra of L-L and L-D. The two VCD spectra can be considered as representing all four diastereomers since the VCD spectra of D-D and D-L are just the mirror images of those of L-L and L-D, respectively. Looking at the predominant VCD feature of L-alanyl-L-alanine under the composite peak at 1280 cm^{-1}, it is obvious that the VCD is particularly sensitive to the chirality of the acid terminal alanine residue because of the VCD signs change between L-L and L-D.

The distinct negative VCD peak at 1325 cm^{-1} in the L-L spectrum coincides with the aforementioned C_{α}^{N}-H/N-H/C_{α}^{C}-H coupling coordinates, while a positive band in the L-D VCD spectrum coincides with the third peak (1340 cm^{-1}) of the coupling coordinates. Interestingly, only one of the two vibrations at 1325/1340 cm^{-1} shows VCD in each of the diastereomers and the signs of their VCD signals are opposite.

These mismatch and the sign switching at 1280 cm^{-1} indicate a close relationship among those three peaks, thus, confirming the coupling between the N-H in-plane deformation and C_{α}-H deformations. Removal of N-H (deuterated to N-D) destroys this coupling as will be discussed in the next paragraph. The VCD intensity at 1280 cm^{-1} is attributed to the coupled C_{α}^{N}-H/N-H/C_{α}^{C}-H coordinate, and not to the uncoupled C_{α}^{C}-H deformation at 1266 cm^{-1} since the VCD peak at 1280 cm^{-1} looks perfectly symmetric and indicates no lower frequency component in it. A simple coupled oscillator interpretation, involving three near-degenerate coordinates, produce a useful simulated spectrum. However, a quantitative interpretation will require a normal coordinate analysis, which has been done recently by G. Roberts[74], as well as an intensity model calculation.

For the alanyl dipeptides in D_2O, the peak at

1276 cm^{-1} maintained distinctly in the VCD spectra, while the corresponding IR peak almost fainted into baseline. This is a clear evidence that the N-H in-plane deformation accounts the most for the amide III IR absorption at 1280 cm^{-1}, while its contribution to the VCD intensity is relatively small. Upon deuteration of the N-H, the clear pattern alteration in the VCD spectrum of L-L in the whole 1200 - 1500 cm^{-1} region, not just the peak at 1280 cm^{-1}, is yet another proof of a heavy mixing by the N-H deformation with the C_α-H deformations in H_2O to form the amide III bands. The N-H acts as a bridge, linking the $C_\alpha{}^N$-H and the $C_\alpha{}^C$-H. The disappearance of the coupling upon deuteration of N-H also gives a measure on how close the transitions are in order for the vibrational coupling to occur.

The VCD spectra in the amide III region of the alanyl dipeptides in D_2O have, once again, demonstrated the sensitivity of this technique towards the diastereomers (*cf.* Figure 41). Any of the four diastereomers is easily distinguishable from its VCD spectrum.

None of the other vibrations in the 1250-1750 cm^{-1} spectral region exhibit any significant differential (VCD) intensities. The most intense feature

observed outside the amide III region is the antisymmetric $-CO_2^-$ stretching mode at *ca.* 1590 cm^{-1}. Its VCD intensity is very small ($\Delta A(\tilde{\nu})/A(\tilde{\nu})$ *ca.* 10^{-5}, about the detection limit of VCD-I). The VCD sign of this vibration is, as expected, determined by the chirality of the acid terminal alanine residue; that is, the L-L and D-L diastereomer exhibit the same VCD sign in this band. Figure 39 presents the VCD spectra of L-L and L-D species for a better clarity. Neither the methyl deformations at 1379 and 1462 cm^{-1}, nor the amide II at 1409 cm^{-1} shows any significant VCD intensity.

It appears that all peptide VCD signals are due to either of two mechanisms. In the C-H stretching region, all large signals have been due to the methine (C_α-H) stretching vibration, during which a sizable charge redistribution induces VCD intensity [7]. The other mechanism contributing to the previously observed VCD signals of peptide is of coupling by two or more identical or near identical transitions in a polymeric molecule. This mechanism is responsible for all the amide A, amide I and amide II VCD signals in the peptides studied by Nafie and Keiderling[63-70]. They noted that the amide I VCD signals nearly disappear as the peptide size goes down to four amino acids, believing that the coupling

of the transitions also diminishes.

Thus, the chiral perturbation of a symmetric vibrational chromophore (such as CH_3, CO_2^-) is too small to produce any significant VCD intensity, and most observed VCD is due to the charge-redistribution mechanism or the coupled oscillator mechanism. In the latter case, the coupling may be between identical groups, or energetically similar vibrations, within a close proximity in a polymeric unit, such as the N-H/C_α-H deformations described earlier.

To conclude this section, the observation of the VCD signals in the amide III region of peptides in aqueous solution is not only possible but also meaningful. The amide III vibration is a result of coupling by the N-H in-plane deformation and the adjacent C_α-H deformations on both sides of the N-H along the peptide backbone. This interpretation is far more complicated than that of other more localized amide vibrations, and consequently more amenable to an assignment based on group frequencies. Furthermore, the VCD of localized vibrations (*e.g.*, the amide I) can be interpreted in terms of a simple coupled oscillator model (*cf.* the next section), whereas the VCD signals in the amide III region require a detailed normal coordinate analysis and VCD intensity

calculations for a qualitative interpretation. Nevertheless, the amide III spectral region contains a significant amount of structural information, as evidenced by the comparison of the VCD spectra of diastereomers of alanyl dipeptide. In addition, the sensitivity of VCD toward all diastereomers in the amide III region may well be utilized as an analytical tool in a biochemical and pharmaceutical analysis.

5.2 Vibrational Circular Dichroism Study of Alanyl Tripeptide[21]

This section will further demonstrate the sensitive nature of VCD method towards the secondary structure of a molecule in solution via the studies in the amide I' region of L-alanyl-L-alanyl-L-alanine (*cf.* Figure 42 for molecular structure). The detailed interpretation process provides a classical example of the mutual relationship between the theoretical modeling and the experimentation.

The sensitivity of VCD signals towards the secondary structure originates from the coupling of two or more identical, or virtually identical, achiral transitions of the peptide linkages arranged in a dissymmetric pattern, such as an α-helix. The optical activity of such dissymmetric structures has been investigated theoretically in detail, both in electronic[26] and vibrational[16,19,77] optical activity.

In the simplest example of dissymmetric vibrational interaction - the coupled oscillator model (*cf.* Chapter One) - two identical achiral groups interact and form the symmetric and antisymmetric coupled excited states |+> and |->, respectively. The interaction, in most cases, is a straightforward dipole-dipole coupling. The splitting between the |+> and

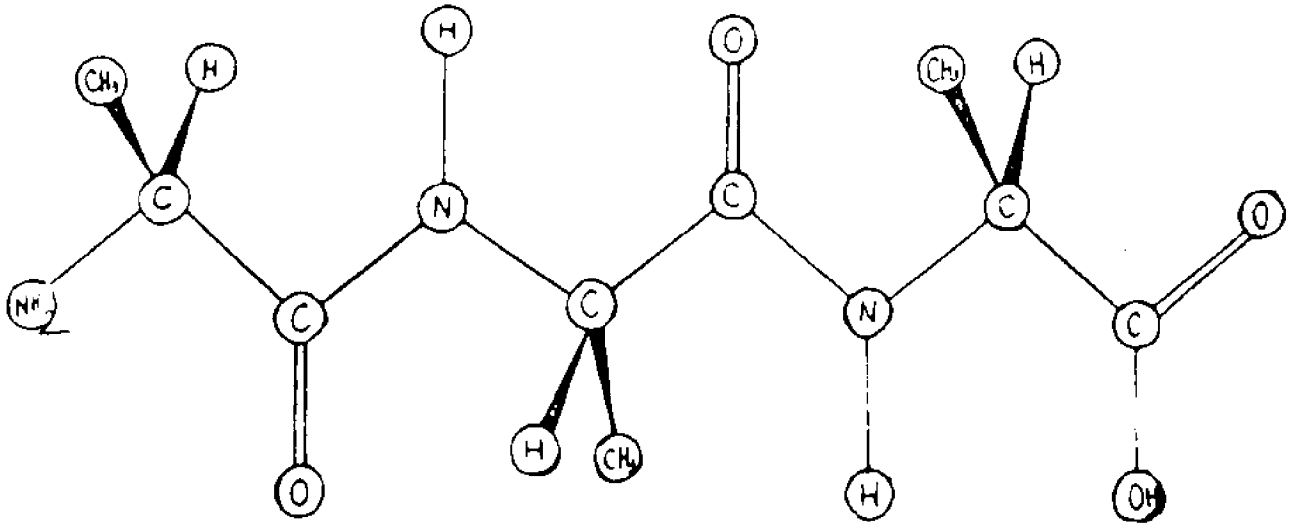

Figure 42. Molecular Structure of L-Alanyl-L-Alanyl-L-Alanine, L-L-L

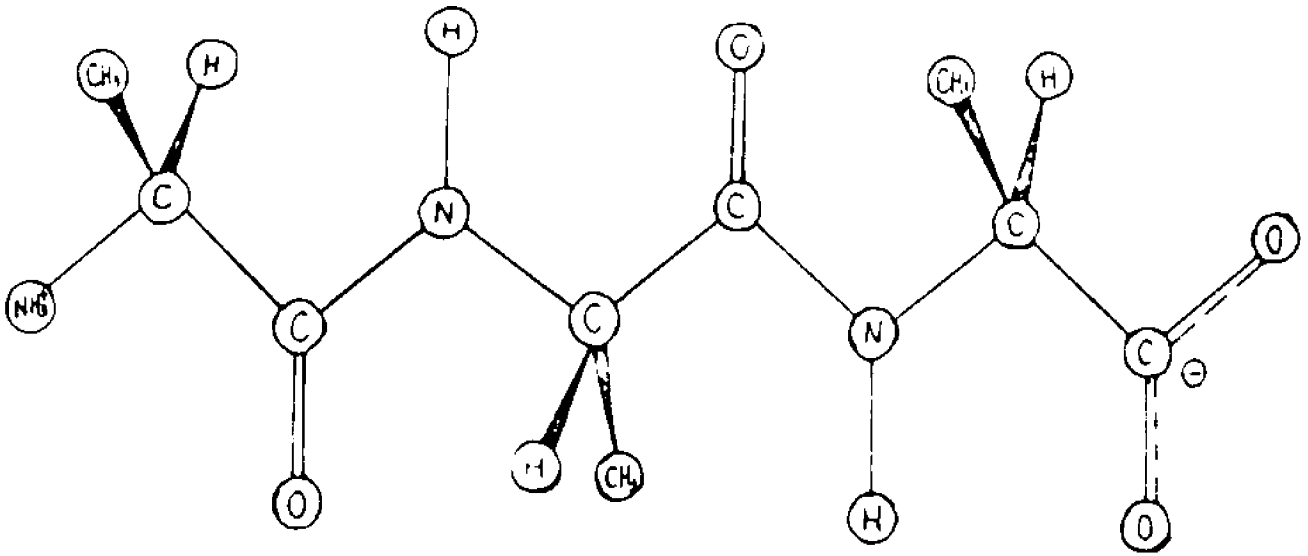

Figure 43. Zwitterionic Structure of L-Alanyl-L-Alanyl-L-Alanine

the |-> states can amount from a few to about a hundred wavenumbers, depending on the dipole strength, the geometry, and the distance between the oscillators.

In practice, the observed splitting most often is less than the band width of the vibrational transitions since most samples investigated are in solution phase. Frequent molecular collisions in solution phase broaden the band shape of a molecular transition. As a result, the transitions from the ground state into the |+> and |-> excited states form only one broadened and distorted infrared absorption band instead of two distinct peaks. The corresponding VCD spectrum, however, show distinct positive-negative (or negative-positive) band shapes, as predicted by the coupled oscillator theory. The |+> and |-> transitions exhibit opposite signs in circular dichroism.

Unlike alanyl dipeptides[22] (*cf.* Figure 41), the VCD spectrum of L-alanyl-L-alanyl-L-alanine in a neutral D_2O solution displays a distinct negative-positive intensity pattern in the amide I' region (*cf.* Figure 44). Such pattern should be interpreted as an evidence of a stable coupled oscillator, at least on the time scale of 10^{-12}-10^{-15} second, thus, indicating the existence of a preferred solution conformation.

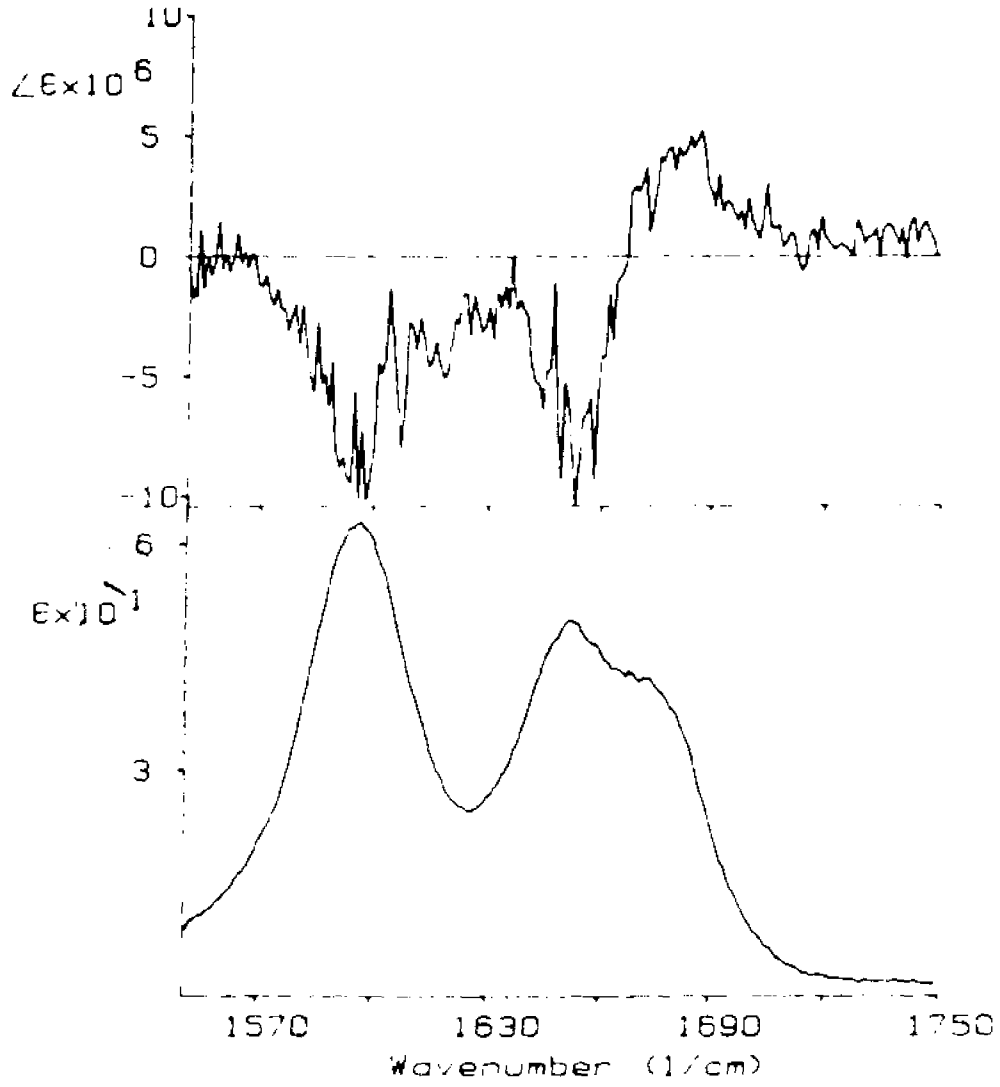

Figure 44. Spectra of L-L-L in D_2O, C=0.49 M; top: VCD; bottom: IR. (part of Fig.32)

To support this interpretation, other experiment results are also presented. No coupling features are observed for either L-alanyl-L-alanyl-L-alanine in a basic D_2O solution, or N-acetyl-L-alanyl-N'-methyl-amide (AAMA, *cf.* Figure 45 for structure) in a neutral D_2O solution. Both these cases lack the zwitterionic features. Thus, one can conclude that without the zwitterionic interaction no stable solution conformer exits that can support a coupled oscillator.

The samples, L-alanyl-L-alanyl-L-alanine and D-alanyl-D-alanyl-D-alanine (Chemical Dynamics, Inc.), are deuterated (dissolved in excess D_2O and consequently lyophilized from D_2O) and redissolved in D_2O of a precisely calculated volume to make a 0.5 M solution. The basic solution is prepared by titrating the neutral solution with concentrated NaOD solution until the pD of the sample solution reaches approximately 13. The sample concentration is recalculated accordingly. A fixed path cell is used with CaF_2 windows and a 15 μm teflon spacer. AAMA (Chemical Dynamics, Inc.) sample is run at the same conditions. The solution phase Raman spectra are obtained with a 500 mW laser excitation power at 514.5 nm on a completely digital Raman spectrometer described elsewhere[78]. The coupled oscillator calculations were

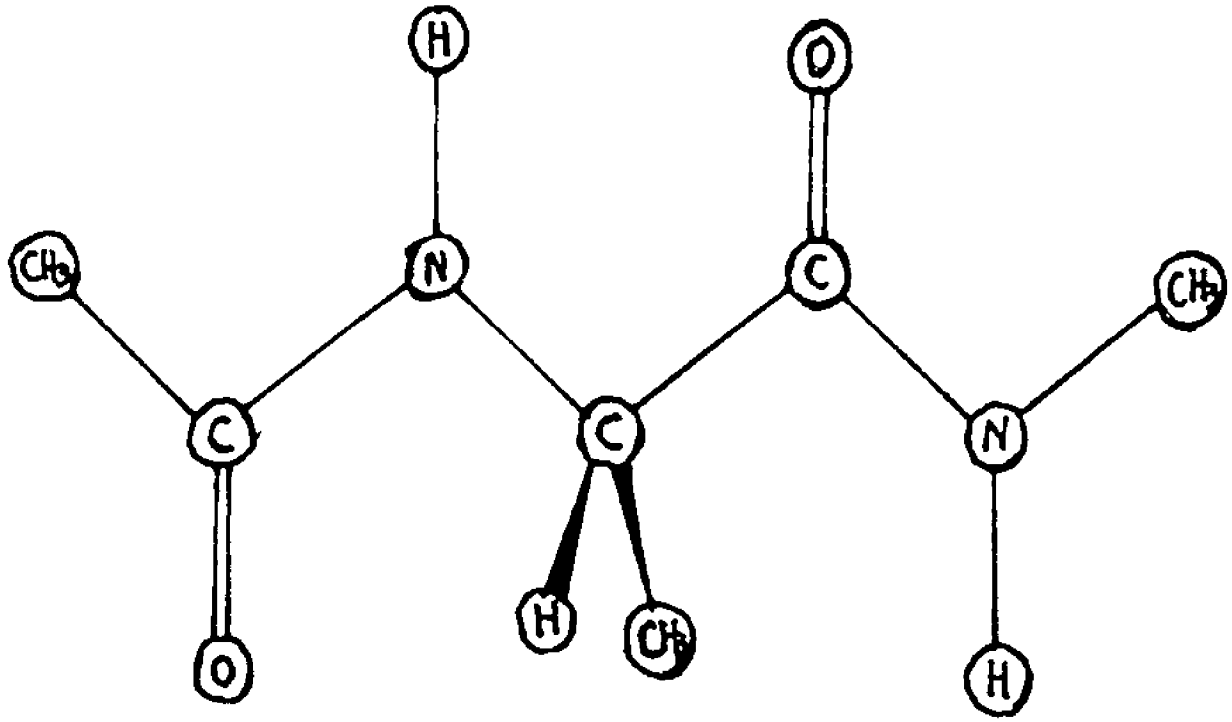

Figure 45. Structure of N-acetyl-L-alanyl-N'-methyl-amide, AAMA

carried out using the principles and formulae described in Chapter One. The μ_1 and μ_2 are the dipole strength of a single amide I' transition, obtained from the IR absorption spectrum of alanyl dipeptide, which contains a single peptide linkage, by the approximation[79] (for Lorentzian peaks):

$$\mu = \int_{\bar{\nu}}^{\epsilon(\bar{\nu})} d\bar{\nu} = 0.92 \times 10^{-38} \; \epsilon_{max} W \sqrt{\bar{\nu}_0} \qquad (5.1)$$

in esu cm erg. Here W denotes the half-width at the half-height of the observed band.

The aim of the coupled oscillator calculations is to utilize the observed rotational and dipole strengths, as well as the dipolar splitting, to find a molecular conformation that reproduces the experimental parameters. The program performing these calculations was written by M. Diem in FORTRAN 77 for operation on a personal computer. The molecular structure of the peptide is input in equilibrium bond lengths and angles. Starting from the fully extended form, $\phi = 180^\circ$ and $\psi = 180^\circ$, rotations about the torsion angles ϕ and ψ, respectively, in -5° steps cover the entire conformation space (ϕ and ψ: from 180° to -180°). For each conformation, T_{12}, V_{12}, R_+ D_+

and D_- are computed. The final step is searching the 72 x 72 conformational matrix for the best fit between the calculated and the experimentally observed data. Conformational energy computation were done on a MicroVAX computer (Digital Equipment Corporation), using MM2 and AMBER programs for the energy minimization.

Based on a comparison of the vibrational spectra of L-alanine, L-alanyl-L-alanine and L-alanyl-L-alanyl-L-alanine, it is reasonable to assume that L-alanyl-L-alanyl-L-alanine exists as a zwitterionic species in aqueous solution (*cf.* Figure 43). Alanine, with a pK_a of 2.3 and a pK_b of 9.9, is known to exist in aqueous solution nearly completely in the zwitterionic form. In its IR and Raman spectra[75], this is evident by the occurrence of two vibrations that are indicative of the $-CO_2^-$ anion: the symmetric carboxylate stretching mode (1409 cm^{-1}, strong in Raman) and the antisymmetric carboxylate stretching mode (1595 cm^{-1}, strong in IR).

These modes are observed virtually unchanged in L-alanyl-L-alanine[22] and L-alanyl-L-alanyl-L-alanine, thus confirming that all three species exits as zwitterions. Figure 44 shows the $-CO_2^-$ antisymmetric stretching mode at *ca.* 1595 cm^{-1}. The VCD intensity of this mode is roughly constant for L-alanine, L-ala-

nyl-L-alanine, L-alanyl-L-alanyl-L-alanine.

The higher frequency peaks shown in Figure 44 are the amide I′ modes. In L-alanyl-L-alanine (*cf.* Figure 41), there is a single peak at *ca.* 1673 cm^{-1}. In L-alanyl-L-alanyl-L-alanine, the amide I′ region appears to have two distinct yet not completely separated peaks at 1650 and 1675 cm^{-1}. The higher wavenumber component (1675 cm^{-1}) is more intense and more highly polarized in the Raman spectra (*cf.* Figure 46), indicating that it is the |+> state, the symmetric combination.

At the amide I′ vibration of L-alanyl-L-alanine, not much VCD intensity is observed (*cf.* Figure 29). However,at the same vibration L-alanyl-L-alanyl-L-alanine, a distinct negative-positive couplet (proceeding from the lower to the higher wavenumber) occurs. The occurrence of this VCD couplet, along with the observation of two corresponding peaks in the both IR and Raman spectra, strongly suggests that coupling between the amide I′ vibrations is taking place and that the observed features are attributable to the coupled oscillator mechanism.

The exact wavenumbers of the absorption and the VCD peaks are determined through a decomposition of the overlapping peaks into Lorentzian components. The

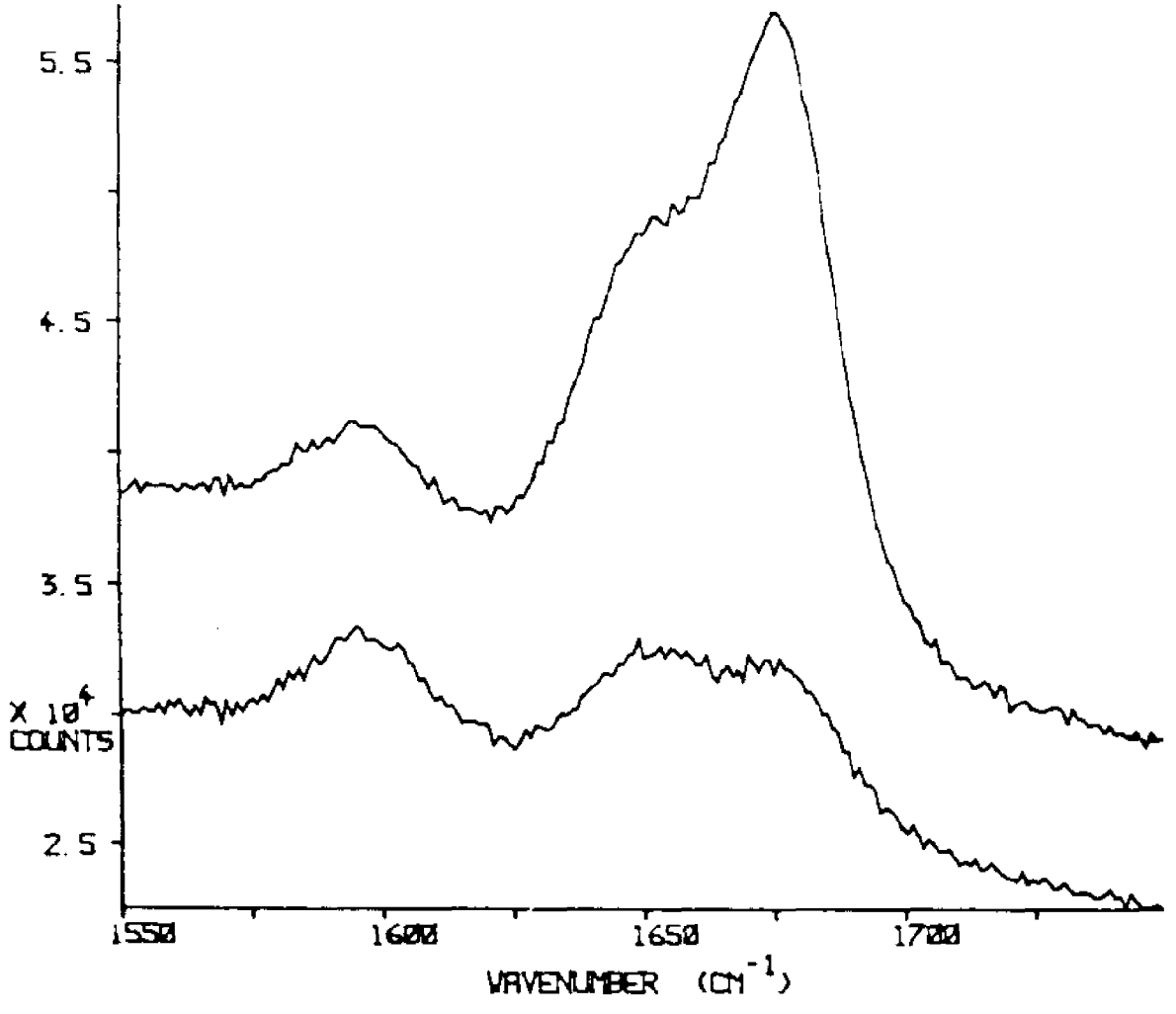

Figure 46. Raman Spectra of L-L-L, in neutral D_2O; C = 0.49 M, 30 scans each; upper: polarized; lower: depolarized.

decomposition of the VCD spectrum is also useful in estimating any signal cancellation in the negative-positive couplet. Basing on the splitting and bandwidths obtained from the absorption spectrum in Figure 44, the cancellation of the VCD intensities is small. The observed frequencies, and dipole and rotational strengths are summarized in Table VII.

Two possible explanations for the observed spectral features are worthy of discussion, considering two entirely different scenarios. First, a model is built on the following interpretations: i) the two amide I' peaks observed in the vibrational, spectra *i.e.*, infrared and Raman, and the VCD spectra were due to two completely unrelated conformations; ii) each conformer contributed with a monosignate VCD signal in the vibrational spectra and the corresponding VCD spectrum; and iii) the two mono-signate VCD signals, however, happened to have opposite signs. This model would fail to explain differences in the Raman depolarization ratios. In addition, the differences in the wavenumbers of the two amide I' frequencies would be surprisingly large in the absence of any coupling mechanism. Other spectral regions studied, notably the amide III vibrations, do not indicate the occurrence of two conformers with the opposite VCD.

Table VII

Observed Frequencies, and IR and VCD Intensities of L-alanyl-L-alanyl-L-alanine (0.5 M in D_2O)

frequency cm^{-1}	ϵ_{max} L/mol cm	$\Delta\epsilon_{max}$ L/mol cm	assignment
1595	815	-1.6×10^{-2}	$\nu^{AB}(CO_{2-})$
1650	513	-1.4×10^{-2}	amide I', $\bar{\nu}_-$
1675	394	1.3×10^{-2}	amide I', $\bar{\nu}_+$

Second, if the observed VCD is due to a coupled oscillator mechanism, the molecule must exist in one or more solution conformation that is stable on the vibrational time scale, and which exhibits certain VCD intensities. This condition can be satisfied by the occurrence of a distribution of many slightly different conformations with similar VCD features, or the predominance of one or a few structures that will dominate the VCD spectra. At present, it is impossible to distinguish these cases without concentration- and/or temperature-dependent studies of the VCD intensities.

Next, the discussion centers on the result from the coupled oscillator interpretation of the observed spectral features. The aim of this discussion is to compare the VCD intensities computed via the coupled oscillator model for the fragment (I) with the experimental VCD data, and deduce a conformation for this fragment. Finally, some other experimental evidences are also presented to justify the structure proposed in terms of a stabilizing interaction by the zwitterionic groups.

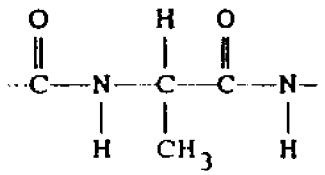

(I)

For each of the 5184 conformers (*vide supra*), R_+, V_{12}, and the ratio of D_+/D_- are calculated via the coupled oscillator model. The resulting matrix is searched for a suitable fit to the experimental data. In searching the calculated matrix in the conformation space, the following features have utmost significance. First. the sign and magnitude of V_{12}, which half of the splitting between the |+> and |-> states, have to be right. Second, the computed IR intensities distribution between these states (D_+/D_-) must be close to the observed values. Third, the signs and magnitudes of the rotational strengths ought to be reproduced.

Unfortunately (and surprisingly), none of the 5184 conformers give the desired optical parameters, namely $R_+ = 1 \times 10^{-42}$ esu^{2}cm^2, $V_{12} = 12.5$ cm^{-1}, and $D_+/D_- = 0.8$. In an attempt to improve the fit between observed the computed spectral parameters, the direction of the dipole transition was allowed to deviate slightly ($\pm 5^\circ$) from the direction of the C=O bond. Although this improved the fit somewhat, the overall agreement is still unsatisfactory.

When relaxing the fitting requirements to

$$1.0 \times 10^{-42} < R_+ < 2.5 \times 10^{-42} \text{ esu}^2\text{cm}^2 \quad (5.2)$$

$$8.0 < V_{12} < 12.5 \text{ cm}^{-1} \qquad (5.3)$$

and

$$0.5 < D_+/D_- < 2.5 \qquad (5.4)$$

a number of possibilities were found, with

$$\phi = 165 \pm 20^\circ \text{ and } \psi = -5 \pm 10^\circ$$

A typical set of computed spectral parameters for one of these conformers are summarized in Table VIII.

Although these structures reproduced the observed spectral data reasonably well, they have to be discarded as possible conformations since they include such a twist of the fragment that the two amide hydrogen atoms come within the van der Waals radii.

Thus, the results of the first search over the conformation space of the peptide backbone fragment do not yield any conformers which either generate acceptable molecular structures, or for which V_{12}, R_+, and D_+/D_- are in good agreement with the experimental data. Examining the calculation process closely, it appears that there exists an exclusion rule preventing all three parameters R_+, V_{12}, and D_+/D_- to converge toward the experimental results simultaneously. In particular, the required V_{12} value and the ratio D_+/D_- are incompatible: a large V_{12} almost invariably results in a very small or very large D_+/D_- ratio.

Table VIII

Comparison of
Observed and Calculated Coupled Oscillator
Frequencies, and Dipole and Rotational Strengths,
for Different Conformers

		Calculated	
	Observed	Form I $\phi=165^\circ$ $\psi=-5^\circ$	Form II $\phi=120^\circ$ $\psi=-25^\circ$
$\bar{\nu}_+(cm^{-1})$	1675	1671	1667
$\bar{\nu}_-(cm^{-1})$	1650	1654	1657
$D_+[\ 10^{-38}(esu^2cm^2)]$	10.3	15.5	12.8
$D_-[\ 10^{-38}(esu^2cm^2)]$	13.4	8.1	10.8
$R_+[\ 10^{-42}(esu^2cm^2)]$	0.84	1.9	3.8
$R_-[\ 10^{-42}(esu^2cm^2)]$	-0.91	-1.9	-3.8

This is understandable from a physical viewpoint: a good coupling geometry between μ_1 and μ_2 will occur when the two dipoles are either parallel or antiparallel. In these case, however, either D_+ or D_- will become predominant at the expense of the other transition.

Next, the attention is on looking for the reasons that may cause the discrepancy between experimental and calculated data. Both R and D depend, besides the geometric parameters, on the dipole strength. Mechanical coupling of the carbonyl vibrations can effect strongly the splitting of the |+> and |-> states, in addition to the dipolar coupling energy expressed in Equation (1.38) (V_{12} matrix in Chapter One). The relative magnitude of the dipolar vs. mechanical coupling has been discussed before[30]. Not including such mechanical coupling in the calculations seriously underestimates the splitting between the |+> and |-> states. That is, the observed splitting must be greater than the calculated one based on the current model. Furthermore, it is likely that the two C=O stretching frequencies are not exactly degenerate, since their chemical environments differ at the positively and negatively charged zwitterionic residue positions. As a result, there would also be an uncertainty here for the calculated

spectrum.

Thus, it is advantageous to search the conformations for a good fit for the observed dipole and rotational strengths, omitting the coupling energy as a requirement. In particular, emphasis is on the near equality of D_+ and D_-, while allowing V_{12} to be as low as 5 cm^{-1}.

This search yielded only a few conformers for which D_+ and D_- are about the same, and $R_+ > 0$. These conformers have ϕ and ψ values of 120 $\pm$ 5° and -25°, respectively. Their spectral parameters are tabulated also in Table VIII (Form II). However, the agreement between observed and calculated parameters is still not particularly good. As the ratio D_+/D_- approaches unity, the rotational strength becomes larger than the experimental value by about a factor of 3. This disagreement is, unfortunately, very large for the structures that are most likely.

The discrepancy in the rotational strengths may result from an underestimation of the VCD signal in the instrument and cancellation of signal strengths due to different conformers. Also, an absolute calibration of signal as small as VCD is difficult. There is a good agreement between the data collected on VCD-I and other existing VCD spectrometers[76].

However, the estimated deviation in the absolute magnitude between the different instruments may be as high as 30%, although the data are perfectly reproducible on the respective instruments. The occurrence of other structures with opposite VCD signal intensities could easily decrease the observed rotational strengths. However, it is impossible to quantify this aspect at present time.

The IR absorption and VCD spectra suggest strong interaction of the two amide I' transitions. The VCD spectral pattern suggests a left-handed helical structure, since the signal is a negative-positive couplet[30]. The calculated absorption intensities of a conformer with ϕ=120° and ψ=-25° (*cf.* Figure 47), called a "left-handed bridge conformer" [80], are similar to the observed ones, but with a smaller splitting between the excited states and with a larger rotational strengths. The smaller observed VCD intensities is not likely to be due to the overlap of a positive and a negative peak since the observed splitting is about the same as the full width of the peaks. The calculated splitting between the states is only 10 cm^{-1} if using the dipole-dipole interactions as the only source for this splitting. Kinetic energy coupling contributes to the increase

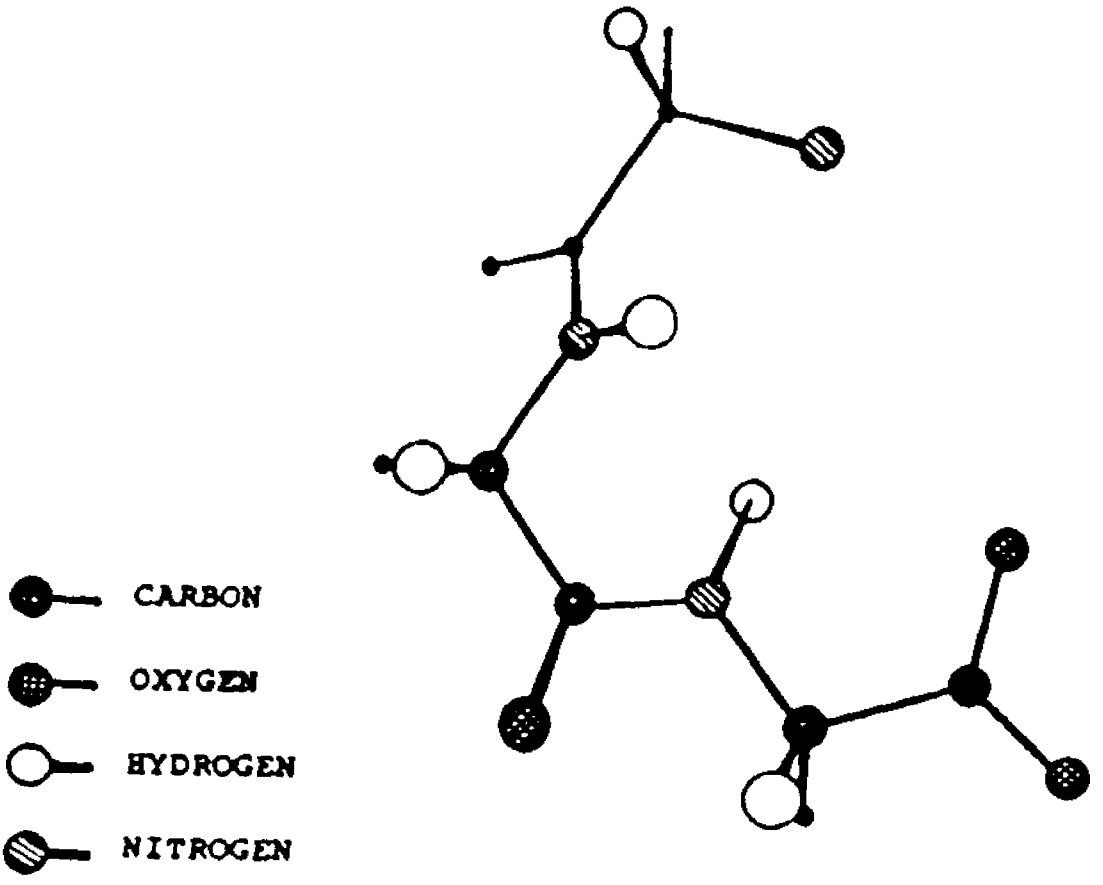

Figure 47. Proposed Solution Conformation of L-L-L, based on experimental VCD and IR absorption data, and energy minimization calculations. ϕ = 120°, Ψ = -25°.

of the splitting. That the original amide I' transitions may not be exactly degenerate could also contribute to the splitting.

It is also beneficial, via conformational energy calculations, to assess whether or not a molecule (such as L-alanyl-L-alanyl-L-alanine) is likely to exist as a structure similar to the one shown in Figure 47. This conformation is stabilized by a intramolecular zwitterionic attraction. Although these computations (*vide supra*) do not take into account solvation, which may be a major factor in the stabilization of zwitterionic species, the resulting structure is twisted strongly so the ionic end groups can come near each other. The amount of stabilization energy, compared to a fully extended form, is on the order of 300 kJ/mol. Thus, these calculations support that L-alanyl-L-alanyl-L-alanine exists in aqueous solution in a structure, or a number of structures, similar to the one shown in Figure 47.

However, the possibility certainly exists that intermolecular head-to-tail zwitterionic interactions of two or more L-alanyl-L-alanyl-L-alanine molecules are the cause of the stabilization. This possibility can not be eliminated entirely since the concentration range studied was still high. Such structures would be less strained, however. It is still assumed

that the geometry of the central portion of the peptide backbone (I) would be similar to that of the internally stabilized structures in order to produce the same spectral features.

The IR feature remains unchanged as the concentration decreases. However, some instrumental constraints have prevented observing VCD as a function of concentration below 0.005M. The main obstacle is the strong water absorption, which limited the cell path length to be not longer than 100 μm. That the IR spectra do not change appreciably with concentration suggests intramolecular coupling.

Upon removing the zwitterionic character of the end groups by a base titration, the VCD couplet and the distinct peaks in the IR absorption spectra disappear (*cf.* Figure 48). Instead, the absorption spectrum shows only two peaks: the antisymmetric carboxylic stretching vibration at 1595 cm^{-1} and the amide I′ at 1643 cm^{-1}. This latter peak is nearly as intense as the carboxylic stretching signal with about the same $\Delta\epsilon(\bar{\nu})/\epsilon(\bar{\nu})$ as in the neutral L-alanyl-L-alanyl-L-alanine. At 1643 cm^{-1}, there is still little negative VCD intensity, most likely not due to the carboxylic vibration. Similarly, N-acetyl-L-alanyl-N′-methyl-amide, which possesses the same peptide

linkage (I) environment as L-alanyl-L-alanyl-L-alanine, exhibits only a single VCD peak in the 1550-1750 cm^{-1} region with a $\Delta\epsilon(\bar{\nu})/\epsilon(\bar{\nu})$ of -1.7×10^{-5} (*cf.* Figure 49).

Concluding from the absence of the coupled oscillator spectral features in the latter two samples, the zwitterions are necessary for the stabilization of L-alanyl-L-alanyl-L-alanine in the neutral solution. Without such a stabilization, no dominant structure supporting the coupling of oscillators exists. It will be interesting to extend these studies to some different, somewhat larger peptides, for which intramolecular zwitterionic interactions have been postulated[81]. VCD, with is high sensitivity toward detecting secondary structure, thus may become a prime technique in the structural investigations of small biomolecules in aqueous solution.

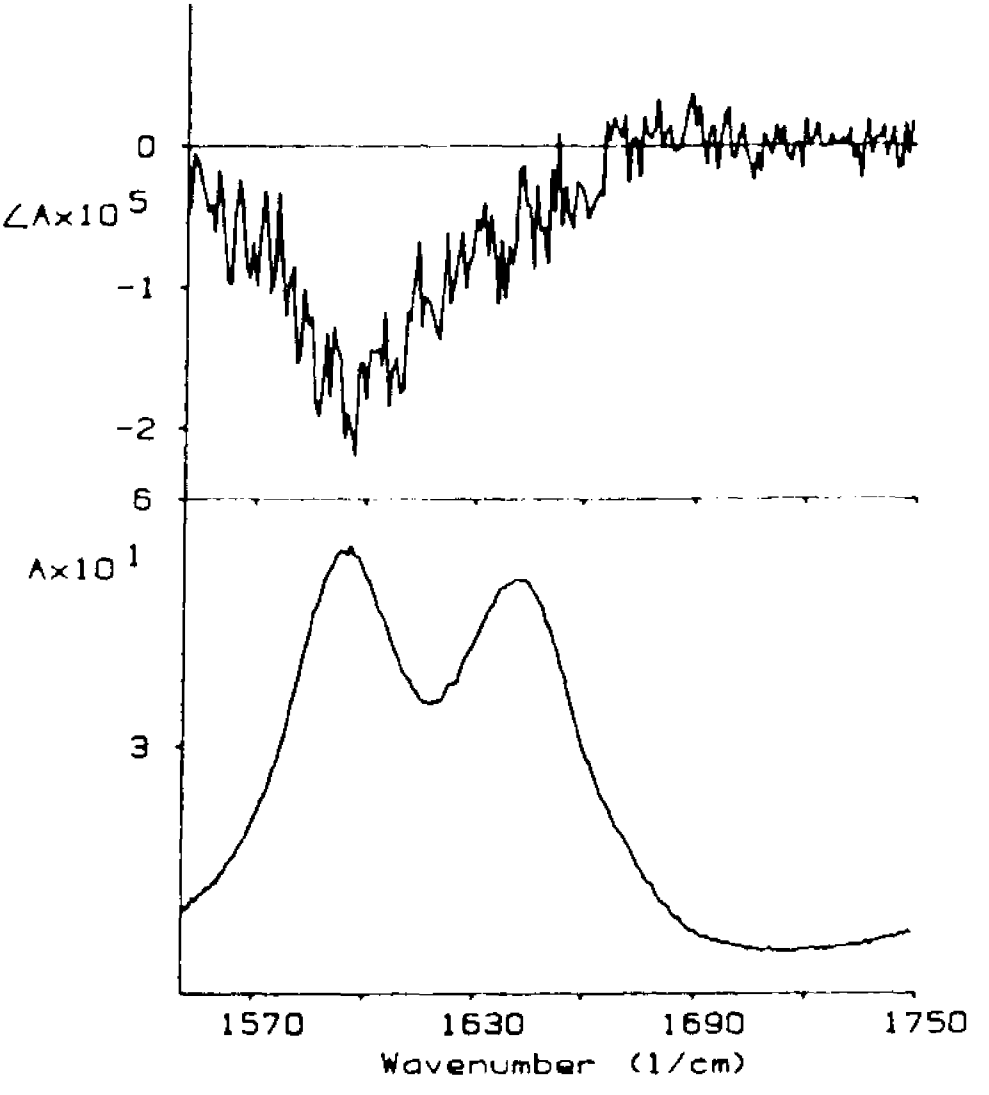

Figure 48. Spectra of L-L-L in basic solution.
C = 0.5 M, pD ≈ 13; top: VCD; bottom: IR.

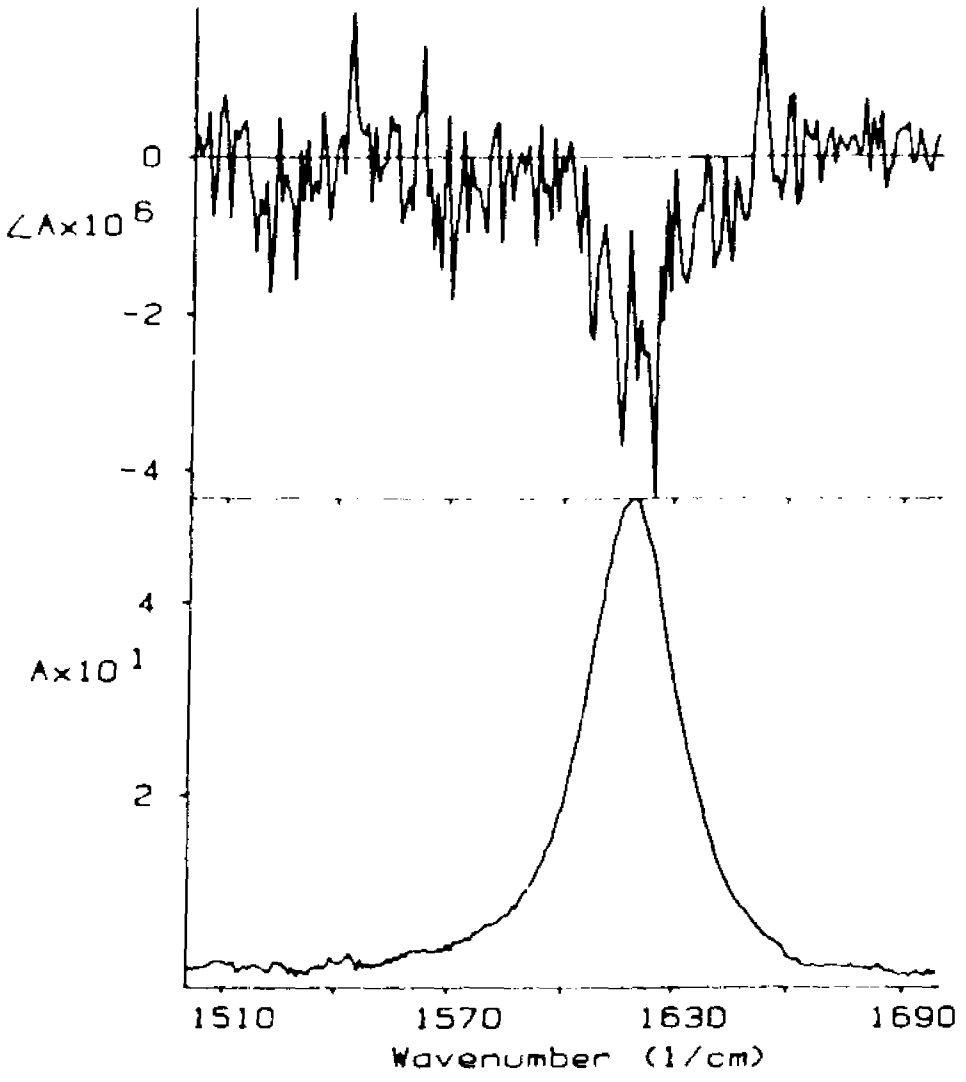

Figure 49. Spectra of AAMA in D_2O, C = 0.4 M; top: VCD; bottom: IR.

References

[1] Michl, J. & Thulstrup, E.W., in *"Spectroscopy with Polarized Light, Solute Alignment by Photoselection, in Liquid Crystals, Polymers, and Membranes"*; VCH Publishers, Inc., New York, **1986**; Chapter one.

[2] Jenkins, F.A. & White, H.E., *"Fundamentals of Optics"*, Fourth Edition, McGraw-Hill, Inc., **1976.**

[3] Atkins, P.W., *"Physical Chemistry"*, Fourth Ed., W.H. Freeman and Company, New York, **1990.**

[4] Nafie, L.A. and Diem, M., *Acc.Chem.Res.*, **1979**, 12, 296.

[5] Diem, M.,in *"Vibrational Spectra and Structure"*, Durig, J., Editor, Elsevier Science Publishers, Amsterdam, The Netherlands, **1991**, Vol. 19, 1.

[6] Keiderling, T.A.,in *'Practical Fourier Transform Infrared Spectroscopy'*, **1990**, Academic Press, NY, pp 203-283.

[7] Freedman,T.B. and Nafie,L.A., in *"Topics in Stereochemistry"*, Eliel, E.L., and Wilen, S.H., Editors, J. Wiley and Sons, New York, **1987**,

Vol.17, 114.

[8] Chabay, I.; Hsu, E.C. & Holtzwarth, G., *Chem. Phys. Lett.* **1972**, 15(2), 211.

[9] Holtzwarth,G., Hsu,E.C., Mosher,H.S., Faulkner, T.R., and Moscowitz, A., *J.Amer.Chem.Soc.*, **1974**, 96, 251.

Faulkner, T.R., Moscowitz, A., Holtzwarth, G., Hsu, E.C. and Mosher,H., *J.Amer.Chem.Soc.*, **1974**, 96, 252.

[10] a) Osborne, G.A., Cheng, J.C. & Stephens, *Rev. Sci. Instr.*, **1973**, 44, 10.

b) Nafie, L.A., Keiderling, T.A., Stephens, P.J., *J. Amer. Chem. Soc.*, **1976**, 98(10), 2715.

c) Keiderling,T.A. and Stephens,P.J., *J.Chem. Phys.*, **1976**, 41, 46.

[11] Su, C.N., Heintz, V.J. and Keiderling, T.A., *Chem. Phys. Letters*, **1980**, 73, 157.

Su,C.N. and Keiderling, T.A., *J.Amer.Chem.Soc.*, **1980**, 102, 511.

[12] Diem, M., Gotkin, P.J., Kupfer, J.M., Tindall, A.P. and Nafie, L.A., *J. Am. Chem. Soc.*, **1977**, 99, 8103.

[13] Stephens, P.J. & Lowe, M.A., *Ann. Rev. Phys. Chem.*, **1985**, 36, 213.

[14] Cahan, N.V. & Hameka, H.F., *J. Am. Chem. Soc.*,

1966, 88, 2136.

[15] Schellman, J.A., *J.Chem.Phys.*, **1973**, 58, 2882.

[16] Deutsche, C.W., & Moscowitz, J., *J.Chem. Phys.*, **1968**, 49, 3257.

Deutsche, C.W., & Moscowitz, J., *J.Chem. Phys.*, **1970**, 53, 2630.

[17] Polavarapu, P.L., *Mol. Phys.*, **1983**, 49, 645.

[18] Stephens, P.J., *J.Am.Chem.Soc.*, **1985**, 107, 748.

[19] Holtzwarth, G. and Chabay, I., *J. Chem. Phys.*, **1972**, 57(4), 1632.

Holtzwarth, G., Chabay, I. & Holtzwarth, N.A.W., *J. Chem. Phys.*, **1973**, 58, 4816.

[20] Freeman, T.B., Balukjian, G.A. & Nafie, L.A., *J. Am.Chem. Soc.*, **1985**, 107, 6213.

[21] Lee, O., Roberts, G.M. & Diem, M., *Biopolymers*, **1989**, 28, 1759.

[22] Roberts, G.M., Lee, O., Calienni, J., and Diem, M., *J.Am.Chem. Soc.*, **1988**, 110, 1749.

[23] Gulotta, M. Goss, D.J. & Diem, M., *Biopolymers*, **1989**, 28, 2047.

[24] Zhong, W., Gulotta, M., Goss, D.J. & Diem, M., *Biochemistry*, **1990**, 29, 7485.

[25] Diem, M., Lee, O. and Roberts, G.M., accepted by *J. Phys. Chem.*, **Feb., 1992**.

[26] Tinoco, I., *Radiation Research* **1963**, 20, 133.

[27] Bayley, P.M. Nielsen, E.B. & Schellman, J.A.,

J.Phys.Chem., **1969**, 73, 28.

[28] Keiderling, T.A. & Stephens, P.J., *J. Am. Chem. Soc.*, **1978**, 99, 8061.

[29] Narayanan, U., & Keiderling, T.A., *J. Am. Chem. Soc.*, **1983**, 105, 6406.

[30] Snir, J., Frankel, R.A. & Schellman, J.A., *Biopolymers*, **1975**, 14, 173.

[31] Chabay, I., and Holtzwarth, G., *Applied Optics*, **1975**, 14(2), 454.

[32] Diem, M., Roberts, G.M., Lee, O., and Barlow, A., *Applied Spectroscopy*, **1988**, 42(1), 20.

[33] Grosjean, M. and Legrand, M., *C.R. Acad. Sci.* (Paris), **1960**, 251, 2150.

[34] Velluz, L., Grosjean, M., and Legrand, M., *"Optical Circular Dichroism"*, Academic Press, New York, **1965**.

[35] Modine, F.A., Major, R.W., and Sonder, E., *Applied Optics*, **1975**, 14(3),757.

[36] Hoffman, G.G., Schrader, B., and Snatzke, G., *Rev. Scient. Instrum.*, **1987**, 58, 1675.

[37] Kemp, J.C., *J. Optical Soc. Amer.*, **1969**, 59, 950.

[38] Cheng, J.C., Nafie, L.A., Allen, S.D., and Braunstein, A.L., *Applied Optics*, **1976**, 15(8), 1960.

[39] Cheng, J.C., Nafie, L.A., and Stephens, P.J., *J. Optical Soc. America*, **1975**, 65(9), 1031.

[40] Arfken, G., *"Mathematical Methods for Physicists"*, Second edition, Academic Press, New York, **1970**, chap.11, (11.1).

[41] Griffiths, P.R. and de Haseth, J.A., *"Fourier Transform Infrared Spectroscopy"*, Vol.83 in *Chemical Analysis Series*, Editors Elving, P.J. & Winefordner, J.D., John Wiley & Sons, New York, **1986**.

[42] Perkins, W.D., *J. Chem. Education*, **1986**, 63(1), A5.

Perkins, W.D., *J. Chem. Education*, **1987**, 64(11), A269.

Perkins, W.D., *J. Chem. Education*, **1987**, 64(12), A296.

[43] Nafie, L.A. and Diem, M., *Appl. Spectrosc.*, **1979**, 33(2), 130.

[44] Nafie, L.A., Diem, M., and Vidrine, *J. Amer. Chem. Soc.*, **1979**, 101, 496.

[45] Polavarapu, P.L., *Appl. Spectros.*, **1984**, 38(1), 26.

Polavarapu, P.L., Michalska, D.F., and Back, D.M., *Appl. Spectros.*,**1984**, 38(3), 438.

[46] Keiderling, T.A., & Malon, P., *Appl. Spectros.*, **1988**, 42(1), 32.

[47] Lipp, E.D., Zimba, C.G., and Nafie, L.A., *Chem. Phys. Lett.*, **1982**, 90, 1.

[48] Lipp, E.D. and Nafie, L.A., *Appl. Spectrosco.*, **1984**, 38(1), 20.

[49] McCoy, C.A. and de Haseth, J.A., *Applied Spectroscopy*. **1988**, 42(2), 336.

[50] Yoo, R.K., Croatto, P.V., Wang, B.L., and Keiderling, T.A., *Applied Spectroscopy*, **1991**, 45(2), 231.

[51] Martin, D.H. and Puplett, E., *Infrared Physics*, **1969**, 10, 105, Pergamon Press.

[52] Burton, C.H. and Akimoto, Y., *Infrared Physics*, **1980**, 20, 115.

[53] Dignam, M.J. and Baker, M.D., *Appl. Spectrosco.*, **1981**, 35(2), 186.

[54] Polavarapu, P.L., *Infrared Physics*, **1988**, 28(2), 109.

[55] Polavarapu, P.L. and Weibel, S., *Applied Spectroscopy*, **1990**, 44(8), 1369.

[56] Ragunathan, N., Lee, N.S., Freedman, T.B., Nafie, L.A., Tripp, C., and Buijs, H., *Applied Spectrosc.*, **1990**, 44(1), 5.

[57] Keiderling, T.A., *Applied Spectroscopy Review*, **1981**, 17, 189.

[58] Diem, M., Oboodi, M.R. and Alva, C.,

Biopolymers, **1984**, **23**, 1917.

[59] Janos Technology, Inc., *"Precision Optics and Components" (optics catalog)*, **1984**.

[60] Diem, M., Adar, F., and Grayzel, R., *Computer Enhanced Spectrosc.*, **1986**, **3**, 29.

[61] Lee, O. and Diem, M., summited to *Analytical Instrumentation*, **1991**.

[62] Oboodi, M.R., Alva, C., and Diem, M., *J. Phys. Chem.*, **1984**, **88**, 501.

[63] Singh, R.D.; Keiderling, T.A., *Biopolymers*, **1981**,**20**, 237.

[64] Lal, B.B., Nafie, L.A., *Biopolymers*, **1982**,**21**, 2161.

[65] Sen, A.C.; Keiderling, T.A., *Biopolymers*, **1981**,**23**, 1519

[66] Sen, A.C.; Keiderling, T.A., *Biopolymers*, **1981**,**20**, 1537

[67] Narayanan, U.; Keiderling, T.A.; Bonora, G.M.; Toniolo, C., *Biopolymers*, **1985**,**24**, 1757.

[68] Narayanan, U.; Keiderling, T.A.; Bonora, G.M.; Toniolo, C., *J. Am. Chem. Soc.*, **1986**,**108**, 2431.

[69] Yasui, S.C.; Keiderling, T.A., *J. Am. Chem. Soc.*, **1986**,**108**, 5576.

[70] Paterlini, G.M.; Freedman, T.B.; Nafie, L.A., *Biopolymers*, **1986**, **25**, 1751.

[71] Lord, R.C., *Applied Spectrosc.*, **1977**, **31**, 187.

[72] Miyazawa, T.; Shimanouchi, T.; Mizushima, S.I., *J.Chem. Phys.*, **1958**, 29, 611.

[73] Krimm, S. and Bandekar, J., *Biopolymers*, **1980**, 19, 1.

[74] Gull-maj Roberts, Ph.D. dissertation, **1991**, City University of New York.

[75] Diem, M.; Polavarapu, P.L.; M.R., Nafie, L.A., *J. Am. Chem, Soc.*, **1982**, 104, 3329.

[76] Diem. M., *J. Am. Chem.Soc.*, **1988**, 110, 6967.

[77] Barron, L.D., in "*Advances in Infrared Raman Spectroscopy*", Vol. 4, Clark, R.J.H & Hester, R.E., Eds., Heyden, London, pp.271.

[78] Diem, M., *Comp. Enhanced Spectrosc.*, **1983**, 1, 19.

[79] Faulkner, T.R., Ph.D. thesis, University of Minnesota, **1976**.

[80] Nemethy, G. & Scheraga, H.A, *Quarterly Review Biophys.*, **1977**, 10, 239.

[81] Khaled, M.A., Long, M.M., Thompson, W.D., Bradley, R.J., Brown, G.B. & Urry, D.W., *Biochem. Biophys. Res. Commun.*, **1977**, 76, 619.